

Abstract

Interactions and Regulation of the Microtubule System by Viral and Cellular Proteins

Pei-Tzu Huang

2020

Microtubules are important for diverse cellular functions, including motility, mitosis, and vesicle transport. Kinesins are motor proteins that hydrolyze ATP to provide the energy for its translocation and carry cargo along microtubules. My dissertation focuses on the microtubule system, specifically on the interactions between the kinesin adaptor protein FEZ1 and HIV-1 virus capsid and the regulation of microtubule dynamics by kinesin Kip2.

Human immunodeficiency virus type 1 (HIV-1) is a challenging world health problem. The HIV-1 virion is composed of an outer membrane surrounding the HIV-1 capsid and other accessory proteins. The HIV-1 capsid is a protein cone that encapsulates and protects the viral genome during early stages of virus infection. It provides an important platform for the interaction of various host factors to ensure successful virus infection. After entry into the cell, HIV-1 virus is transported along microtubules towards the cell nucleus, but little is known about the exact mechanism of this process. It was discovered that a kinesin adaptor protein, FEZ1, is involved in the HIV-1 movement toward the nucleus. In a pulldown assay using mammalian cell lysate, FEZ1 interacts with *in vitro* assembled HIV-1 capsid tubes, hinting at a potential direct interaction between FEZ1 and capsid.

For the first part of my dissertation, I set out to investigate the interaction of FEZ1-capsid and the role of FEZ1 in HIV-1 infection utilizing biochemical and biophysical assays. I first confirmed the direct interaction of FEZ1 with capsid, and found that FEZ1 uses highly negative charged regions to interact with capsid. Interestingly, since FEZ1 has multiple regions of negative charges, it has the advantage of avidity binding that strengthens its interaction with capsid under physiological conditions. Next, I mapped the FEZ1 binding site on capsid with different capsid assemblies, and found that FEZ1 particularly recognizes the capsid hexamer. Upon examining the electrostatic charge map of the HIV-1 capsid hexamer, I discovered the center R18 ring is positively charged, and I confirmed the importance of this charge-charge interaction between FEZ1 and capsid hexamer R18. I also performed competition binding assays with nucleotides and the small molecule IP6, all shown to interact with R18, and found that the binding of FEZ1 was reduced with increasing nucleotide/IP6 concentration. Furthermore, model simulation provided additional evidence of this FEZ1-capsid interaction. Lastly, we obtained virology data that mutation of FEZ1 negative charges reduced the virus trafficking to nucleus and reduced infection. These results established a comprehensive framework for a mechanistic understanding of the important function of FEZ1 in HIV-1 capsid trafficking on the microtubule and infection, and revealed key residues in the interaction. This is the first report that demonstrates the direct interaction of the cytoskeletal system - a kinesin adaptor protein - to capsid at the molecular level, and can serve as a model for other capsid binding factors.

For the second part of my dissertation, I investigated an intriguing yeast kinesin that functions as a polymerase besides transportation of cargoes and regulates the

dynamics of microtubules. Kip2 is a yeast kinesin that is critical in yeast mitosis, and mutation of Kip2 results in nuclear migration defects and abnormal lengths of microtubules. More interestingly, Kip2 promotes microtubule growth on its own. To unveil the mechanism of how Kip2 promotes microtubule polymerization, I started with investigating the different domains of Kip2 and observe their motility and effects on microtubule dynamics. I found that the motor domain alone can nearly account for the reduction in microtubule catastrophe frequency, while the C-terminus alone does not affect the microtubule dynamics. These results advanced our understanding of how Kip2 regulates the microtubule dynamics.

In summary, my thesis research provided insight into the functions and key interaction sites of a kinesin adaptor protein, FEZ1, and its cargo, HIV-1 capsid, and also shed light on the regulation of microtubule by yeast kinesin Kip2.

Interactions and Regulation of the Microtubule System by Viral and Cellular Proteins

A Dissertation
Presented to the Faculty of the Graduate School
of
Yale University
in Candidacy for the Degree of
Doctor of Philosophy

by
Pei-Tzu Huang

Dissertation Director: Yong Xiong, Jonathon Howard

May 2020

© 2020 by Pei-Tzu Huang

All rights reserved

Acknowledgements

There are so many people that I am thankful for throughout this incredible journey, and I would love to thank everyone for their support and encouragement.

First and foremost, I would love to thank my dearest family. Thank you to my parents for the unconditional love, for always supporting my decisions from learning arts and literature to studying sciences. Both of you served as great role models for me (PhD/MS in engineering and literature), and it is from you that I got the courage to pursue my dreams of studying abroad. Thank you, my dear siblings, for the warm phone calls and visits, and being strong mental support for me whenever and wherever. I would have never done this without you.

Thank you, my dear partner Leo, for always being there for me through ups and downs ever since high school. You made my days so much happier and colorful. Life would be totally different without you.

Thank you, my dear mentors, Yong and Joe, for supporting my development as a scientist. Thank you for providing guidance and encouragement, sharing your knowledge and experience about scientific thinking, writing, and presenting. I am grateful for the opportunity to be in such wonderful labs and discover all the different fascinations of research.

I would like to thank all the members of my two labs, Xiong Lab and Howard Lab, for help, suggestions, and warm company. Especially, I would like to thank Kris (and Rafael) and Maijia, for great chats over bubble tea, and all the fun we had together over numerous meals! Thank you for making everyday life in lab joyful. Wanyu and Catherine, you two are wonderful and generous people that I love to dance and hangout with! Oli and Sonal, I love running with you two, and hopefully we can run half-marathon together some day! Also thank you to Alicia, Xiaoyun, Chenxiang, Xiaofei, Wei, and Olga, for guiding me through the early years.

I must thank my committee members, Thomas Pollard and Charles Sindelar, for mentoring and scientific guidance. Thank you for always encourage me to improve on my presentation, think about the bigger picture at a higher level, and go even deeper into science questions. Your feedback and suggestions are greatly appreciated.

Thank you, all my friends and mentors, throughout the years. Vicky, Mandy, Monica, Kevin, Henry, and Hungni, thank you for being so supportive and be there when I needed for all these years. Nichole, I love chatting and going to the gym with you. Big thanks to my advisors and friends from the McDougal Center and OISS, I love working with you all! Thank you, Lisa, Jen, and Molly, for letting my creative ideas flow and do crafty workshops. Organizing fun and meaningful events is one of the best parts of my grad school. Special thanks to my advisor and friends from the Office of New Haven Affairs, Pathways to Science/Art, Maria and Sarah. It is so fun to be part of the greater science outreach community and I really enjoyed helping out in various science outreach programs. It is very inspiring to plant the love for science in young minds! Also thank you to the Yale Good Life Center and Peer Wellness fellows, especially Tracy and Maria. I love the yoga and meditation activities we did. It is great to discover the inner mind wellness and also helping fellow grad students to lead a more balanced grad school life. Thank you, my friends from YYGS and Splash, together I discovered and cultivated my love for mentoring and teaching.

Thank you everyone for making this a transformative experience!

List of Figures

| | |
|--|----|
| Figure 1-1 Proposed model for post-entry events of HIV-1 infection | 5 |
| Figure 1-2 HIV-1 Capsid is Important for Virus Functions | 7 |
| Figure 1-3 FEZ1 is a Kinesin Adaptor Protein that Promotes HIV-1 Infection..... | 10 |
| Figure 2-1 FEZ1 protein domain, purification, and capsid tube binding | 13 |
| Figure 2-2 Mapping the capsid binding region on FEZ1 | 17 |
| Figure 3-1 FEZ1 uses negatively-charged poly-glutamate regions to bind CA hexamers | 22 |
| Figure 4-1 Determining the binding parameters of FEZ1 with HIV-1 capsid using ITC.. | 24 |
| Figure 5-1 FEZ1 recognizes the positively charged center pore of CA hexamers through electrostatic interactions | 29 |
| Figure 5-2 Comparison of structures of the WT and R18D CA Hexamers with the open or the closed conformation of the b-hairpin. | 31 |
| Figure 5-3 FEZ1 pelleting assay with CA tubes at different buffer pH. | 32 |
| Figure 5-4 Mapping additional binding sites on the capsid hexamer | 32 |
| Figure 5-5 Electrostatic interaction is important for FEZ1 binding with CA hexamer | 34 |
| Figure 5-6 FEZ1 has multiple negatively charged regions for avid binding to the capsid | 36 |
| Figure 6-1 FEZ1 Capsid-Binding Regions Contribute to Early HIV-1 Infection | 42 |
| Figure 7-1 All-atom molecular dynamic simulations identify FEZ1 interactions at the CA hexamer center. | 45 |
| Figure 8-1 Cartoon figures of the FEZ1 fusion proteins | 47 |
| Figure 8-2 Co-crystallization of FEZ1 constructs and peptide with HIV-1 capsid..... | 50 |
| Figure 8-3 Using GST-FEZ1 to obtain FEZ1-capsid complex structure | 52 |
| Figure 8-4 CypA-FEZ1 fusion protein as a helical symmetry approach to capture the FEZ1-capsid complex..... | 54 |
| Figure 8-5 Utilizing the SpyTag/SpyCatcher system for the study of FEZ1-capsid complex | 56 |
| Figure 8-6 Using llama-FEZ1 to probe the structure of FEZ1-capsid complex | 58 |
| Figure 9-1 Schematic Models of HIV-1 Capsid Trafficking on Microtubules and a Conserved Targeting Site at the CA Hexamer Center | 63 |
| Figure 9-1 Microtubules are dynamic structures | 70 |
| Figure 9-2 Kinesin and dynein motors in the budding yeast. | 75 |
| Figure 10-1 Purification of Kip2FL..... | 80 |
| Figure 10-2 Schematic of dynamic microtubule assay | 81 |
| Figure 10-3 Full-length Kip2 increases the growth rate and reduces the catastrophe frequency of dynamic microtubules | 83 |
| Figure 10-4 Structure Predictions of Kip2C and its role in microtubule polymerization.. | 85 |
| Figure 10-5 Kip2C does not affect microtubule dynamics, even at very high concentrations | 87 |
| Figure 10-6 Kip2MC1 affects microtubule dynamics by reducing catastrophe frequency | 91 |

| | |
|---|-----|
| Figure 10-7 Depolymerization of GMPCPP-stabilized microtubules by Kip2FL and Kip2MC1 | 92 |
| Figure 11-1 Schematic of the single-molecule motility assay..... | 93 |
| Figure 11-2 Full-length Kip2 is a highly processive motor that dwells at microtubule plus-ends..... | 94 |
| Figure 11-3 Kip2MC1 is also a processive motor that dwells at microtubule plus-end .. | 95 |
| Figure 12-1 Negative stain EM images of Kip2 proteins with microtubules | 97 |
| | |
| Appendix 1-1 Domain organization and sequence similarities of the stathmin family protein. | 111 |
| Appendix 2-1 SRB3-D1 & RB3-D1 fusion proteins form stable complexes with tubulins | 118 |
| Appendix 2-2 RB3-D1-D1, SRB3-D1-D1, and Nter-RB3-D1-D1 form stable complexes with tubulins..... | 121 |
| Appendix 2-3 Adding in linkers to help relax the curvature of RB3 | 121 |
| Appendix 2-4 Addition of GMPCPP did not improve the tubulin assembly | 123 |
| Appendix 2-5 Crosslinking of the tubulin assemblies | 124 |
| Appendix 2-6 EB1 in the binding of tubulins and RB3/D1 constructs..... | 128 |
| Appendix 2-7 Structural investigation of tau interaction with tubulins | 130 |
| Appendix 3-1 Tau binding to microtubules | 134 |

List of Tables

| | |
|---|-----|
| Table 1 Data collection and refinement statistics for the R18D CA crystal structure. | 28 |
| Table 2 Crystallographic conditions of FEZ1 proteins, FEZ1 peptide, and FEZ1 fusion proteins..... | 49 |
| Table 3 Data collection of FEZ1 peptide with hexamers or half-hexamers | 50 |
| Table 4 Summary of FEZ1 constructs..... | 64 |
| Table 5 List of tubulin-MAP structures | 108 |

Table of Contents

| | |
|--|-----------|
| Dissertation Aims and Scope..... | 1 |
| FEZ1 is recruited to a conserved cofactor site on capsid to promote HIV-1 trafficking | 4 |
| 1 Introduction..... | 4 |
| 1.1 HIV-1 and the Viral Life Cycle | 4 |
| 1.2 HIV-1 Capsid is Important for Virus Functions | 5 |
| 1.3 Transportation of HIV-1 Capsid Along the Microtubule Network..... | 7 |
| 1.4 FEZ1 is a Kinesin Adaptor Protein that Promotes HIV-1 Infection..... | 9 |
| 1.5 Aims and Scope | 10 |
| 2 FEZ1 directly interacts with the HIV-1 capsid through negatively charged residues..... | 12 |
| 2.1 Introduction | 12 |
| 2.2 Results | 14 |
| 2.2.1 FEZ1 directly interacts with the HIV-1 CA capsid | 14 |
| 2.2.2 FEZ1 uses highly negatively charged residues to interact with the HIV-1 capsid protein ... | 15 |
| 2.3 Discussion..... | 17 |
| 3 Determination of the HIV-1 capsid binding of FEZ1: FEZ1 interacts with the capsid hexamer | 18 |
| 3.1 Introduction | 18 |
| 3.2 Results | 19 |
| 3.2.1 FEZ1 specifically recognizes the HIV-1 capsid hexamer..... | 19 |
| 3.2.2 FEZ1 does not bind to HIV-1 capsid pentamer..... | 20 |
| 3.3 Discussion..... | 21 |
| 4 Determining the binding parameters of FEZ1 with HIV-1 capsid using ITC | 23 |
| 4.1 Introduction | 23 |
| 4.2 Results | 23 |
| 4.3 Discussion..... | 24 |
| 5 FEZ1 binds to capsid through charge-charge interaction using a highly conserved viral cofactor binding site | 26 |
| 5.1 Introduction | 26 |
| 5.2 Results | 26 |
| 5.2.1 Charge-charge interactions are important for FEZ1-capsid interaction: R18..... | 26 |
| 5.2.2 Mapping additional binding sites on the capsid hexamer: G89, P90, P207, G208, T210.... | 32 |
| 5.2.3 FEZ1 interacts with a conserved viral co-factor capsid binding site: NTP/dNTP & IP6, SUN2 | 33 |
| 5.2.4 Secondary binding sites provide avidity and enhance FEZ1-capsid interaction | 34 |
| 5.3 Discussion..... | 37 |
| 6 Mutations in FEZ1 negatively charged regions reduce HIV-1 early trafficking and infectivity . | 38 |
| 6.1 Introduction | 38 |
| 6.2 Results and Discussion..... | 39 |
| 7 Model simulation further confirms the charge-charge interaction of FEZ1 with capsid residue R18 | 42 |
| 7.1 Introduction | 42 |
| 7.2 Results and Discussion..... | 43 |
| 8 Structural determination of FEZ1-capsid hexamer complex..... | 46 |
| 8.1 Introduction | 46 |
| 8.2 Results | 47 |

| | |
|--|-----------|
| 8.2.1 Co-crystallization of FEZ1 constructs and peptide with HIV-1 capsid..... | 47 |
| 8.2.2 Using GST-FEZ1 to obtain FEZ1-capsid complex structure by electron microscopy..... | 51 |
| 8.2.3 CypA-FEZ1 fusion protein as a helical symmetry approach to capture the FEZ1-capsid complex..... | 52 |
| 8.2.4 Utilizing the SpyTag/SpyCatcher system for the study of FEZ1-capsid complex..... | 54 |
| 8.2.5 Using llama-FEZ1 to probe the structure of FEZ1-capsid complex..... | 56 |
| 8.3 Discussion..... | 58 |
| 9 Conclusions and Future Directions..... | 60 |
| 10 Material and Methods..... | 63 |
| 10.1 Bacterial Strains..... | 63 |
| 10.2 Human Cell Lines..... | 63 |
| 10.3 Protein expression and purification..... | 63 |
| 10.4 Analytical size-exclusion chromatography (SEC)..... | 64 |
| 10.5 CA Tube Pelleting Assay with purified FEZ1 proteins..... | 65 |
| 10.6 Isothermal Titration Calorimetry..... | 65 |
| 10.7 Crystallization and data collection..... | 65 |
| 10.8 Structure determination and refinement..... | 65 |
| 10.9 Negative stain electron microscopy..... | 65 |
| 10.10 Atomic model building for molecular dynamic (MD) simulations..... | 66 |
| 10.11 System preparation for MD simulation..... | 66 |
| 10.12 MD simulation production runs on Anton2..... | 66 |
| 10.13 Viruses..... | 67 |
| 10.14 Generation of stable pools..... | 67 |
| 10.15 RNAi and measurement of early HIV-1 infection..... | 67 |
| 10.16 Live imaging and analysis..... | 67 |
| 10.17 Data Deposition..... | 68 |
| 11 Publications and News Articles..... | 68 |
| Elucidating the mechanism of how yeast kinesin Kip2 promotes microtubule polymerization..... | 69 |
| 1 Introduction..... | 69 |
| 1.1 Tubulins and Microtubule..... | 69 |
| 1.1.1 Microtubule introduction..... | 69 |
| 1.1.2 MAPs regulate MT functions and dynamics..... | 70 |
| 1.2 Kinesins..... | 72 |
| 1.2.1 Microtubule-based motor proteins..... | 72 |
| 1.2.2 Kinesin superfamily..... | 73 |
| 1.2.3 Kinesins regulate microtubule dynamics..... | 74 |
| 1.2.4 Kinesins throughout the budding yeast cycle..... | 74 |
| 1.3 Kip2..... | 75 |
| 1.3.1 Identification of <i>Saccharomyces cerevisiae</i> kinesin Kip2..... | 75 |
| 1.3.2 Kip2 regulates microtubule dynamics indirectly in budding yeast cell mitosis by transportation of other MAPs to microtubule plus-ends..... | 76 |
| 1.3.3 Kip2 directly regulates microtubule dynamics by acting as a polymerase and anti-catastrophe factor..... | 77 |
| 1.4 Aims and Scope..... | 78 |
| 2 Biophysical and Biochemical Properties of Kip2..... | 79 |
| 2.1 Expression and purification of Kip2..... | 79 |
| 2.2 <i>In vitro</i> reconstitution of microtubule dynamics..... | 80 |
| 2.3 Full-length Kip2 promotes microtubule growth by acting as a microtubule polymerase and anti-catastrophe factor..... | 81 |

| | |
|--|------------|
| 2.4 Kip2 C-terminus may contain potential tubulin/microtubule interaction site | 84 |
| 2.5 Kip2 C-terminus does not have effect on microtubule dynamics | 85 |
| 2.6 High concentration of Kip2 C-terminus still does not have effect on microtubule dynamics | 88 |
| 2.6 Kip2-MC1 affects microtubule dynamics by reducing catastrophe frequency | 89 |
| 2.7 Kip2MC1 lowers the GTP tubulin off-rate constant | 91 |
| 3 Single molecule motility assays | 92 |
| 3.1 A single-molecule motility assay to study biophysical properties of Kip2 | 92 |
| 3.2 Full-length Kip2 is a highly processive motor that dwells at microtubule plus-ends | 93 |
| 3.3 Kip2MC1 has comparable velocity to full-length Kip2 | 94 |
| 4 Visualization of the Kip2-microtubule complex using electron microscopy | 95 |
| 5 Discussion and Future Direction | 97 |
| 5.1 Confirming that Kip2 promotes microtubule growth <i>in vitro</i> at physiologically relevant protein concentrations without accessory proteins | 97 |
| 5.2 Kip2 C-terminus alone does not have effect on microtubule dynamics | 98 |
| 5.3 Kip2MC1 is the minimal motility construct that has comparable velocity to Kip2FL | 100 |
| 5.4 Kip2MC1 affects microtubule dynamics by reducing the catastrophe frequency | 100 |
| 5.5 Possible mechanisms of how Kip2 affects microtubule dynamics | 102 |
| 5.6 Towards a detailed molecular understanding of the mechanism of Kip2 microtubule growth promotion | 103 |
| 6 Material and Methods | 104 |
| 6.1 Protein expression and purification | 104 |
| 6.2 Tubulin and Microtubule preparation protocols | 104 |
| 6.2.1 Purification of bovine brain tubulin | 104 |
| 6.2.2 Cycling of tubulin | 104 |
| 6.2.3 Labeling of tubulin | 104 |
| 6.2.4 Polymerization of GMPCPP-stabilized microtubules | 104 |
| 6.3 Microscopy assay protocols | 104 |
| 6.3.1 Glass silanization | 104 |
| 6.3.2 Flow cell preparation | 105 |
| 6.3.3 Dynamic microtubule assay with bovine tubulin | 105 |
| 6.3.4 Single-molecule motility assay | 105 |
| 6.3.6 TIRF Microscopy | 105 |
| 6.3.7 DIC Microscopy | 105 |
| 6.3.8 Image and data analysis | 106 |
| 6.3.9 Statistics and graphics | 106 |
| Appendix I: Construction of Novel Tubulin Assemblies for Molecular Studies of Microtubule Associated Proteins | 107 |
| 1 Introduction | 107 |
| 1.1 Microtubule Conformations | 107 |
| 1.2 EM Technology Development of Imaging Microtubules/Tubulins and Challenges | 108 |
| 1.3 Tubulin Sequestering Proteins | 109 |
| 1.3.1 Stathmin RB3 | 110 |
| 1.3.2 DARPin | 111 |
| 1.2 End-binding protein EB1 | 113 |
| 1.3 tau protein | 114 |
| 1.4 Aim and Scope | 115 |
| 1.4.1 Develop novel tubulin assemblies | 115 |
| 1.4.2 Study of tau function and mechanism | 116 |
| 2 Construction of Novel Tubulin Assemblies and the Structural Study of Tau | 118 |

| | |
|--|------------|
| 2.1 RB3-D1 and SRB3-D1 forms stable complexes in gel filtration and negative-stain EM | 118 |
| 2.2 Fusion of Stathmin with DARPin, the construction of RB3-D1-D1, Nter-RB3-D1-D1 and SRB3-D1-D1 | 119 |
| 2.3 Adding flexible linkers into RB3-D1-D1 did not improve the tubulin assembly..... | 121 |
| 2.4 Adding in nucleotides did not affect the octamer assembly | 122 |
| 2.5 Crosslinking of the tubulin octamer | 123 |
| 2.6 Using EB1 to help forming the tubulin assembly..... | 125 |
| 2.7 Structural studies of tau using these tubulin assemblies | 128 |
| 3 Discussion | 131 |
| 4 Material and Methods..... | 134 |
| 4.1 Protein expression and purification | 134 |
| 4.2 Size-exclusion chromatography (SEC) binding assays | 134 |
| 4.3 Crystallization | 134 |
| 4.4 Negative stain EM | 135 |
| References | 136 |

Dissertation Aims and Scope

Cells are the basic structures of all living organisms, and are called “the building blocks of lives”. The cytoskeleton system is a complex and dynamic system that assists cells in maintaining the shape and organization, and also help execute critical functions such as cell motility, cell mitosis, and vesicles/organelles transportation. Cytoskeleton is composed of three kinds of filamentous structures, the microtubules, intermediate filaments, and actin filaments. Microtubules are the largest type of filaments, with a diameter of around 25 nm. Analogous to highway system, microtubules serve as the “roads” for motor proteins (“cars”), such as kinesin or dynein, to carry cargoes from one place to the other. Microtubules are highly regulated by many kinds of proteins, including motor protein kinesins (**Kip2**, second part of my thesis), and are utilized by not only the host system, but also for invading pathogens such as viruses (**HIV-1, and kinesin adaptor protein FEZ1**, first part of my thesis), for transportation.

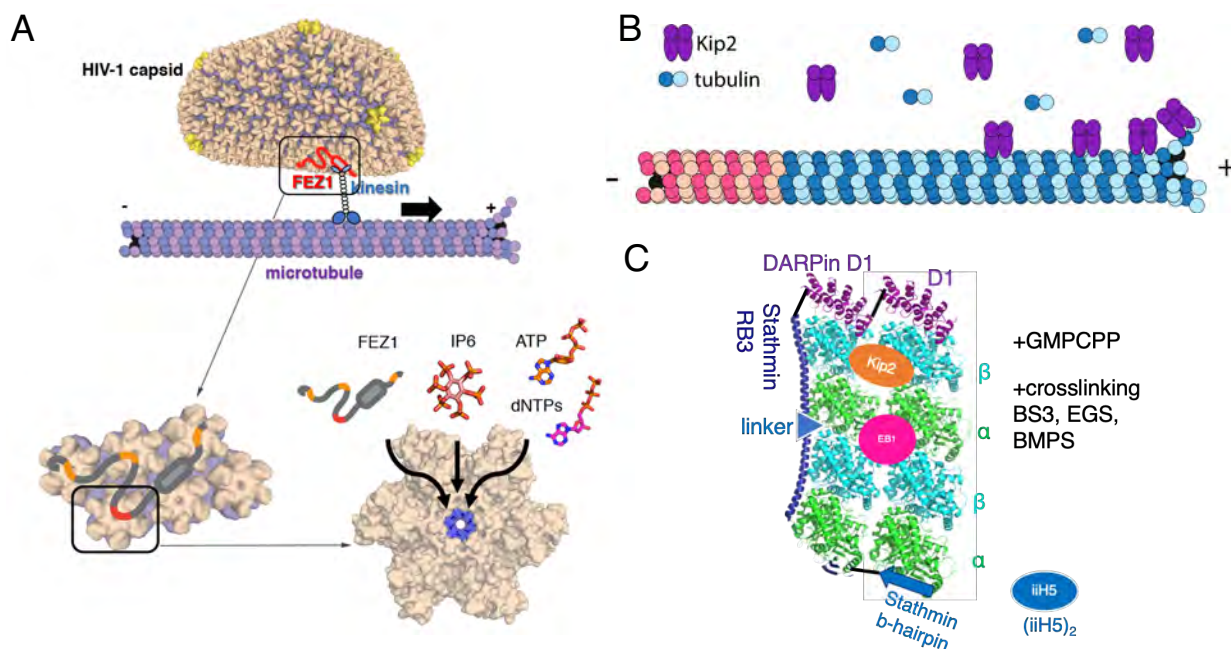
In the first part of my thesis, I investigated the clever strategy that HIV-1 virus uses to infect host cells. HIV-1 hijacks the host microtubule system for its own transport into the nucleus, recruiting both motors, kinesin and dynein, to successfully reach the nucleus. My work focused on kinesin, on examining the role of a kinesin adaptor protein, FEZ1, in the infection of HIV-1. I utilized both biochemistry and biophysical methods, including size exclusion chromatography binding assays and pelleting assays, isothermal titration calorimetry, and model simulation, along with virology and extensive structural approaches to look into the interaction between FEZ1 and HIV-1 capsid, and tease apart

the important residues on FEZ1 in the trafficking and infection of HIV-1 during early post-entry stage (detailed aim in **FEZ1 project section 1.5, p.2**).

In the second part of my thesis, I probed the mechanism of how Kip2 can directly act as a microtubule polymerase and regulate microtubule dynamics. As a kinesin, Kip2 was previously thought to carry other regulatory proteins (dynein, Bik1/CLIP170, Bim1/EB1) to the microtubule plus-end, where these proteins can exert their effect of promoting microtubule growth and function. However, it was discovered that Kip2 alone was able to regulate the microtubule dynamics. In order to unveil the mechanistic details of this regulation, I mapped different parts of Kip2, and looked at the effect on microtubule dynamics. I also observed the motility of these different Kip2 constructs. The final goal is to obtain a structure of the Kip2 with microtubule/tubulin to pinpoint the key interactions, and understand the mechanism in more detail (detailed aim in **Kip2 project section 1.4, p.29**).

To facilitate the study of myriad microtubule associated proteins, MAPs, I was dedicated to construct a novel tubulin assembly that contains multiple microtubule binding sites. I tried extensively different combinations of tubulin sequestering proteins stathmin and DARPin, with the production of fusion proteins or adding in linkers, and also addition of nucleotides and tubulin binding partners. I am testing out crosslinking, and a new tubulin capping protein iiH5. These tubulin assemblies would be powerful tools for the structural study of MAPs in single-particle EM or crystallography.

The outline of my thesis is summarized in **Graphical Summary**.



Graphical Summary of This Thesis

(A) Kinesin adaptor protein FEZ1 directly interacts with HIV-1 capsid in virus trafficking. FEZ1 specifically targets the conserved center pore of capsid protein (CA) hexamers using electrostatic interactions, which is an important site for nucleotides and small molecules. (B) Yeast kinesin Kip2 acts directly as a polymerase and an anti-catastrophe factor, promoting the growth of microtubules. (C) Multiple approaches toward constructing a novel tubulin assembly, including tubulin sequestering proteins stathmin RB3 and DARPin D1, addition of nucleotides, crosslinking, and adding in binding partners.

FEZ1 is recruited to a conserved cofactor site on capsid to promote HIV-1 trafficking

1 Introduction

1.1 HIV-1 and the Viral Life Cycle

Human immunodeficiency virus type-1 (HIV-1) is a retrovirus that causes acquired immune deficiency syndrome (AIDS). HIV-1 is a lentivirus that infects immune system cells such as CD4+ T cells and macrophages, and the gradual loss of infected T cells and the progressive failure of the immune system lead to the development of AIDS and life-threatening opportunistic infections. HIV/AIDS is a serious health challenge that in 2018, approximately 37.9 million people worldwide are infected, and only two people throughout history have ever been cured [1][2][3].

The first step of the viral life cycle is the entry into the host cell. Viruses are able to bind to specific cell surface receptors (CD4) and co-receptors (mainly CXCR4 and CCR5), allowing membrane fusion and viral entry (reviewed in [4]). After HIV-1 viral envelope fusion with the host cell membrane, the capsid is released into the cytosol and is transported towards the nucleus along the microtubule network (**Figure 1-1**) [5]. During this time, the single-stranded viral RNA genome is reverse transcribed into double-stranded DNA and can be integrated into host genome once reaching the nucleus. After integration, HIV-1 can replicate with host genome or stay dormant until reactivated. The final stages of the viral life cycle are virus packaging, budding and maturation (reviewed in [6]).

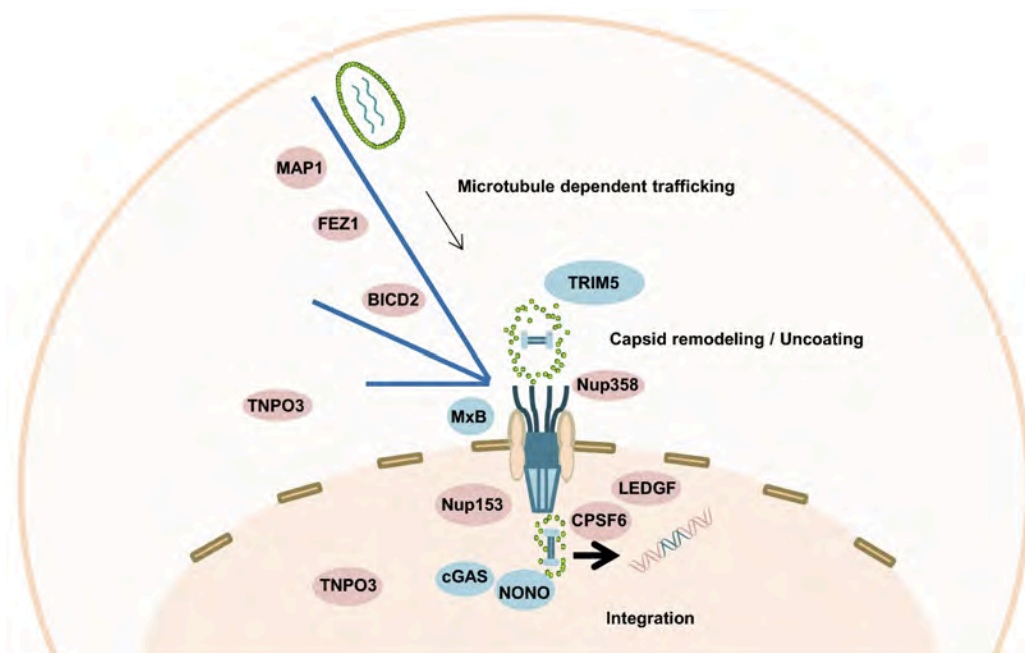


Figure 1-1 Proposed model for post-entry events of HIV-1 infection

Microtubule-associated proteins MAP1, kinesin-1 adaptor protein FEZ1, and dynein adaptor protein BICD2 bind to CA protein and facilitate the net inward trafficking of HIV-1 towards the nuclear membrane. Numerous other factors also participate in the process of HIV-1 transport towards the nucleus. Adapted from [5].

1.2 HIV-1 Capsid is Important for Virus Functions

HIV-1 contains an outer envelope with glycoproteins for host recognition, encapsulating the virus capsid (protein core made from CA proteins) and nucleocapsid (NC), which in turn encloses the viral genome and other accessory proteins required for virus infection (**Figure 1-2A**). The HIV-1 capsid core is a fullerene cone composed of around ~250 CA hexamers and 12 CA pentamers, with 5 pentamers at the narrow end and 7 pentamers at the wide end for closing the curvature of capsid [7-9] (**Figure 1-2B**). It is very heterogeneous in nature (**Figure 1-2C**).

HIV-1 CA is composed of mainly α -helices, with a flexible linker linking its amino-terminal assembly domains (NTD) to the carboxyl-terminal dimerization domain (CTD) [10-12] (**Figure 1-2D**). The assembled CA hexamers or pentamers have an inner ring of

NTDs containing the surface binding sites for host factors, while the CTDs form the inter-subunit contacts linking the hexamers together [8, 13, 14]. At high salt concentrations *in vitro*, the HIV-1 CA hexamers further assemble into hollow cylinders (**Figure 1-2E**) [7, 8, 15, 16], and will be referred to as capsid tubes in this paper.

The viral capsid is central to many of the virus infection processes [17], including prevention of restriction factors from triggering host immune system [6, 18, 19], regulation of reverse transcription [20] and nuclear import pathway [21]. Moreover, there are a diverse array of capsid-binding host factors that can promote (cofactors) or inhibit (restriction factors) the infection of the virus. Cofactors are host proteins utilized by the virus to promote infection, while restriction factors are innate immune molecules that block virus infection (reviewed in [5, 22]). As a result, virus capsid needs to be optimally stable to protect the viral genome from host restriction factors while retaining the ability to disassemble for release of viral genome and integration into host chromosome [23, 24], making capsid a promising therapeutic target for HIV-1 [25-27].

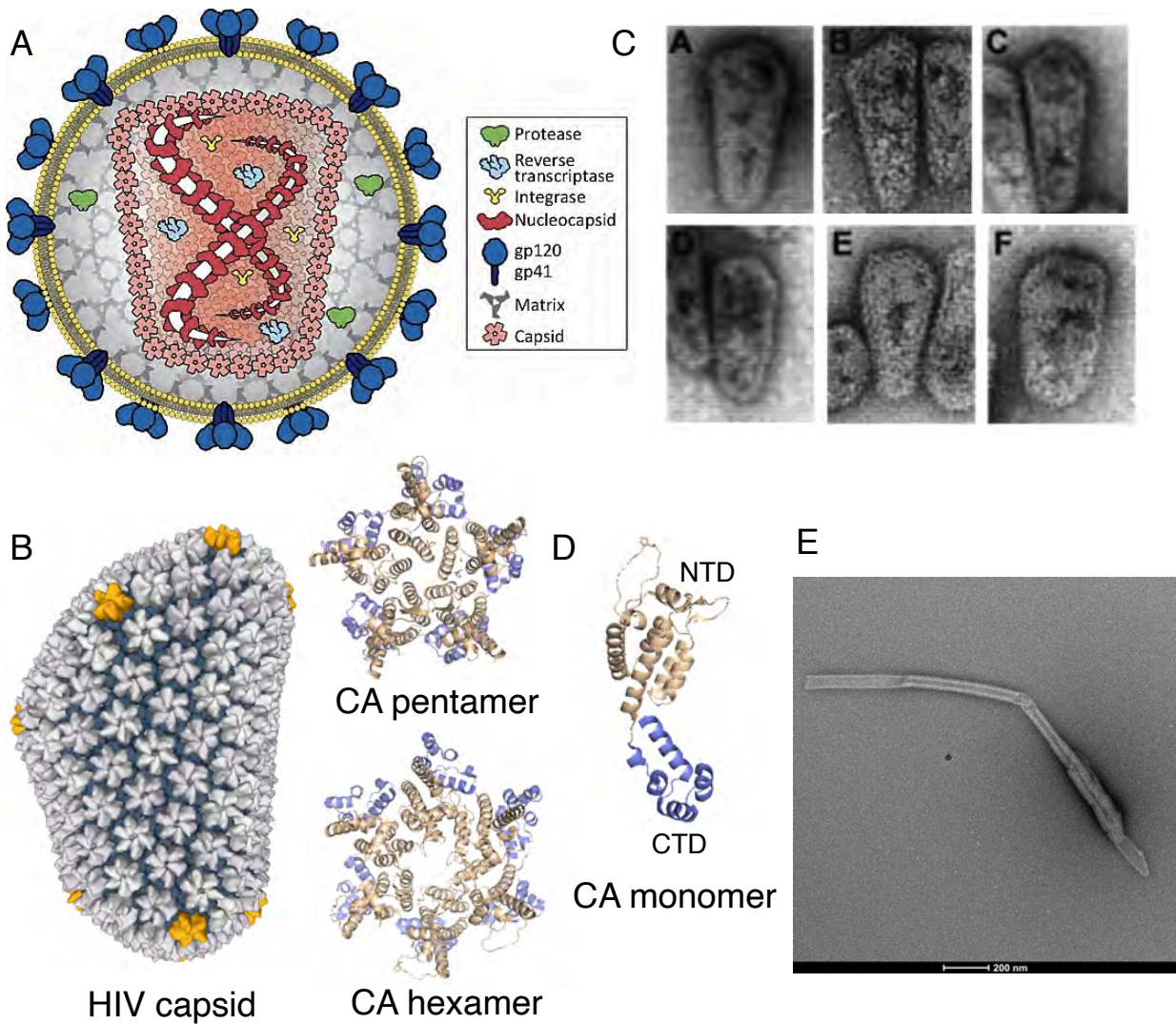


Figure 1-2 HIV-1 Capsid is Important for Virus Functions

(A) A mature HIV-1 virion showing the viral proteins protease, reverse transcriptase, integrase, nucleocapsid, matrix, capsid, gp120, and gp41. Adapted from [28]. (B) An HIV-1 cone is made up of 12 CA pentamers and ~250 CA hexamers. (C) The HIV-1 cone is heterogeneous in shape. Adapted from [29]. (D) The CA monomer that are composed of two globular domains, NTD & CTD, that are linked by flexible linker. (E) EM image Negative-staining specimen of a capsid tube.

1.3 Transport of HIV-1 Capsid Along the Microtubule Network

The dimensions of HIV-1 cones range from 100-200 nm in length and 45-50 nm in width [9, 17, 30]. After fusion with the cellular plasma membranes, viral particles are usually too large to diffuse freely within the crowded cytoplasm environment, since

diffusion of particles larger than 50 nm in diameter is restricted by the structural organization of the cytoplasm [31]. Therefore, they require active transport along microtubules (MT). Intracellular directed long-range transport is mediated by MT and their associated motor proteins, such as dynein or kinesin.

Many viruses including HIV-1, adenoviruses, parvoviruses, other retroviruses, and herpes viruses, exploit the MT and motor proteins for intracellular movements and infections throughout their life cycle (reviewed in [32]). It is shown that HIV-1 stimulates the formation of stable microtubules to promote early infection [33, 34], and these stable MTs can serve as special tracks for cargo protein transportation [35, 36]. Experiments show that GFP-tagged HIV-1 particles transport along the MT with peak velocities of 1 $\mu\text{m/s}$ [37], which is consistent with MT transport rates of cytosolic and virus cargoes [38, 39]. Moreover, disruption of MTs using the MT-depolymerizing drug nocodazole blocks HIV-1 nuclear transport [37] and leads to a two-fold reduction in HIV-1 infection [40]. Additionally, it blocks the nuclear targeting and reduces the viral gene expression of adenovirus type 2 and herpes simplex virus type 1 [41]. Also, microtubule-associated proteins (MAP1A and MAP1S) promote HIV-1 trafficking to the nucleus by stimulating the formation of stable microtubules and mediating the association of HIV-1 CA proteins with microtubules [34].

In terms of interactions with motor proteins, dynein light chain DYNLL1 interacts with HIV-1 integrase and is involved in HIV-1 uncoating and reverse transcription [42-45]. A dynein adaptor protein BicD1 is also shown to interact with and transport human cytomegalovirus tegument protein [46]. Inhibition of dynein by anti-dynein antibody

microinjection or expression of a dominant negative inhibitor of dynactin inhibits incoming viral particles to traffic through the cytoplasm and thus accumulates at the cell periphery [37, 47]. As for kinesins, kinesin 4 family Kif4 have been shown to interact with HIV-1 Gag proteins in late stages of infection, that could either be dependent upon the motor transport activity of Kif4 or the stabilization of MTs [33, 48, 49]. Another kinesin, kinesin 3 Kif3A, also plays an important role in HIV-1 release [50, 51]. These observations suggest that HIV-1 particles can associate with both dynein and kinesin [52], while the detailed mechanism is still unknown.

1.4 FEZ1 is a Kinesin Adaptor Protein that Promotes HIV-1 Infection

FEZ1, fasciculation and elongation protein zeta 1, is a mammalian orthologue of the *C. elegans* locomotor protein UNC-76, which is important in the process of vesicle transportation, nerve bundle formation and axon elongation during neuronal development [53-57]. Locomotive defective worms with mutant UNC-76 have defective axons in neuron bundles unable to reach their full lengths and fail to bundle tightly together [58].

As a kinesin adaptor protein, FEZ1 links the cargo proteins to the cytoskeleton system. FEZ1 is shown to bind and regulate the activity of kinesin-1, functioning in transportation of vesicles and organelles along MTs in the neurons (**Figure 1-3A**). FEZ1 along with the JNK-interacting protein family (JIP) are required for the activation of kinesin-1 Kif5 [59-61]. It is shown that FEZ1 interacts with Kif5 kinesin heavy chain tail using its C-terminal coiled-coil region 231-308 [61] (**Figure 1-3B**). Moreover, FEZ1 is involved in virus infection and transportation to the nucleus depending on kinesin Kif5 [62,

63]. Recently, it was reported that FEZ1 is involved in HIV-1 infection by regulating the viral movement towards the nucleus [63]. Depletion of FEZ1 inhibits HIV-1 virus trafficking to the nucleus, suggesting that FEZ1 is important for HIV-1 infection [63]. FEZ1 promotes viral accumulation near nucleus and its knockdown strongly reduces HIV-1 infectivity (**Figure 1-3C&D**). In their pulldown assay from crude cell lysate, FEZ1 co-pellets with capsid–nucleocapsid complexes (**Figure 1-3E**). However, it is not clear whether FEZ1 and capsid interact directly, and if so, how FEZ1 recognizes the capsid.

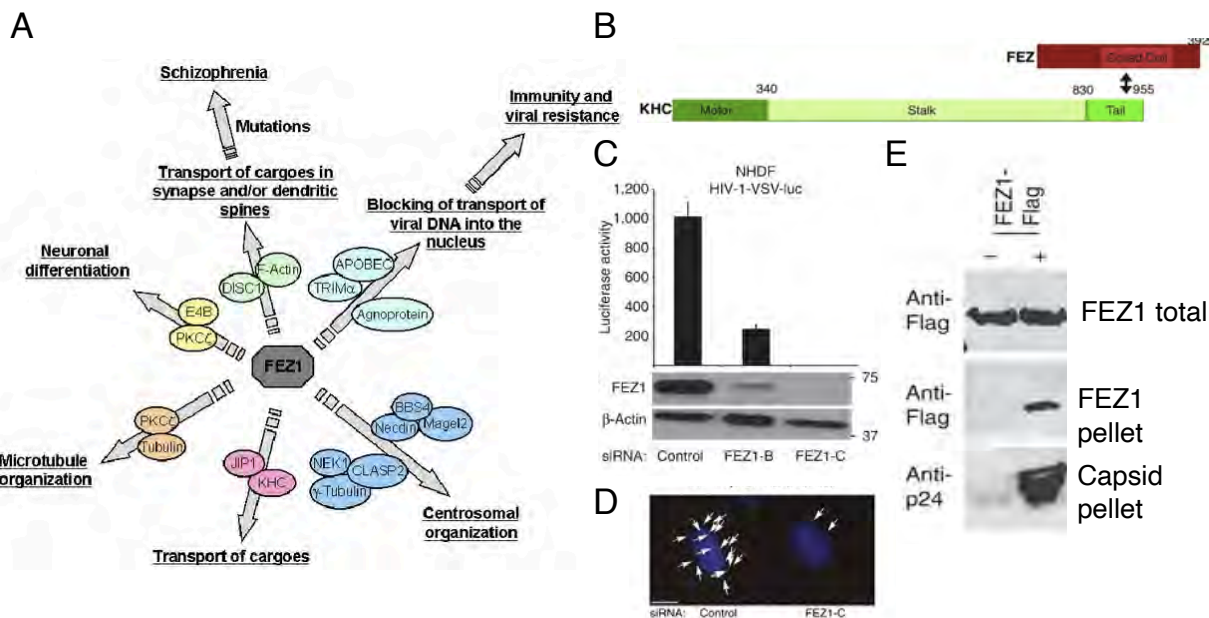


Figure 1-3 FEZ1 is a Kinesin Adaptor Protein that Promotes HIV-1 Infection

(A) FEZ1 has multiple roles in the cell. Adapted from [64]. (B) FEZ1 binds to the tail of KHC. Adapted from [61]. (C) FEZ1 knockdown strongly reduces infectivity, and (D) reduced the amount of virus particles reaching the nucleus. (E) FEZ1 co-pellets with capsid. (C-E) Adapted from [63].

1.5 Aims and Scope

During the different steps in the life cycle of HIV-1, numerous molecular motors and tubulin-associated proteins are involved. After viral entry into the host cell, capsid is thought to be transported along microtubules to nuclear pores, where the viral DNA

genome is delivered into the nucleus for integration into the host chromatin. However, the trafficking and uncoating events occurring immediately after HIV-1 entry into the host cell are complex and among the most poorly understood aspects of the viral life cycle.

Many viruses utilize the microtubule network and their associated motor proteins for transportation inside the cell. However, unlike several other viruses, evidence for direct engagement of HIV-1 with microtubule motors is lacking. From recent studies of FEZ1 and BICD2 it is now becoming evident that HIV-1 engages motors indirectly through these kinesin-1 and dynein adaptors, respectively. Outside the context of infection, FEZ1 is known to act as a kinesin-1 adaptor protein that regulates kinesin-1 activity and links it to cargos to transport vesicles and organelles along microtubules in neurons [53, 58, 61, 65, 66]. It is reported that FEZ1 interacts with the tail of kinesin-1 heavy chain using its C-terminal coiled-coil region 231-308 [61]. However, while it was recently shown that FEZ1 binds *in vitro* assembled CA-NC complexes and promotes early HIV-1 trafficking to the nucleus [63, 67], the structural basis by which HIV-1 capsids engage motor adaptors remains poorly defined. Indeed, it was not known whether FEZ1 actually directly interacts with HIV-1 capsid, and if so, which molecular determinants drive the interaction.

To investigate this FEZ1-capsid interaction and its effect on virus trafficking and infection, I made multiple truncation and mutation constructs of FEZ1 and mapped the binding regions of recombinant FEZ1 and capsid using size exclusion chromatography and pelleting assays (**chapter 2**). Using the capsid assemblies developed in our lab and from other groups, I also discovered the binding site on HIV-1 capsid (**chapter 3**). I also obtained the binding stoichiometry of FEZ1 with capsid hexamer using ITC (**chapter 4**).

Upon closer examination, I discovered that the interaction is a charge-charge interaction, and the binding site is a highly conserved region that is also important for binding of nucleotides and other small molecules (**chapter 5**). This electrostatic interaction between FEZ1 and capsid is important for the trafficking and infection of HIV-1 virus, as shown by *in vivo* virology data (**chapter 6**). Using model simulation, I further confirmed the interaction of FEZ1 with capsid hexamer (**chapter 7**). I have also made extensive attempts to obtain a high-resolution structure of the FEZ1-capsid complex (**chapter 8**). This study demonstrates that, for the first time, the key determinants required for the interaction of FEZ1 and the HIV-1 capsid core, and identified a critical role for FEZ1 in the nuclear import and infection of HIV-1. This work expanded our understanding of the interaction mode of a viral host factor, and could serve as a model for future discovery.

2 FEZ1 directly interacts with the HIV-1 capsid through negatively charged residues

2.1 Introduction

In this chapter, I set out to determine the binding site on FEZ1. The full-length human FEZ1 is a 392-amino acid protein, with a molecular weight of 45 kDa (**Figure 2-1A**). It is predicted to be a natively unfolded protein with several putative coiled-coil regions that are mostly in the C-terminus [68] (**Figure 2-1B**). The amino acid sequence of FEZ1 is notable in that it contains numerous negatively charged glutamate and aspartate residues (**Figure 2-1C**). A high concentration of negative charge is specifically present within the best behaving construct, FEZ1₉₂₋₁₉₈, although many additional charged

residues appear in the N- and C-terminal portions of the molecule. About one-third of the residues in FEZ1_{158–198} are negatively charged (underlined in **Figure 2-1C**). There is a stretch of nine out of eleven negatively charged residues (residues 181–191). I hypothesized that these acidic residues may interact with CA hexamers through electrostatic interactions. To test out this hypothesis, I mapped the binding regions of FEZ1 extensively and made different FEZ1 truncation and mutation constructs. Moreover, I was able to express and purify sufficient amounts of soluble and homogeneous FEZ1 proteins from *E. coli* (**Figure 2-1D**).

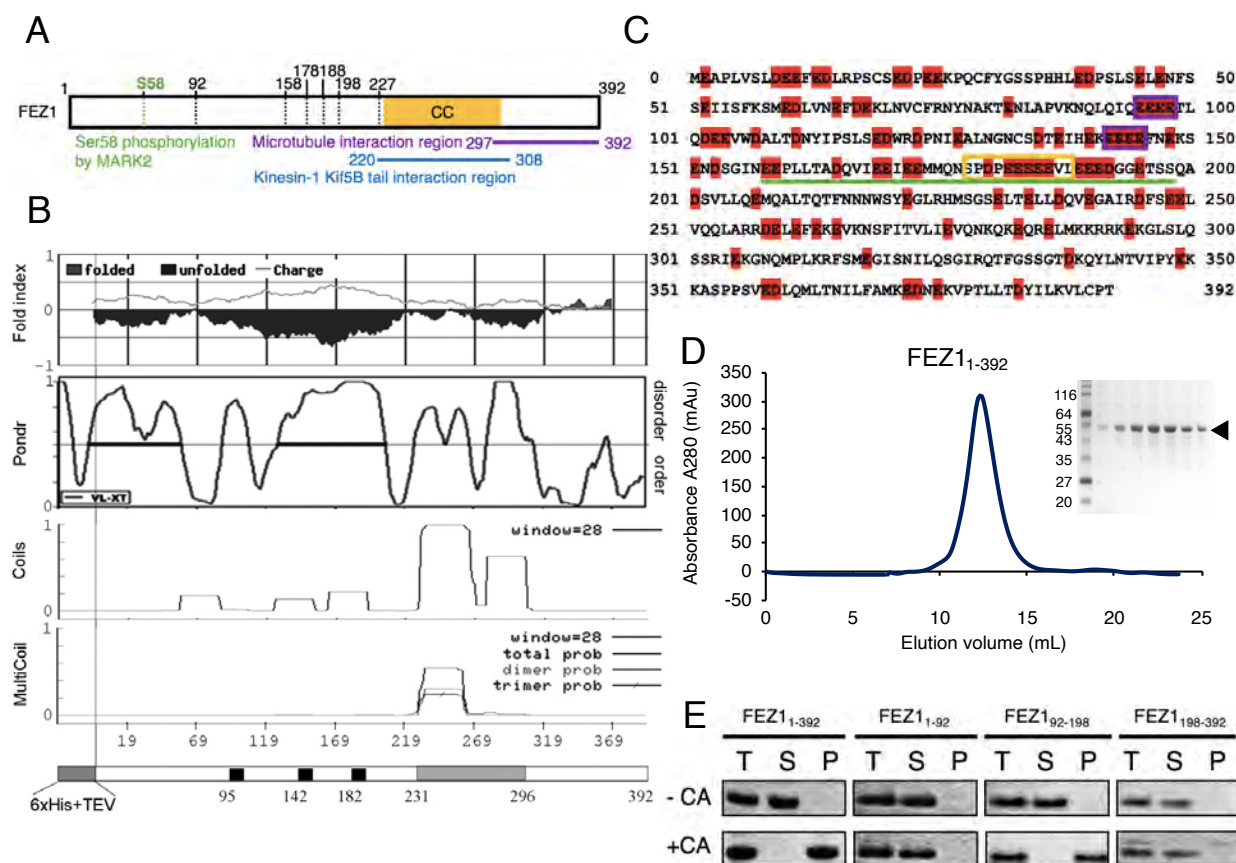


Figure 2-1 FEZ1 protein domain, purification, and capsid tube binding

(A) Schematic diagram of the FEZ1 construct (marked by the black dotted lines) used for capsid-binding assays. The yellow bar indicates the predicted coiled-coil region of FEZ1. The putative functional regions of FEZ1 are labeled with different colors. (B) FEZ1 has multiple unstructured regions. Adapted from [68]. (C) Protein sequence of the full-length FEZ1₁₋₃₉₂. Negatively-charged residues (aspartate & glutamate)

are in red. Polyglutamate regions are marked with purple underlines, FEZ1₁₇₈₋₁₈₈ is marked with a yellow box, and FEZ1₁₅₈₋₁₉₈ is underlined in green. (D) Purification of full-length FEZ1₁₋₃₉₂, it is very homogeneous and appears as a nice peak. (E) Copelleting assay of FEZ1₁₋₃₉₂, FEZ1₁₋₉₂, FEZ1₉₂₋₁₉₈, and FEZ1₁₉₈₋₃₉₂ with 14C/45C crosslinked CA tubes in 150 mM NaCl. Full-length FEZ1₁₋₃₉₂ and FEZ1₉₂₋₁₉₈ copellet with CA tubes, while the N-terminal (FEZ1₁₋₉₂) and C-terminal (FEZ1₁₉₈₋₃₉₂) regions do not. T, total load; S, supernatant; P, pellet. This is SDS-PAGE gel stained with Coomassie blue.

2.2 Results

2.2.1 FEZ1 directly interacts with the HIV-1 CA capsid

I first sought to determine if the FEZ1-capsid interaction observed from crude mammalian cell lysates is direct or if additional cofactors are required. I recombinantly expressed full-length FEZ1 (FEZ1₁₋₃₉₂) and a series of other FEZ1 truncation constructs in *E. coli* and purified them to homogeneity (**Figure 2-1D**). They generally eluted at an earlier elution volume and higher apparent molecular weight than their absolute molecular weight in size-exclusion chromatography assays, supporting the notion that they lack a compact three-dimensional structure (Note: The elution volume decreases nearly linear with the log of the molecular hydrodynamic volume. With proper column calibration using molecular weight standards, the molecular weights of unknown molecules can be measured. Molecular weight estimates by column chromatography can be quite accurate for globular proteins and less accurate for other, more linear, molecules like DNA).

I tested these FEZ1 constructs for their ability to co-pellet with *in vitro* assembled disulfide-stabilized CA tubes since these contain all intra- and inter-hexamer capsid surfaces. FEZ1₁₋₃₉₂ and constructs minimally containing FEZ1₉₂₋₁₉₈ demonstrated strong CA tube co-pelleting under physiological condition (150 mM NaCl) (**Figure 2-1E**). FEZ1 portions outside of this minimal region did not show appreciable co-pelleting. This data

clearly supports an interaction between FEZ1 and capsid that is not mediated by additional cellular factors. This is the first demonstration of a direct linkage between HIV-1 CA and an established kinesin-adaptor protein.

2.2.2 FEZ1 uses highly negatively charged residues to interact with the HIV-1 capsid protein

To map the FEZ1 region that interacts with HIV-1 capsid protein, I made different FEZ1 truncation constructs, and tested their interaction with capsid hexamers by size exclusion chromatography, and interaction with capsid tubes by pelleting assay. To begin with, I used the full length and N- or C-terminal truncation constructs of FEZ1₁₋₃₉₂, FEZ1₁₋₂₂₇, FEZ1₉₂₋₃₉₂. On the size exclusion S200GL column of capsid hexamer with FEZ1₁₋₃₉₂, there is a shift of the mixed complex peak, corresponding to the binding complex of FEZ1 with capsid hexamers (**Figure 2-2A**). I further cut off the predicted C-terminal helical region (230-306) for the construct FEZ1₁₋₂₂₇, and cut off the N-terminal flexible regions before the first polyglutamate region for FEZ1₉₂₋₃₉₂. In the pelleting assay of capsid tubes with FEZ1₁₋₃₉₂, FEZ1₁₋₂₂₇, or FEZ1₉₂₋₃₉₂, all three of these FEZ1 constructs bind to the capsid tubes (**Figure 2-2I**), so I reasoned that the interaction site on FEZ1 lies in the region of 92-227. Indeed, in the chromatogram of FEZ1₉₂₋₂₂₇ binding with capsid hexamer, the mixed complex peak showed a clear shift from the hexamer alone peak, indicating a strong binding interaction (see **Figure 5-1C, top**).

After truncation of an additional 30 residues from the C-terminus, FEZ1₉₂₋₁₉₈ still binds well to the capsid hexamer, as shown by the distinct shift of the mixed complex peak (see **Figure 3-1E**). However, cutting off more residues from the C-terminus, such

as the construct FEZ1₉₂₋₁₇₇, reduced binding interaction with capsid hexamers (**Figure 2-2B**), indicating that there are important residues for binding in the FEZ1 region 177-198. Further testing with the construct that contains the first two polyglutamate regions but not the third one, FEZ1₉₂₋₁₅₈, showed no binding to the capsid hexamer by size exclusion chromatography (**Figure 2-2C**).

To further pinpoint the capsid interaction site on FEZ1, I tested the binding interaction of the stretch FEZ1₁₅₈₋₁₉₈, and found that the mixed complex peak also shifted to larger molecular weights, indicating this region of FEZ1 is binding tightly with hexamers (**Figure 2-2D**). However, when I cut off residues and made FEZ1₁₅₈₋₁₈₂, it severely reduced binding to capsid hexamers in size exclusion chromatography, indicating that the negatively charged glutamate residues after 182 are important for binding (**Figure 2-2E**). This was further confirmed by mutating the glutamate residues ¹⁸²EEEEEE¹⁸⁶ to ¹⁸²AAAAA¹⁸⁶ on FEZ1₁₅₈₋₁₉₈ and FEZ1₉₂₋₁₉₈ (FEZ1₁₅₈₋₁₉₈ ¹⁸²EA/FEZ1₉₂₋₁₉₈ ¹⁸²EA) (**Figure 2-2G&H**). This mutation greatly reduced the interaction of FEZ1 with capsid hexamer, and much less shift of the mixed complex peak compared to FEZ1₁₅₈₋₁₉₈ WT or FEZ1₉₂₋₁₉₈ WT binding with hexamer. Subsequent mapping identified the highly negatively charged FEZ1₁₇₈₋₁₈₈ region (¹⁷⁸SPDPEEEEEVL¹⁸⁸) to be the minimal construct that retained strong interaction with CA hexamers (**Figure 2-2H**).

The above results show that the major capsid-binding region of FEZ1 is located in the second polyglutamate region 178-188, where the molecule is highly negatively charged.

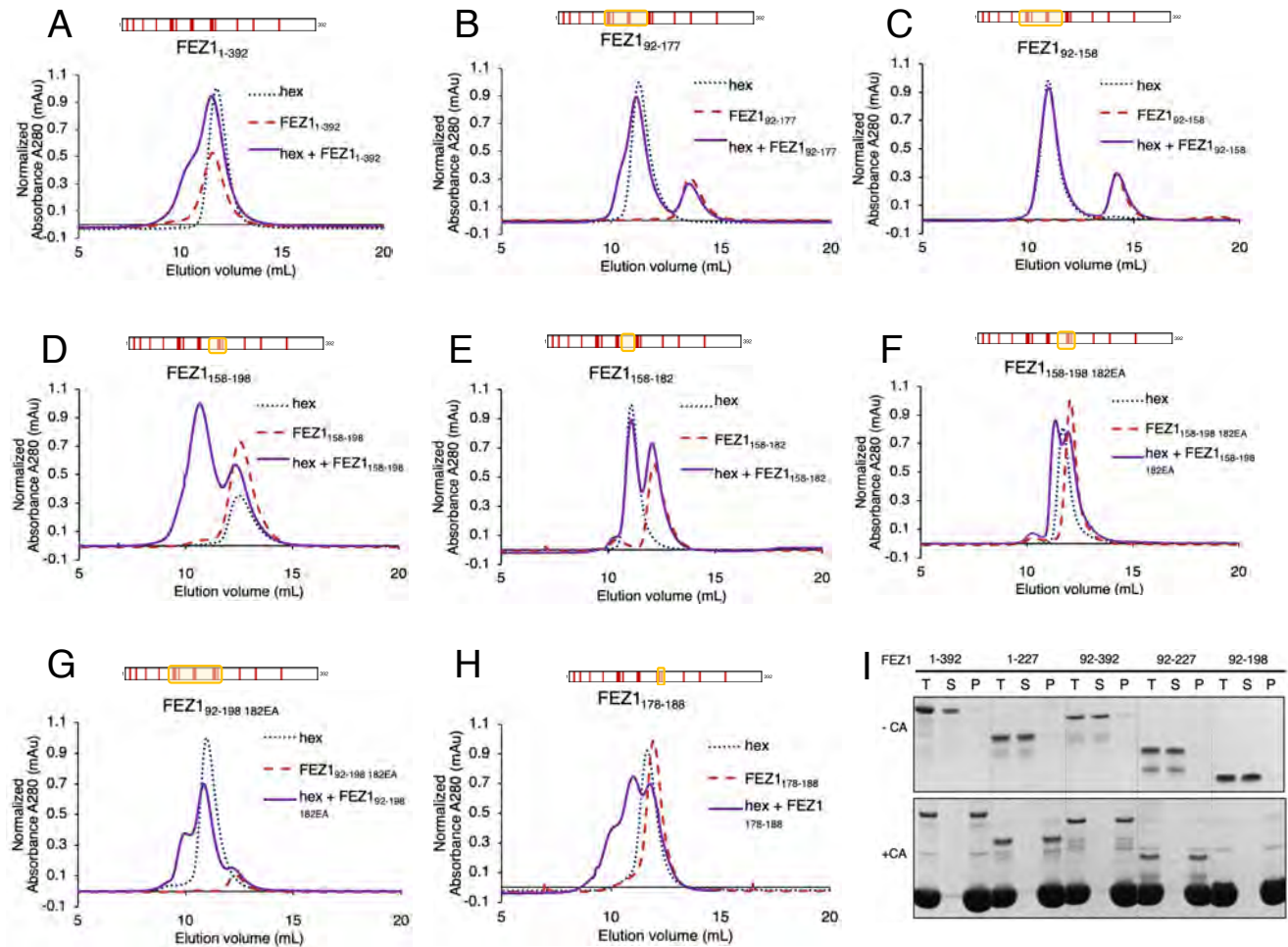


Figure 2-2 Mapping the capsid binding region on FEZ1

(A-H) SEC binding assays of different FEZ1 constructs with the CA hexamer. (A) Full -length FEZ1₁₋₃₉₂ interacts with capsid hexamer, having a shift indicated by the left shoulder that appeared in the mixture. (B) Cutting off till the residue 177, FEZ1₉₂₋₁₇₇, greatly reduced the binding interaction of FEZ1 with capsid hexamers. (C) FEZ1₉₂₋₁₅₈ and (E) FEZ1₁₅₈₋₁₈₂ does not co-elute with CA hexamer, while (D) FEZ1₁₅₈₋₁₉₈ does. (F & G) FEZ1_{158-198 182EA} and FEZ1_{92-198 182EA}, both with five consecutive glutamate residues 182EEEEEE₁₈₆ mutated to alanines, shown reduced interaction with CA hexamer. (H) Co-elution of FEZ1₁₇₈₋₁₈₈ with CA hexamer in the SEC binding assay. FEZ1₁₇₈₋₁₈₈ is MBP-tagged. Schematics of the FEZ1 constructs are boxed in yellow and shown on top of the chromatograms. Red bars indicate the negatively-charged residues of FEZ1.

2.3 Discussion

Viral capsids are the major interacting sites for viral intracellular transport, and many viruses including HIV-1 will utilize the MT and associated motors for transportation inside the cell. FEZ1, which is highly charged and flexible, is characterized as a “hub”

protein and are shown to interact with over 80 proteins, such as the synaptotagmin, SCOCO, JC virus agnoprotein, and Disc1 [58, 62, 69, 70], and many of these interactions involve the FEZ1 C-terminal coiled-coil region 231-308 [54, 71, 72]. Here, I further discovered that the FEZ1 region 178-188 also serves as an interaction site for cargoes such as virus capsid. I showed that kinesin-1 adaptor protein FEZ1 directly interacts with cross-linked HIV-1 capsid hexamers and *in vitro* assembled HIV-1 capsid tubes through highly negatively charged residues. By making different FEZ1 truncation and mutation constructs, I found that the region 178-188 is the major FEZ1 interaction site with capsid protein, and mutating this region significantly reduces binding in size exclusion chromatography binding assays. Interestingly, this stretch of highly negatively charged residues are not conserved in the *C. elegans* UNC-76 or human Fez2 protein [73], suggesting that this is a more recently acquired region in evolution.

3 Determination of the HIV-1 capsid binding of FEZ1: FEZ1 interacts with the capsid hexamer

3.1 Introduction

Now that I know that FEZ1 is using a highly negatively charged region to interact with HIV-1 capsid, I would like to know with what region in the HIV-1 capsid FEZ1 is interacting. To determine this, we used several capsid assemblies that were established by our group and others [74, 75]. The binding assays of FEZ1 with capsid assemblies were done by a fellow graduate student Brady Summers, and myself.

3.2 Results

3.2.1 FEZ1 specifically recognizes the HIV-1 capsid hexamer

To better define the specific capsid surface targeted by FEZ1, we used size-exclusion chromatography (SEC) co-elution assays to test for interactions between FEZ1₉₂₋₁₉₈ and a variety of soluble CA assemblies. We primarily used the FEZ1₉₂₋₁₉₈ construct due to its superior expression and behavior in solution compared to full-length FEZ1. For CA assemblies, we first tested the established native CA monomers/dimers and disulfide-stabilized CA pentamers and hexamers [30, 76]. In addition, we developed an extensive library of stabilized CA oligomers that recapitulate the unique intra- and inter-hexamer surfaces found in the assembled capsid lattice [75]. These new CA oligomers include a series of “partial-hexamer” assemblies, which subdivide the CA hexamer into smaller fragments, such as 1/3- and 1/2-hexamers. 1/3- and 1/2-hexamers contain two and three disulfide-linked CA monomers, respectively, arranged with six-fold rotations just as they are in complete hexamers. 1/2-hexamer assemblies are discrete in solution, but have the ability to dimerize into complete hexamers in certain conditions. This hexamer formation can be prevented by the addition of A42E/T54E mutations at exposed intra-hexamer surfaces (termed 1/2-hexamer-EE). Furthermore, we engineered a new CA hexamer that contains six CA molecules arranged as a trimer of dimers. This structure contains the three-fold inter-hexamer interface and is stabilized by a fusion to the naturally trimeric bacteriophage T4-foldon domain (termed hexamer-2_{foldon}).

Our comprehensive CA assembly library allowed us to unambiguously establish that FEZ1 specifically recognizes the CA hexamer, which is considered to be the

repeating unit of the capsid lattice. We first tested for FEZ1₉₂₋₁₉₈ binding to native CA monomers/dimers, but observed no co-elution between them (**Figure 3-1A**). Similarly, we observed no co-elution between FEZ1₉₂₋₁₉₈ and either 1/3-hexamers or 1/2-hexamers that contained hexamer-preventing mutations (**Figure 3-1B&C**). In contrast, we consistently observed complete co-elution between FEZ1₉₂₋₁₉₈ and CA hexamers (**Figure 3-1E**). A lack of interaction with CA dimers or partial hexamers, yet strong recognition of hexamers, demonstrates a novel FEZ1 capsid-lattice sensing ability. Interestingly, we also detected strong FEZ1₉₂₋₁₉₈ co-elution with the 1/2-hexamer assembly that is competent to dimerize into a hexamer. The observed elution profile closely resembles that of the hexamer-FEZ1 complex, suggesting that FEZ1 is able to bridge two 1/2-hexamers into a hexamer (**Figure 3-1D**). These data further reinforce the idea that FEZ1 targets a complete CA hexamer. In addition, FEZ1 does not appear to require inter-hexamer surfaces for binding, as no co-elution was observed with hexamer-2_{foldon}, which contains native two- and three-fold inter-hexamer interfaces (**Figure 3-1F**). These data demonstrate that FEZ1 targets a highly specific surface pattern only found in complete hexamers. Importantly, a binding mode of this nature has not been described for other capsid-binding proteins.

3.2.2 FEZ1 does not bind to HIV-1 capsid pentamer

The capsid core is composed of twelve pentamers, with five pentamers on the narrow end and seven pentamers on the wide end to close the curvature [29]. After seeing that FEZ1 interacts with capsid hexamers, I was curious whether or not it binds to pentamers. The pentamers used here are the crosslinked N21C/A22C pentamers from

published literature [30]. Despite their structural similarity to hexamers, I observed no FEZ1 co-elution with CA pentamers, indicating there is no observable binding of FEZ1 to capsid pentamers (**Figure 3-1G**).

3.3 Discussion

HIV-1 capsid is made from CA monomer proteins that arrange into mostly hexamers which further assemble into higher order oligomers such as conical shaped capsid cores or capsid tubes [77, 78]. The structures of HIV-1 CA dimer, pentamer, and hexamer have been solved [30, 79, 80], as well as the assemblies of capsid tubes and capsid cones [9, 78, 81]. Here, we have shown that FEZ1 interaction with capsid requires the capsid hexamer interface, in contrast to TRIM or MxB proteins that may require the tri-hexamer interface or binding across multiple hexamers [75, 82]. Moreover, I also found that FEZ1 does not interact with pentamers, which is slightly different in the angle between adjacent CA NTDs (hexamer: 60° ; pentamer and 72° , with the angle vertex at the center of each ring) [30]. Model simulation of HIV-1 capsid stability shows that pentamers are more rigid than hexamers [83], therefore possibly it is harder to accommodate the interactions with FEZ1. Also, the binding of chloride ions in the central pore, near R18, is tighter to pentamers than to hexamers, which could be another possible explanation of no interaction between FEZ1 and pentamers [83].

In summary, I showed that FEZ1 is not interacting with the crosslinked CA pentamer by SEC, further confirming that FEZ1 recognizes specifically the capsid hexamer [30].

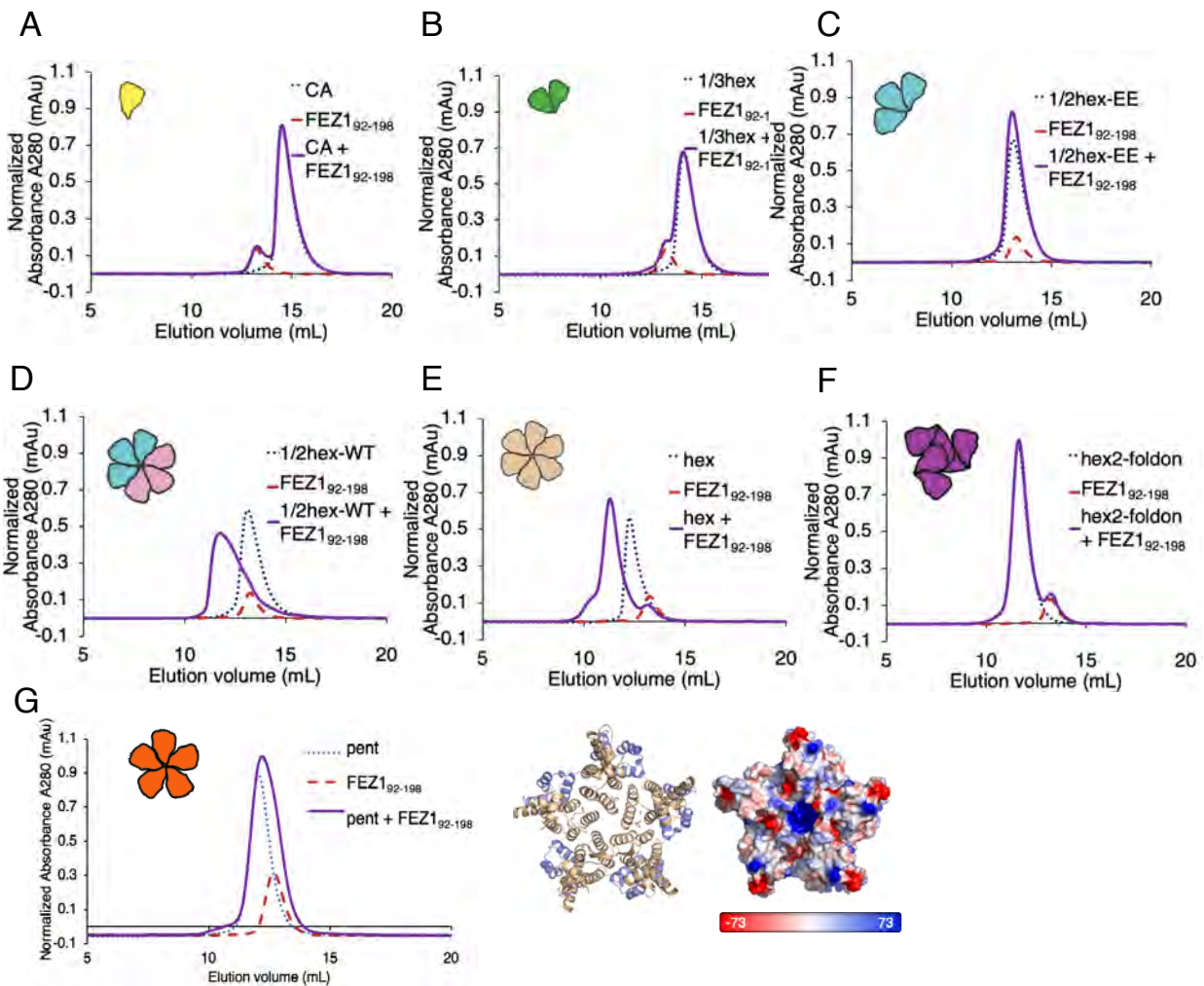


Figure 3-1 FEZ1 uses negatively-charged poly-glutamate regions to bind CA hexamers

(A-F) Size-exclusion chromatography (SEC)-binding assay of FEZ1₉₂₋₁₉₈ with different CA assemblies (schematics shown in cartoon insets). The concentrations of FEZ1 and CA monomer in each binding reaction were 33 and 98 μ M, respectively. FEZ1₉₂₋₁₉₈ does not coelute with CA monomer (A), 1/3-hexamer (B), or 1/2-hexamerEE (C) in SEC assays. There is no elution shift of the mixture (solid purple) relative to the individual components (dotted lines). FEZ1₉₂₋₁₉₈ does coelute with the CA hexamer (D), and restoration of a hexamer from two 1/2-hexamers (cyan and pink cartoons) restores FEZ1₉₂₋₁₉₈ coelution (E), which coelutes at the same position as with CA hexamers. In contrast, FEZ1₉₂₋₁₉₈ does not coelute with hexamer-2foldon (purple cartoon), which also contains 6 CA subunits but arranged around the 3-fold capsid interface (F).

4 Determining the binding parameters of FEZ1 with HIV-1 capsid using ITC

4.1 Introduction

The SEC binding assay offers a quick, qualitative means to detect complex formation. However, it is only applicable to relatively stable complexes with binding affinity (dissociation constant, K_d) at the nanomolar or low micromolar range. To measure the binding interactions between proteins quantitatively, isothermal titration calorimetry (ITC) is an ideal method, because no fluorophores or chromophores are needed. Moreover, it gives the quantitative binding information - the binding association constant K_a , Gibbs free energy change ΔG , the enthalpy change of binding ΔH , the entropy change of binding ΔS , and the binding stoichiometry n – in one single run. Therefore, to quantitate the binding of FEZ1 with capsid hexamers thermodynamically, I used ITC to confirm the binding of FEZ1 92-198 protein with capsid hexamers.

4.2 Results

To get the measurement of the binding stoichiometry and metrics of FEZ1 with capsid, I started with the most well-behaved FEZ1 construct, FEZ1₉₂₋₁₉₈. The binding of FEZ1₉₂₋₁₉₈ with CA hexamers is endothermic with a dissociation constant (K_d) of 300 ± 60 nM (**Figure 4-1A&D**). The hexamer binding affinity of the FEZ1₉₂₋₁₉₈ 182EA mutant was reduced by approximately an order of magnitude ($2.5 \mu\text{M}$), highlighting the importance of the poly-glutamate peptide sequence (**Figure 4-1B&D**). The binding stoichiometry was measured at slightly over one CA hexamer to FEZ1 ($n=1.3 \pm 0.1$ for FEZ1₉₂₋₁₉₈ and $n=1.6 \pm 0.2$ for FEZ1₉₂₋₁₉₈ 182EA), partly due to the existence of multiple CA hexamer-binding sites

within FEZ1 (one major and multiple additional weak sites, see below). When the minimal FEZ1₁₇₈₋₁₈₈ construct containing the major CA hexamer-binding site is used, a comparable affinity was observed (K_d of 180 ± 40 nM), with a 1:1 CA hexamer to FEZ1₁₇₈₋₁₈₈ stoichiometry ($n=1.0 \pm 0.2$) (**Figure 4-1C&D**).

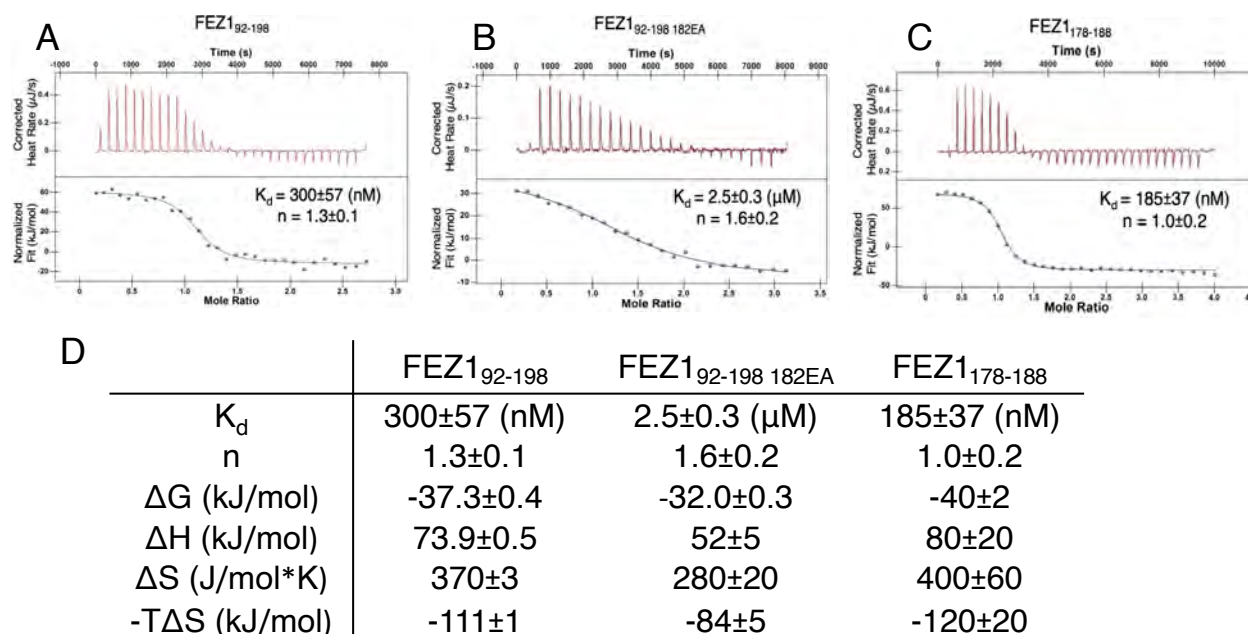


Figure 4-1 Determining the binding parameters of FEZ1 with HIV-1 capsid using ITC

(A-C) Representative ITC curves of FEZ1₉₂₋₁₉₈ (A), FEZ1_{92-198 182EA} (B) and FEZ1₁₇₈₋₁₈₈ (C) with the CA hexamer. (D) Summary table of the ITC data of the binding of FEZ1₉₂₋₁₉₈, FEZ1₁₇₈₋₁₈₈, and FEZ1_{92-198 182EA} with the CA hexamer. Data are from three independent experiments, and are represented as mean \pm SD.

4.3 Discussion

My ITC results showed strong binding between FEZ1 and capsid hexamer. Remarkably, this binding affinity is at least an order of magnitude higher than previously analyzed capsid-binding proteins such as CypA, TRIM5 α , TRIMCyp, CPSF6, and Nup153 [84-88], making FEZ1 the strongest CA hexamer binder known to date. This binding interaction of FEZ1 with capsid hexamer is entropically driven, having similar

characteristics to the first-generation HIV-1 inhibitors (indinavir, nelfinavir, saquinavir and ritonavir), with a strong favorable entropy change and less favorable enthalpy change [89, 90]. This result might at first sight seem contradictory to our result of the importance in charge-charge interaction between the highly negatively charged FEZ1 and the positively charged R18 center of the capsid hexamer. However, this could be explained by the displacement of water molecules upon binding. The entire capsid interface contains numerous water molecules, bridging the polar sidechains and backbone atoms, forming an extensive hydrogen-bonding network that characterizes the retroviral CA hexamer interfaces [14, 91]. Furthermore, a recent study has showed that there is binding of sodium and chloride ions over the entire capsid, and specifically there is binding of chloride ions at the center of the hexameric rings [83], consistent with previous studies [11]. Therefore, the charge-charge interaction between FEZ1 and capsid R18 could be displacing the water or ion molecules that were stabilizing the ring of arginine residues in the center of the CA hexamer, resulting in favorable entropic effect for binding. Moreover, FEZ1 on its own is an intrinsically disordered protein, predicted to be elongated and flexible. Although FEZ1 could become more structured upon binding with capsid, stabilizing the flexible capsid CA hexamers, the loss of conformational degrees of freedom associated with binding could be compensated by the displacement of water molecules on the binding interface upon binding. A detailed molecular structure of the complex would provide more insight into the interactions between FEZ1 and capsid hexamer. Therefore, the overall favorable entropy change is because of the large entropy gain from displacement of water, and the small conformational entropy loss [92, 93].

5 FEZ1 binds to capsid through charge-charge interaction using a highly conserved viral cofactor binding site

5.1 Introduction

In chapter 3, we used different capsid assemblies to examine what is the capsid binding interface that interacts with FEZ1, and found that FEZ1 specifically recognizes the capsid hexamer interface. As FEZ1 uses a highly negatively charged region to interact with the CA hexamer, I examined the CA hexamer surface electrostatic potential distribution to identify the region bound by FEZ1. Importantly, there is a ring of positively charged R18 residues lining the center pore of the capsid hexamer (**Figure 3A**). In this chapter, I examined the role of these R18 residues.

5.2 Results

5.2.1 Charge-charge interactions are important for FEZ1-capsid interaction: R18

I investigated the importance of this highly positively charged region by mutating R18 to an oppositely-charged residue (R18D) (**Figure 5-1A**). To verify that the R18D mutation does not affect the conformation of the CA hexamer, I determined the crystal structure of the R18D CA hexamer at 2.1 Å resolution. Structural comparison between the R18D and wild-type CA hexamers reveals minimal structural changes as measured by the root mean squared differences (RMSD) of ~0.5 Å for all six CA molecules (**Figure 5-1B,E,F, Table 1**). I further confirmed that the R18D mutation does not affect the

morphology of CA tubes as shown by electron microscopy (EM) of negatively-stained samples (**Figure 5-1G**).

Introduction of the R18D mutation drastically reduced the recognition of CA hexamers by FEZ1, while no reduction in binding was observed in mutations of other capsid host factor-binding sites. In both SEC co-elution assays and CA tube co-pelleting assays the R18D mutation substantially reduced FEZ1 binding (**Figure 5-1C&D**). To further confirm that the loss of FEZ1 binding is not due to destabilization of the R18D hexamer by negative charge repulsion at the R18D center pore, I tested FEZ1 binding to the neutral mutant R18A CA tubes. A similar reduction in FEZ1 binding was also observed with the conservative R18A CA mutation (**Figure 5-1H**), supporting a direct binding at the R18 site rather than an indirect destabilization effect by R18D.

| | |
|--|---------------------------|
| Data collection | |
| Space group | P6 |
| Cell dimensions | |
| <i>a</i> , <i>b</i> , <i>c</i> (Å) | 90.66, 90.66, 56.58 |
| α , β , γ (°) | 90.0, 90.0, 120.0 |
| Resolution (Å) | 45.90–2.05 (2.09-2.05) |
| R_{sym} or R_{merge} | 0.134 (1.34) |
| Mean I/σ | 12.2 (1.7) |
| Completeness (%) | 99.9 |
| Redundancy | 5.5 (5.1) |
| CC ^{1/2} (%) | 39.7 |
| Refinement | |
| Resolution (Å) | 2.05 |
| No. of reflections | 15594 |
| $R_{\text{work}}/R_{\text{free}}$ | 0.174/0.221 (0.241/0.296) |
| No. of atoms | |
| Protein | 1692 |
| Water | 218 |
| B-factors | |
| All atoms (Å ²) | 33.0 |
| R.m.s. deviations | |
| Bond lengths (Å) | 0.007 |
| Bond angles (°) | 0.9 |
| Ramachandran | |
| Preferred | 98.1% |
| Allowed | 1.9 % |
| Outliers | 0.0 % |

Table 1 Data collection and refinement statistics for the R18D CA crystal structure.
Values shown in parentheses are for highest-resolution shell.

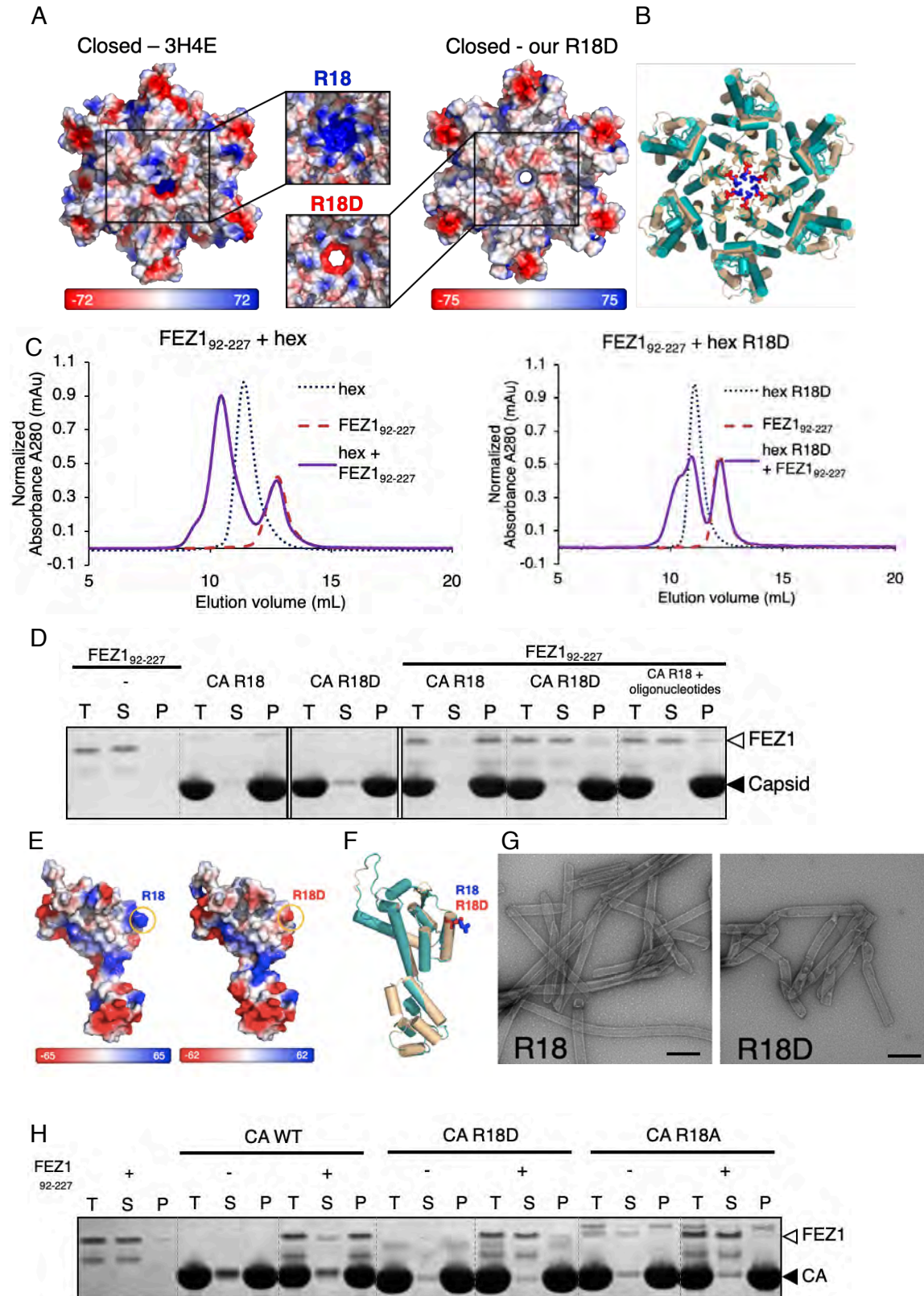


Figure 5-1 FEZ1 recognizes the positively charged center pore of CA hexamers through electrostatic interactions

(A) Comparison of the electrostatic potential surfaces of R18D (right) and WT (left) CA hexamers in the closed state (PDBID: 3H47), as viewed from outside of the capsid (red: negative charge; blue: positive charge). The unit of the electrostatic potential map is $k_B T/e$. Zoomed-in views of the hexamer center pores are shown in the middle inset, where the β -hairpin is not shown for clarity of the charges of the R18 (top) and R18D (bottom) pores. (B) Left, overlay of the crystal structures of the WT CA hexamer (cyan) with the R18D CA hexamer (tan). The mutation does not change the hexamer structure. Right, electrostatic potential surface of the R18D CA hexamer shows the negatively charged center pore. (C) The R18D mutation substantially reduced the binding of FEZ1₉₂₋₂₂₇ with CA hexamer in SEC binding assays (top), compared to the CA hexamer R18 (bottom). (D) The R18D mutation drastically reduced the co-pelleting of FEZ1 with CA tubes. T: total load; S: supernatant; P: pellet. (E) Comparison of crystal structures of WT and R18D CA molecules. Electrostatic potential surface of WT (left) and R18D (right) CA. Blue, positive charge; red, negative charge. The positions of R18 and R18D are marked by orange circles. The unit of the electrostatic potential map is $k_B T/e$. (F) Overlay of the two structures WT CA (cyan, PDBID: 3H47) and R18D CA (tan). R18 is in blue and R18D is in red. (G) Negative-stain electron microscopy micrographs of crosslinked CA tubes of WT CA (left) and R18D CA (right). Scale bar, 200 nm. (H) R18A also reduces interaction of FEZ1 with CA tubes. Mutation of the center ring R18 of the capsid to either aspartate or alanine reduced the interaction of FEZ1₉₂₋₂₂₇ with CA tubes, as compared with the WT CA tubes. (D & H) SDS-PAGE gel stained with Coomassie blue.

The β -hairpin region of R18D CA adopted the closed conformation [94] under our crystallization conditions. A comparison of the R18D CA hexamer structure with known CA hexamer structures in the open or closed state is shown in **Figure 5-2**. It has been reported that the β -hairpin is highly dynamic, with a predominantly open conformation at $\text{pH} < 7$ and a closed conformation at $\text{pH} > 7$ [94]. I tested if the pH-dependent open and closed β -hairpin conformations affect FEZ1 binding by carrying out binding assays at pHs 6, 7 and 8. The results showed that in all three conditions, FEZ1 was able to interact with the CA tubes at a similar level (**Figure 5-3**). This is likely due to the dynamic nature of the CA β -hairpin and the conformational flexibility of FEZ1, which is predicted to be unstructured in its unbound form. It is conceivable that the binding energy of FEZ1 enables a shift in the equilibrium toward the open conformation of the CA β -hairpin, so that FEZ1 is able to reach into the R18 pore for a stable interaction. This hypothesis is supported by our molecular dynamics simulation shown in Chapter 7, demonstrating that FEZ1's ability to access the hexamer center pore.

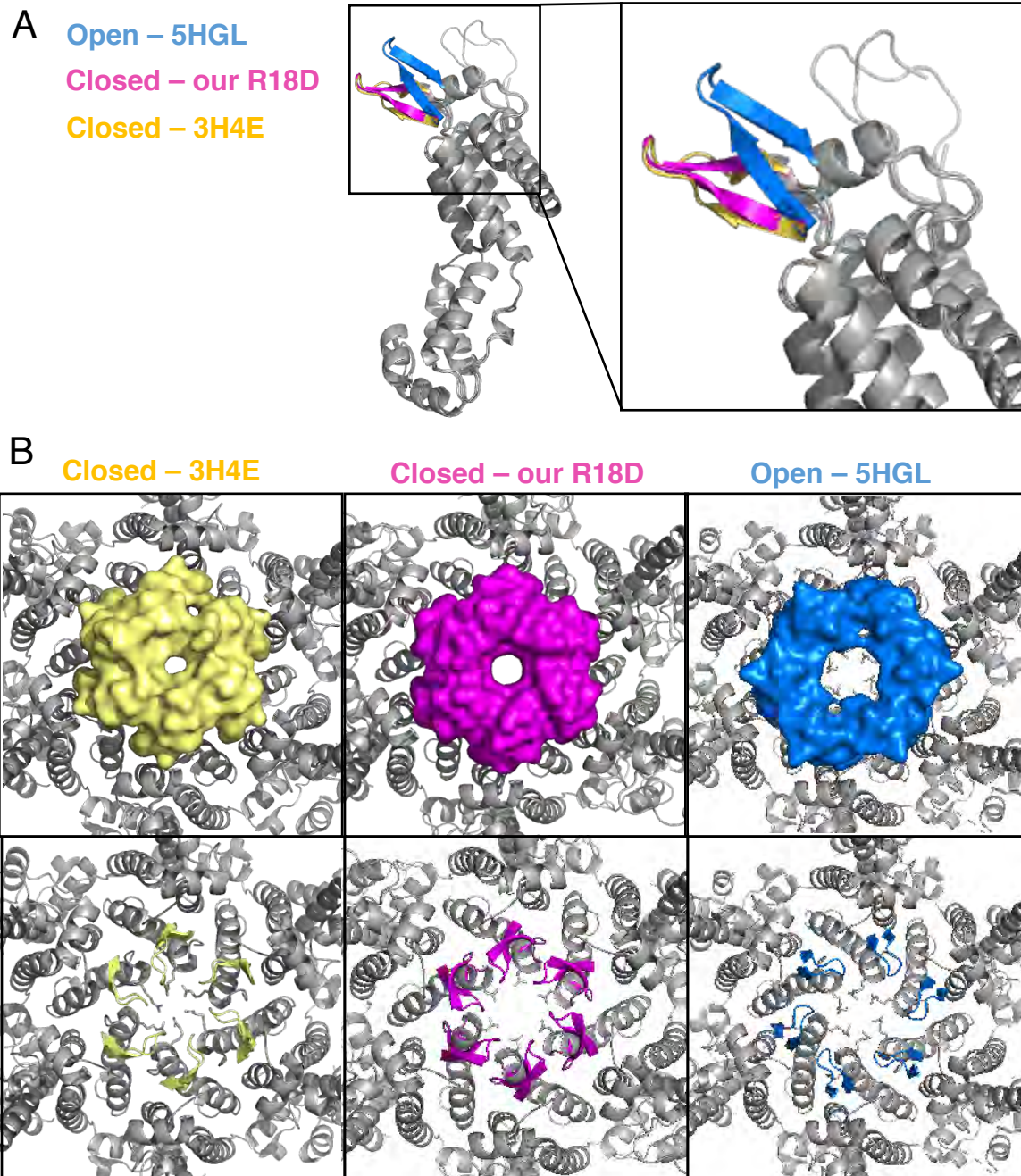


Figure 5-2 Comparison of structures of the WT and R18D CA Hexamers with the open or the closed conformation of the b-hairpin.

(A) Overlay of the two WT CA structures, open (blue, PDBID: 5HGL) and closed (yellow, PDB: 3H4E) forms, and the current R18D CA structure (magenta). (B) Comparison of the open (right) and closed (left) β -hairpin conformations, showing the pore at the center of the CA hexamer. R18 or R18D is shown as stick pointing into the center. The β -hairpin is in surface representation in the top rows and in cartoon representation in the bottom rows.

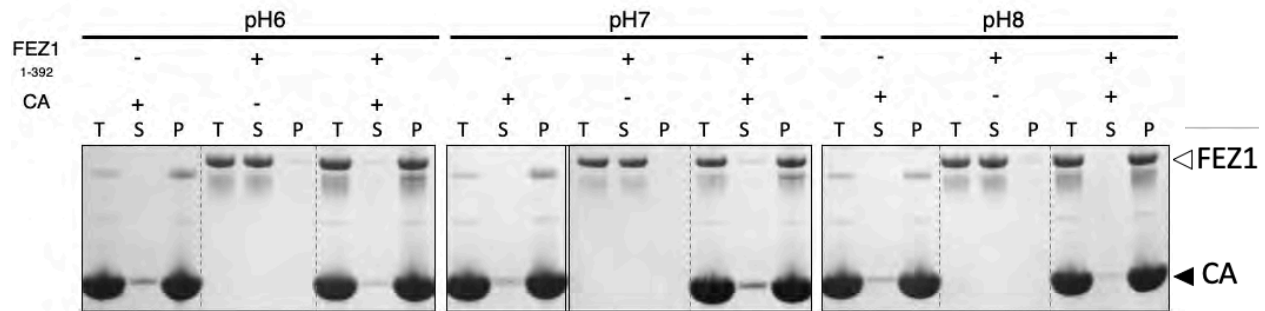


Figure 5-3 FEZ1 pelleting assay with CA tubes at different buffer pH. Under different buffer pHs, pH = 6, 7, 8, FEZ1 all interacts with CA tubes.

5.2.2 Mapping additional binding sites on the capsid hexamer: G89, P90, P207, G208, T210

To determine if FEZ1 uses other established host factor-binding sites on capsid I additionally tested FEZ1-CA tube co-pelleting with a variety of capsid mutations known to reduce capsid recognition by the host protein CypA (G89V and P90A) and the restriction factor MxB (P207S, G208R, and T210K) (**Figure 5-4A**) [95-99]. Importantly, none of the aforementioned mutations reduced the FEZ1 CA-tube interaction (**Figure 5-4B**). These results show that a specific electrostatic interaction at the hexamer center is necessary for FEZ1-capsid interactions.

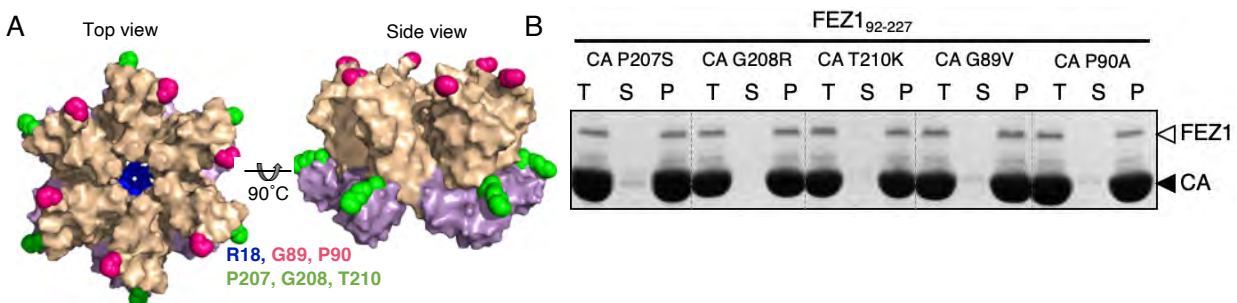


Figure 5-4 Mapping additional binding sites on the capsid hexamer

(A) Orthogonal views of the residues that are mutated on the CA hexamer. Green, residues implicated in escaping MxB restriction (P207 G208, T210); Yellow, residues important for CypA binding (G89, P90); R18 is in blue. (B) Mutations of the residues important for MxB function or CypA binding do not affect FEZ1 co-pelleting with CA tubes.

5.2.3 FEZ1 interacts with a conserved viral co-factor capsid binding site: NTP/dNTP & IP6, SUN2

To date, no other host proteins have been described to bind at the CA hexamer center using the R18 residue. However, R18 has recently been shown to be critical in the binding and translocation of nucleotides into the capsid for reverse transcription [94] and in the binding of the small molecule cofactor IP6 for maturation and stability of capsid [100, 101]. To further support my hypothesis that FEZ1 binds in this region of the CA hexamer I performed competition assays using either ATP, dNTPs, or IP6 to compete with FEZ1 for CA tube co-pelleting (**Figure 5-5 A-C**). As expected, the addition of any nucleotides or IP6 reduced FEZ1-CA tube interaction in a concentration dependent manner. These data substantiate FEZ1 as the first protein known to bind to the same conserved, highly-positively charged hexamer center targeted by important small-molecule cofactors.

The nucleotide and IP6 titration result also demonstrates that FEZ1 has the ability to bind capsid under physiological conditions. Full-length FEZ1 retained CA tube binding in the presence of up to 5mM ATP and 200 μ M IP6 (**Figure 5-5 A&B**), which are the cellular concentrations of these molecules. The binding was diminished or abolished at higher cofactor concentrations. Interestingly, the construct containing a minimal binding motif (FEZ1₁₇₈₋₁₈₈), which interacts with CA hexamers at a high affinity (**Figure 5-5 A&B**), lost its binding to CA tubes at 20 μ M ATP or 20 μ M IP6 (**Figure 5-5 A&B**). This effect at a low ATP/IP6 concentration suggests that the loss of binding is a consequence of a direct

competition at the hexamer center where these cofactors interact, rather than an indirect charge screening effect of these charged molecules at high concentrations.

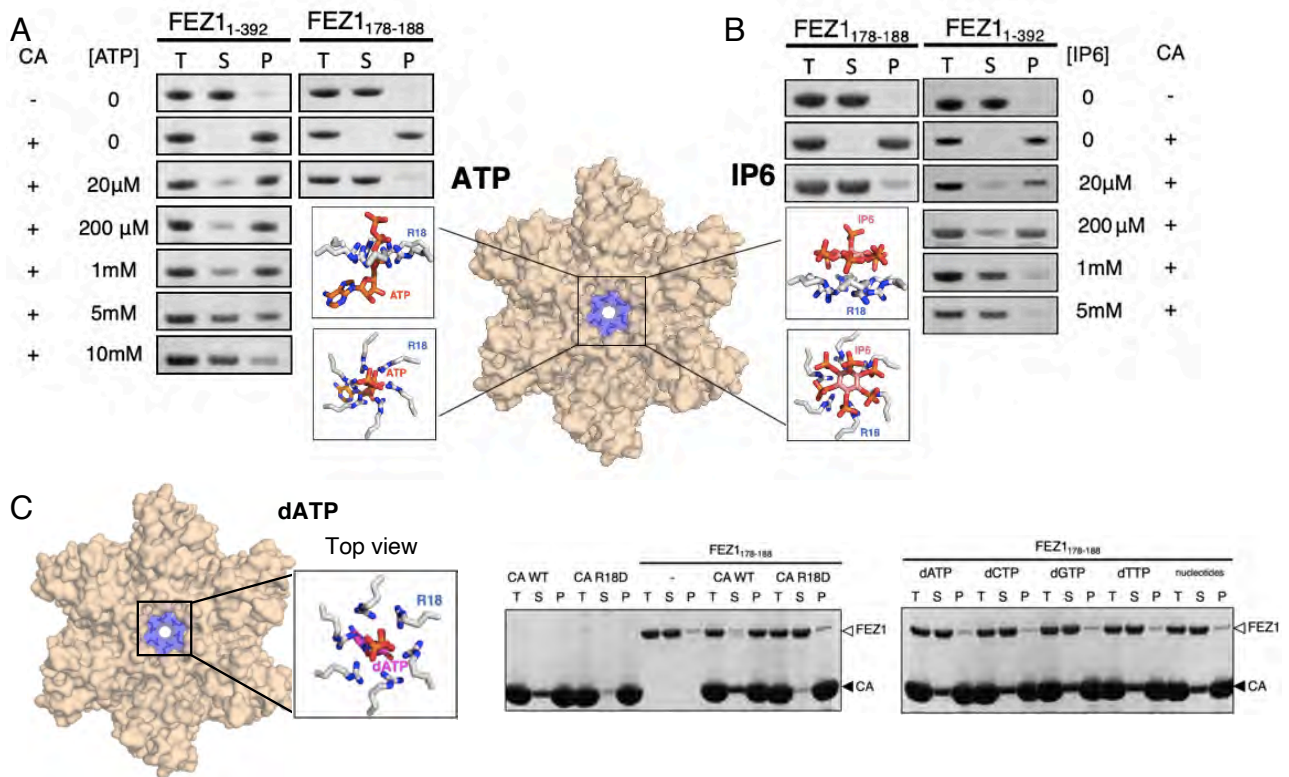


Figure 5-5 Electrostatic interaction is important for FEZ1 binding with CA hexamer

(A, B) Co-pelleting assays showing the binding of FEZ1 constructs to CA tubes at increasing ATP (A) or IP6 (B) concentrations. Only the FEZ1 bands are shown for clarity. FEZ1₁₋₃₉₂ is able to bind with CA tubes in the presence of physiological levels of ATP/IP6, and the increase of ATP/IP6 decreased binding. The binding of FEZ1₁₇₈₋₁₈₈ to CA tubes is nearly abolished at 20 μM ATP/IP6, even though it has high affinity to individual CA hexamers. This difference is consistent with the avidity effect from multiple capsid-binding sites in full-length FEZ1. Center inset: Structural illustrations of ATP (left, PDBID: 6ERN) and IP6 (right, (PDBID: 6HBS) binding to the CA hexamer (middle) center residues R18 (blue). (C) Left: Schematic of dATP binding with the center R18 residues of the CA hexamer (PDBID: 5HGM). Middle and right: Co-pelleting assay showing that the binding of Fez1₁₇₈₋₁₈₈ to CA tubes are abolished by R18D mutation of CA (middle) and various dNTPs (bottom), consistent with binding at the CA hexamer center.

5.2.4 Secondary binding sites provide avidity and enhance FEZ1-capsid interaction

It may appear intriguing that full-length FEZ1 required much higher NTP or IP6 concentrations to abolish binding to CA tubes than that needed for FEZ1₁₇₈₋₁₈₈; the latter showed high-affinity binding to CA hexamers similar to longer FEZ1 constructs (**Figure**

4A,C,D). In fact, these data suggest that FEZ1 contains multiple CA hexamer-interacting regions. In my SEC and ITC assays using the CA hexamer as the binding partner, which has a single targeting site, the minimal FEZ1₁₇₈₋₁₈₈ interacted as effectively as the longer constructs. In contrast, when using CA tubes that contain many hexamer-targeting sites, the simultaneous binding by multiple regions in full-length FEZ1 allows for a much stronger interaction through the avidity effect. The FEZ1 sequence indeed contains numerous highly negatively charged patches throughout the molecule (**Figure 2-1C**). Our data demonstrated effective CA tube binding by FEZ1₉₂₋₁₉₈ (**Figure 2-1E**), which likely contains multiple interaction sites in addition to the strong binding region in FEZ1₁₇₈₋₁₈₈. Although the N- and C-terminal regions (FEZ1₁₋₉₂ and FEZ1₁₉₈₋₃₉₂) did not bind CA tubes under the conditions tested (150 mM NaCl) (**Figure 5-6C**), the abundance of negatively charged segments in these regions indicates that they potentially contain auxiliary weaker binding sites.

To further test the hypothesis that FEZ1 contains multiple capsid-binding sites, I performed SEC binding assays at low ionic strength conditions under which the low-affinity electrostatic interactions can sustain. Even at a low salt condition of 50 mM NaCl, FEZ1₁₋₉₂ and FEZ1₁₉₈₋₃₉₂ did not co-elute with CA hexamers in SEC binding assays (**Figure 5-6A&B**). However, they effectively co-pelleted with CA tubes under this condition (**Figure 5-6C**). These data show that the individual interactions in these auxiliary regions are weak, but multiple interactions allowed for avid binding to CA tubes. I confirmed that these sites also interact with CA hexamers at the R18 location, as the CA R18D mutation strongly reduced binding by all FEZ1 constructs (**Figure 5-6C**). A binding

mode of this nature is additionally supported by the salt-dependence of CA tube binding by FEZ1 constructs (**Figure 5-6E&F**). A longer construct with more capsid-interacting stretches, FEZ1₉₂₋₂₂₇, was able to retain binding in the presence of higher salt concentrations, as compared to a shorter construct with less binding stretches, FEZ1₉₂₋₁₅₈. These results support a model where primary hexamer-targeting motifs in FEZ1 (FEZ1₁₅₈₋₁₉₈) drives FEZ1-capsid interaction through avidity, with auxiliary binding provided by additional FEZ1 acidic stretches (**Figure 5-6D**).

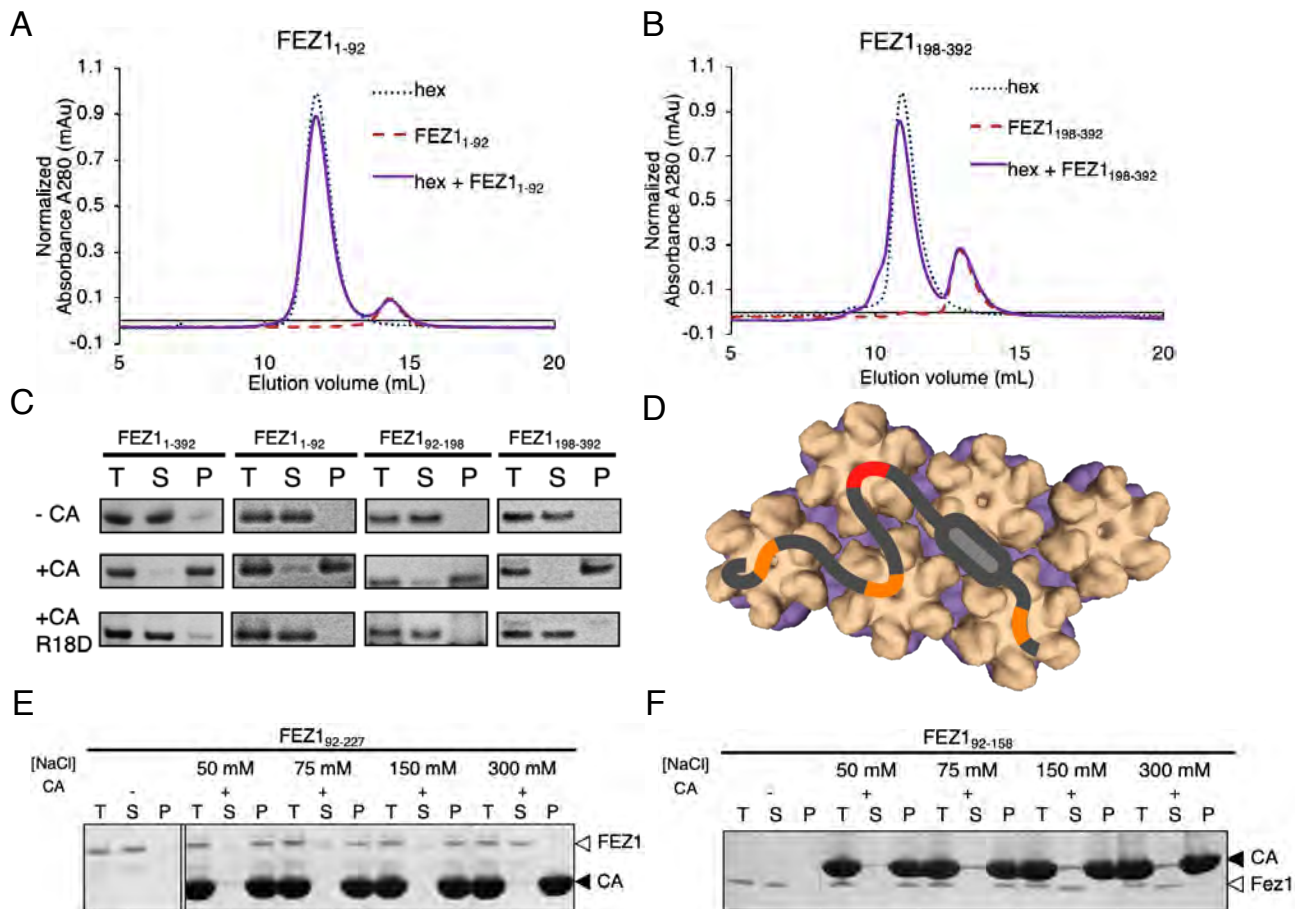


Figure 5-6 FEZ1 has multiple negatively charged regions for avid binding to the capsid

(A, B) SEC binding assay showing that FEZ1₁₋₉₂ (A) or FEZ1₁₉₈₋₃₉₂ (B) does not co-elute with CA hexamer. There is no elution shift of the mixture (solid purple) relative to the individual components (dotted lines). (C) Co-pelleting assays show that there are capsid-binding sites in both FEZ1₁₋₉₂ & FEZ1₁₉₈₋₃₉₂ that can

be detected in low salt (50mM NaCl); and the binding is abolished when using R18D CA tubes (bottom row). (D) Cartoon schematic showing the interaction of Fez1 with multiple hexamers. (E, F) The binding of FEZ1 constructs to CA tubes is reduced and abolished at different salt concentrations. FEZ1₉₂₋₂₂₇ interacts with CA tubes at physiological salt concentrations (150 mM) (E), while the FEZ1₉₂₋₁₅₈ only binds at lower salt concentrations (F), consistent with multiple binding sites in FEZ1.

5.3 Discussion

Despite low sequence homologies, the tertiary structure of capsid is highly similar among the retrovirus family [102-106]. Sequence alignment across the retrovirus genera show that this electropositive R18 pore is highly conserved, that R18G mutation of the capsid is non-viable for HIV-1 [107], and R18A/N21A capsid mutation leads to aberrant and much fewer cones leaving the HIV-1 virus with strikingly reduced infectivity [24, 108]. This ring of arginine R18 has also been indicated to form a pore for the recruitment of nucleotides and reverse transcription inside the capsid [94]. Indeed, I showed here that nucleotides are able to compete with FEZ1 for this binding site, as addition of dNTPs or TG50 oligonucleotides greatly reduced the binding of FEZ1 with capsid tubes, further confirming the importance of this capsid R18 residue binding with FEZ1 through charge-to-charge interaction. Moreover, the higher binding affinity of all four nucleotides dNTP with CA hexamer ($K_d = 6-40$ nM) than FEZ1 with CA hexamer ($K_d = 300$ nM) might be suggesting the co-regulation of the transportation of virus toward the nucleus, uncoating, and reverse transcription.

Interestingly, multiple different FEZ1 truncation constructs are able to bind with capsid tubes, meaning that throughout the entire FEZ1 there are multiple weaker secondary binding sites that adds up to strong interaction with the capsid. This is true since there are many negatively charged residues scattered throughout the entire FEZ1.

One possible model could be that the spacing of FEZ1 negatively-charged residues / polyglutamate regions as well as its flexible and elongated shape enables it to reach out and interact with multiple hexamers while the major binding site 178-188 is anchored to one capsid hexamer center. This provides optimal spacing and orientation for multiple weak domains to sample and engage productive interactions with the CA lattice, permitting higher avidity binding. Other HIV-1 restriction factors such as TRIM5 proteins [109] or MxA/MxB [110] also have similar binding mode, with multiple interaction domains that allow recognition of repeated structures of virus capsid. Charge-to-charge interaction could be formed faster and is more flexible, which is also seen in other capsid-host factor interactions such as MxB [82]. This charge-to-charge interaction is also shown to be important for protein stability, and that rational optimization of charge–charge interactions on the protein surface can be a viable strategy for enhancing protein stability [111]. Charged residues on capsid surface of Rous sarcoma virus is essential for functional virions and successful infection [112].

6 Mutations in FEZ1 negatively charged regions reduce HIV-1 early trafficking and infectivity

6.1 Introduction

My data above shows that FEZ1 makes specific contacts with the HIV-1 capsid through highly negatively charges, with the primary capsid-targeting regions in FEZ1₁₅₈₋₁₉₈, which contains a strong CA hexamer-interacting site in FEZ1₁₇₈₋₁₈₈. In order to test out the physiological relevance of these highly negatively charged residues and their

function in the process of HIV-1 trafficking and infection, we collaborated with the Naghavi Lab from Northwestern University.

6.2 Results and Discussion

To determine the importance of the FEZ1 charged regions during early HIV-1 infection in natural target cells, we first tested the effect of mutations in the hexamer-targeting region FEZ1₁₇₈₋₁₈₈. Human microglia CHME3 stably expressing control Flag alone, Flag-tagged wild-type (WT), or Flag-tagged FEZ1_{178-188E/A} (full-length FEZ1 that has all the glutamates in the region 178-188 mutated to alanine) were selectively depleted for endogenous FEZ1, followed by infection with HIV-1 pseudotyped with WT envelope and carrying a luciferase reporter gene [67]. Compared with CHME3 cells expressing exogenous WT FEZ1, HIV-1 infection was moderately impaired in cells expressing FEZ1_{1-392 178-188EA} (**Figure 6-1A**). Given the function of FEZ1 as a kinesin-1 adaptor protein that facilitates microtubule-based movement of incoming HIV-1 capsid cores [63, 67], we then tested whether these effects on early infection reflected defects in the transport of incoming viral particles to the nucleus. To do so, CHME3 cells depleted for endogenous FEZ1 and expressing exogenous forms of WT or mutant FEZ1, as described above, were infected with HIV-1 pseudotyped with WT envelope and whose core was labeled using GFP-tagged Vpr. These cells were then imaged by live cell microscopy. Rapid, long-range bi-directional movement of HIV-1 particles was observed in cells expressing exogenous WT FEZ1, and the motility of HIV-1 particles was not significantly affected in CHME3 cells expressing FEZ1_{1-392 178-188EA} (**Figure 6-1C**). It is somewhat surprising that

mutation of this major CA hexamer-targeting region of FEZ1 did not show a detectable trafficking defect. This is possibly due to that the many secondary binding sites in FEZ1_{1-392 178-188EA} collectively still allow for an avid binding of HIV-1 capsid, and the reduction (not major loss) in binding was below the threshold of detection in our trafficking measurements.

We then looked into the capsid-targeting regions in FEZ1₁₅₈₋₁₈₈, which allows for avid capsid binding through many negatively charged residues dispersed in multiple patches. We constructed the Flag-tagged FEZ1_{158-198E/A}, which is full-length FEZ1 that has all the glutamates in the region 158-198 mutated to alanine. We tested the effect of FEZ1_{158-198E/A} expression on the early infection and transport of incoming HIV-1 particles in cells depleted for endogenous FEZ1. HIV-1 infection was significantly reduced in CHME3 cells expressing the FEZ1_{158-198E/A} (**Figure 6-1B**). Moreover, FEZ1_{158-198E/A} expression in CHME3 cells failed to rescue HIV-1 transport to the nucleus, indicating that the motility of incoming HIV-1 particles was significantly reduced (**Figure 6-1D**). Note that imaging was conducted after spinoculation-based infection and after time taken to set acquisition locations, the times shown in the figure indicate the period of imaging beginning at 20 min post-infection. For this reason, in control and FEZ1, but not FEZ1_{1-392 158-198EA} cells, a significant number of particles are already trafficking in the cytosol and approaching the nucleus. Moreover, as infection progresses the number of particles in control and FEZ1 cells decreases due to movement out of the focal plane and/or uncoating.

To further confirm that the defect in early transport reflected impairment in microtubule motor activity, cells were treated and infected as above but imaged at a higher frame rate of 1 frame per second (fps) over a 300s period followed by measurements of distances traveled by viral particles in either retrograde or anterograde directions [63]. In the control siRNA-treated cells and WT FEZ1 expressing cells particles on average traveled longer retrograde than anterograde distances, resulting in a net forward movement toward the nucleus (**Figure 6-1E**). In contrast, in FEZ1^{1-392 158-198EA} expressing cells viral particles did not exhibit any difference in retrograde versus anterograde movement, resulting in no net forward movement toward the nucleus and in line with findings that overall transport and early infection are impaired in the presence of this mutant. These results support the notion that multiple negative charged regions of FEZ1 contribute to early HIV-1 infection through avid interactions with the viral capsid, and that the negative charges within the 158-198 motif are specifically required for FEZ1 to control HIV-1 transport to the nucleus.

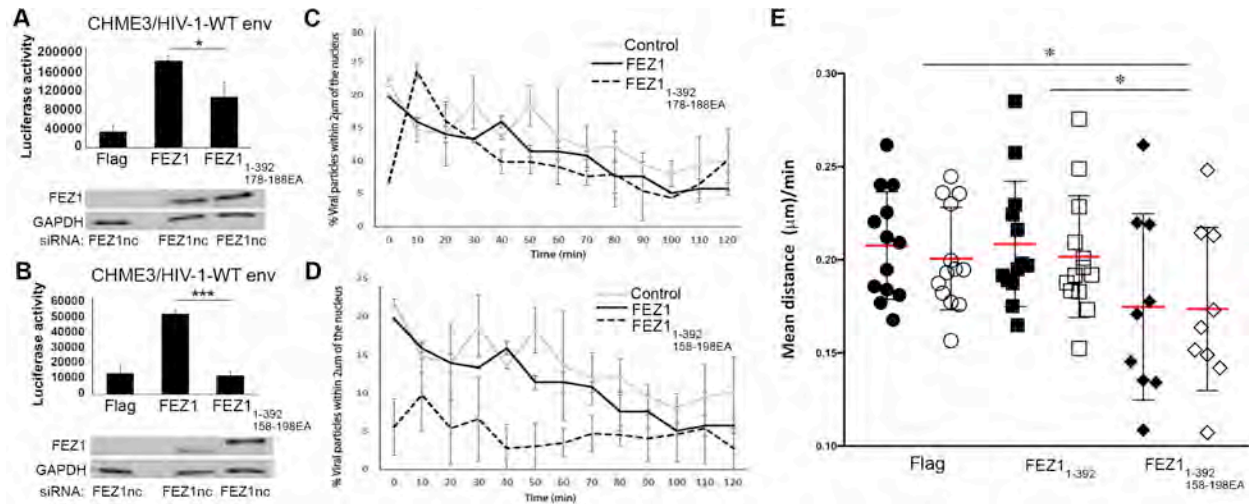


Figure 6-1 FEZ1 Capsid-Binding Regions Contribute to Early HIV-1 Infection

(A–D) CHME3 cells stably expressing control FLAG (control), WT (FEZ1), or mutant FEZ1 (FEZ1_{1–392 178–188EA} or FEZ1_{1–392 158–198EA}, alanine substitution mutants of glutamates in the region 178–188 or 158–198 of full-length FEZ1, respectively) were treated with an siRNA targeting the FEZ1 30 UTR (FEZ1nc) to deplete endogenous FEZ1. Cells were then infected with HIV-1 luciferase reporter virus carrying the WT envelope (HIV-1-WT-Luc) followed by measurement of luciferase activity (A and B). The error bars represent SD from at least three independent experiments. Knockdown levels of endogenous FEZ1 in each sample from (A) and (B) are shown in the lower panels, which were analyzed by western blotting using anti-FEZ1 antibodies. GAPDH served as loading control. (C, D) CHME3 cells depleted for endogenous FEZ1 and expressing control FLAG or exogenous forms of WT or mutant FEZ1 as in (A) and (B), respectively, were infected with HIV-1-WT-Luc containing GFP-Vpr (HIV-1-WT-Luc- GFP-Vpr) and imaged live at 3 frames per min for 2 h, followed by quantification of the percentage of viral particles within 2 µm of the nucleus at the indicated times after infection. The error bars represent SD from at least three independent experiments. (E) Quantification of the average distance (micrometers per 2.5 min) traveled by viral particles toward the nucleus (retrograde motility shown as black symbols) or away from the nucleus (anterograde motility, shown as white symbols) in CHME3 cells as in (D).

7 Model simulation further confirms the charge-charge interaction of FEZ1 with capsid residue R18

7.1 Introduction

Model simulation has been shown to be a valuable tool in understanding HIV-1 virus capsid properties [9, 113, 114], and are able to reveal important details of the capsid which points to its biological functions. To investigate the interaction of FEZ1 with the CA

hexamer, we collaborated with graduate student Chaoyi Xu and Dr. Juan Perilla from the University of Delaware to build an all-atom model and setup a canonical 2 μ s molecular dynamics simulation.

7.2 Results and Discussion

To prevent model bias by the initial simulation setup, the FEZ1₁₇₈₋₁₈₈ peptide was initially placed outside of the CA hexameric pore more than 24 Å from R18 (**Figure 7-1A**). The dynamic β -hairpin structure [94] and the flexibility of the FEZ1 peptide allow FEZ1 to reach down into the center of the R18 ring. During the simulation, the FEZ1₁₇₈₋₁₈₈ segment rapidly translocated into the pore at the beginning of the simulation and stably remained inside the hexamer pore. Importantly, the stability of binding was conferred by interactions between FEZ1 and the R18 residue for the remaining of the simulation (**Figure 7-1B & Movie 1**). This rapid conformational change, followed by a stable conformation, demonstrates strong interactions between FEZ1₁₇₈₋₁₈₈ and the CA hexamer. In addition, the fact that the FEZ1₁₇₈₋₁₈₈ was recruited from the exterior of the capsid towards the interior cavity, shows weak electrostatic shielding provided by solvent, water, and ions.

To identify the detailed molecular contacts between FEZ1 and the CA hexamer, we performed statistical analysis on the contacts observed during the simulation. The contact analysis reveals that FEZ1 binds to the CA-hexamer driven by the electrostatic interactions between the poly-glutamate stretch in FEZ1₁₇₈₋₁₈₈ and the R18 in CA-hexamers (**Figure 7-1C&D**). Moreover, the stability of these salt-bridges was also demonstrated by the high contact occupancies exhibited during the simulation.

Specifically, the salt-bridges between E182-R18 and E183-R18 contacts, both showed high occupancy larger than 99.5%. Results from our MD simulations suggest that FEZ1₁₇₈₋₁₈₈ negatively charged residues strongly bind to the positively charged residue R18 inside of the CA hexamer center pore through salt-bridges. An important detail revealed by the simulations is the ability of FEZ1 to rapidly access the CA-hexamer cavity and stably bind to it.

The simulation also provides insight into the structure of the FEZ1₁₇₈₋₁₈₈ upon binding to capsid and the influence on the ionic environment. FEZ1 in general is predicted to be disordered by itself [68]. Our results show that while the bound FEZ1₁₇₈₋₁₈₈ still contains large disordered areas, the region near FEZ1₁₈₂₋₁₈₄ becomes ordered with a stable conformation during the simulation (**Figure 7-1E**). The simulation also shows that binding of FEZ1 at the hexamer interface stabilizes FEZ1 from unstructured form into a turn conformation. (**Figure 7-1F**). Together, our MD results also support that FEZ1 negatively charged residues strongly bind positive residue R18 inside of the CA hexamer through forming electrostatic interactions.

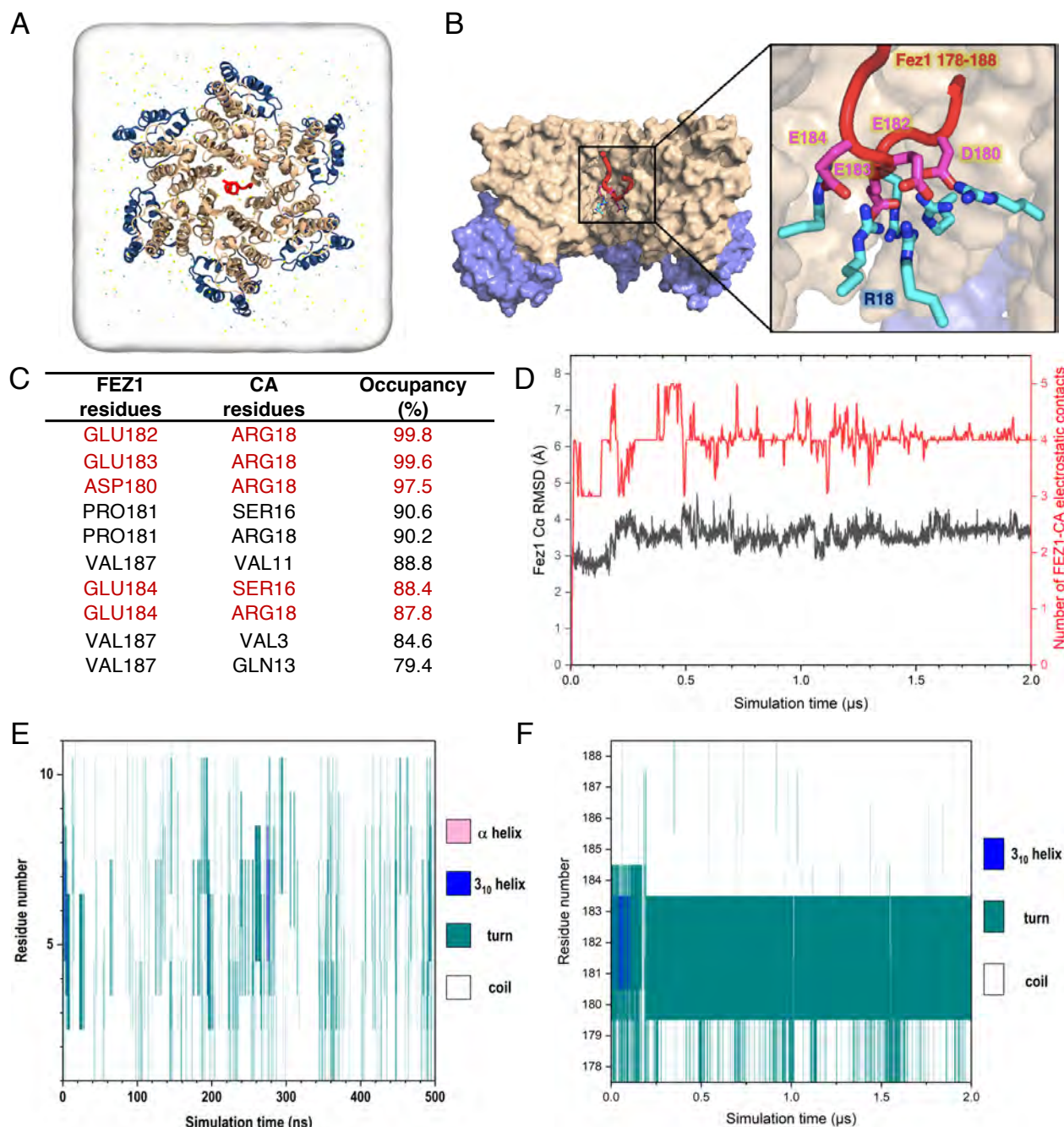


Figure 7-1 All-atom molecular dynamic simulations identify FEZ1 interactions at the CA hexamer center.

(A) The all-atom model of FEZ1₁₇₈₋₁₈₈ is placed at the center of the simulation box containing a CA hexamer, water and 150 mM NaCl. Before the simulation, the initial location of the FEZ1₁₇₈₋₁₈₈ segment is 24 Å away from R18. CA_{NTD} (gold), CA_{CTD} (blue) and FEZ1₁₇₈₋₁₈₈ (red) are shown in a ribbon representation. (B) Binding of FEZ1 to the CA hexamer after 2 μs of MD simulation. Surface representation of the internal hexamer center pore showing that the FEZ1 interacts with the R18 residues of the CA hexamer (cyan/blue sticks) through negatively charged acidic residues (magenta/red sticks). (C) A list of the top 10 residues in the CA hexamer that are interacting with FEZ1₁₇₈₋₁₈₈, showing that FEZ1₁₇₈₋₁₈₈ is stably bound to R18 of the CA hexamer. The occupancy is calculated throughout the length of the simulation. (D) Dynamics of FEZ1₁₇₈₋₁₈₈ near a CA hexamer. FEZ1 quickly travels from the exterior of the hexamer to the interior (500 ns). After 500 ns, the interaction between FEZ1 and CA plateaus. The

root-mean-square deviation (RMSD) plot of the FEZ1₁₇₈₋₁₈₈ C α atoms (in gray) and the electrostatic interactions with the CA hexamer (in red) during the simulation are shown.

8 Structural determination of FEZ1-capsid hexamer complex

8.1 Introduction

From the biochemistry experiments, I discovered that FEZ1 interacts with the HIV-1 capsid hexamer through charge-charge interactions. To elucidate the detailed molecular interaction of FEZ1 with HIV-1 capsid hexamer, I tried several structural methods to obtain atomic-resolution structure of the complex. I made different FEZ1 constructs and fusion proteins, and utilized both X-ray crystallography and electron microscopy to study the structure of the complex.

I first tried co-crystallization of different FEZ1 proteins and peptides with capsid hexamer, and also tried peptide soaking. I was able to get good crystals that diffracted well, but I was unable to see FEZ1 in the electron density, possibly due to it being averaged out due to the symmetry of capsid hexamer. Next, I tried a variety of fusion proteins by fusing FEZ1 directly to other capsid binding proteins, including GST, CypA, SpyCatcher/SpyTag system, and the llama nanobody. These will be talked about more in the results section. The idea of making fusion proteins is in the hope that they will: (1) increase the local concentration of FEZ1 and thus enhance the binding affinity for FEZ1 to capsid, which would be especially useful for electron microscopy; (2) break the symmetry of FEZ1 binding with capsid hexamer, because FEZ1 is often averaged out due to the six-fold symmetry of capsid. The schematics of the methods used are summarized in **Figure 8-1**.

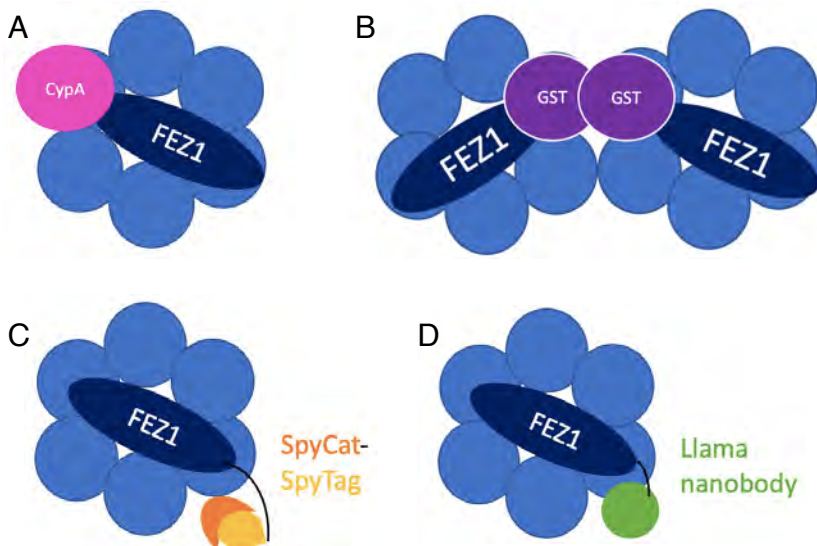


Figure 8-1 Cartoon figures of the FEZ1 fusion proteins

(A) CypA-FEZ1 fusion protein. CypA binds to the flexible loop on the NTD of CA protein. (B) GST-FEZ1 fusion protein. Globular GST provides a marker for visualization under microscopy, and the dimerization property can potentially align FEZ1 as a certain direction onto di-/hexamers. (C) SpyTag-FEZ1 fusion protein. SpyTag interacts with the SpyCatcher tag on CA protein, thus enhancing the local concentration of FEZ1 and also the interactions between FEZ1 and CA hexamer. (D) Llama-FEZ1 fusion protein. Llama nanobody binds strongly to the CTD of CA protein, thus could provide a strong zipping interaction between FEZ1 and CA hexamer.

8.2 Results

8.2.1 Co-crystallization of FEZ1 constructs and peptide with HIV-1 capsid

To get a structure of the FEZ1-capsid complex, I started with the expertise of our lab, X-ray crystallography. I pinpointed the binding site of FEZ1 to capsid hexamer, and utilized different FEZ1 constructs containing this binding site to set up crystal trays with the microbatch under oil method. The constructs of FEZ1 tested are listed in **Table 2**, with the crystallization conditions described. I also tried co-crystallization of capsid hexamer with a FEZ1 peptide with residues 178-188 (the major binding site), and this peptide has a tryptophan addition to facilitate its purification. In addition to capsid hexamers, I also tried crystallization with half-hexamers that are able to form back into hexamers.

I got several crystals that were able to diffract well (**Figure 8-2A**), and the representative data collected for these crystals are summarized in **Table 3**. However, upon examination of the electron density after solving the structure, I noticed that the center of the hexamer where I expected FEZ1 to bind had a six-fold axis of symmetry (**Figure 8-2B**). I was unable to see the FEZ1 peptide bound, likely because it was either not present in the crystal or averaged out due to the effects of the symmetry of the crystal at this binding site. I repeated my crystallization screening in different conditions, and also optimized them further, with the hope that I would find a crystal in a different space group without the six-fold symmetry, or that at high concentrations, the FEZ1 peptide may break the symmetry of the crystals. However, I was unsuccessful and attempted to make FEZ1-fusion proteins.

| Protein | Conditions | Oil P:S* | Conc. | Temp | Crystals & optimization |
|---|---|----------|-----------------------------------|-----------|---|
| FEZ1₁₅₈₋₁₉₈ + hexamer | Classics, Pact, ProComp, JCSG, Morpheus, PEGII | 2:1 | 1 mg/mL | RT | PACT: 29, 39, 41, 42 ProComp: 46 |
| FEZ1₁₅₈₋₁₉₈ peptide + hexamer | Classics, Pact, ProComp, JCSG, Morpheus, PEGII | 2:1 | Hex: 1 mg/mL Peptide: 1 mM | RT | √ |
| FEZ1₁₅₈₋₁₉₈ peptide + half-hex¹ | Classics, Pact, ProComp, JCSG, Morpheus, PGA | 2:1 | Hex: 0.5 mg/mL Peptide: 0.5 mM | RT | √ ¹ these are the half-hexamers that can form the hexamer back |
| FEZ1₁₅₈₋₁₉₈ peptide + half-hex² | Classics, Pact, ProComp, JCSG, Morpheus, PGA | 2:1 | Hex: 0.5 mg/mL Peptide: 0.5 mM | RT | X ² these are the hexamers that cannot form the hexamer back |
| FEZ1₁₅₈₋₁₉₈ peptide + half-hex³ | Classics, Pact, ProComp, JCSG, Morpheus, PGA | 2:1 | Hex: 0.5 mg/mL Peptide: 0.5 mM | RT & 12°C | X ³ these are the hexamers that can form the hexamer back, but have their CTD deleted |
| FEZ1 177-191 + hex/half-hex¹ 178- SPDP EEEEE VLEEE W -191 | Classics, Pact, ProComp, JCSG, Morpheus, PGA | 2:1 | Hex: 0.5 mg/mL Peptide: 0.5 mM | RT | √ ¹ these are the half-hexamers that can form the hexamer back |
| Hexamer R18D | Classics, Pact, ProComp, JCSG, Morpheus, PGA | 2:1 | 1 mg/mL | RT | √ |
| CypA-FEZ1 158-198 + hexamer/hexamer-221 | Classics LITE, Pact, ProComp, JCSG, Morpheus, PEGII | 2:1 | complex: 1 mg/mL | RT / 12°C | rectangular cuboid, thin half-/hexamer, small needle-like crystals |
| CypA-FEZ1 158-198 + hexamer + llama nanobody | Classics, Pact, ProComp, JCSG, Morpheus, PEGII MCSGI, MCSGII | 2:1 | complex: ~3 mg/mL | RT | rectangular cuboid, long rod-like crystals, thin half-/hexamer, small needle-like crystals |
| SpyCat-hex + SpyTag-FEZ1 | Classics, Pact, ProComp, JCSG, Morpheus, PEGII, MCSGI | 2:1 | 1 mg/mL | RT | thin half-/hexamers, small needle-like crystals |

Table 2 Crystallographic conditions of FEZ1 proteins, FEZ1 peptide, and FEZ1 fusion proteins

*P, Paraffin oil; S, Silicon oil

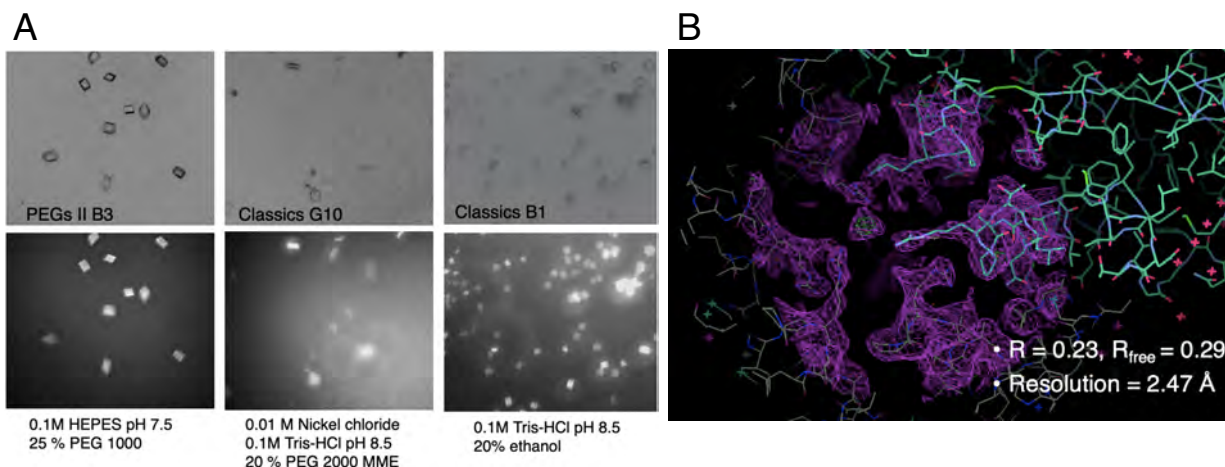


Figure 8-2 Co-crystallization of FEZ1 constructs and peptide with HIV-1 capsid

(A) Crystals obtained and the condition. Top row is the crystals under visible light, while the bottom row is under UV light. (B) Electron density map of the structure of FEZ1 peptide with CA hexamer. FEZ1 is proposed to be interacting at the center of the CA hexamer, however, due to averaging, no density is observed.

| Data collection (Overall) | hexamer with FEZ1 peptide | half-hexamer with FEZ1 peptide | hexamer with FEZ1 peptide |
|---------------------------|---|--|---|
| Spacegroup | P 21 21 21 | H3 | P6 |
| Unit Cell | 133.00 133.08 203.85 90.00 90.00 90.00 | 89.73 89.73 164.41 90.00 90.00 120.00 | 90.63 90.63 56.69 90.00 90.00 120.00 |
| High resolution limit | 4.42 | 2.39 | 1.87 |
| Low resolution limit | 133.08 | 70.25 | 78.49 |
| Completeness | 99.7 | 98.8 | 98.6 |
| Multiplicity | 8.1 | 6.3 | 6.2 |
| I/sigma | 3.5 | 14.9 | 15.0 |
| CC(1/2) | 0.990 | 0.998 | 0.997 |
| Rmerge | 0.250 | 0.069 | 0.075 |
| Rmerge (anomalous) | 0.240 | 0.062 | 0.067 |
| Rmeas | 0.268 | 0.075 | 0.082 |
| Rmeas (anomalous) | 0.271 | 0.074 | 0.080 |
| Rpim | 0.093 | 0.029 | 0.032 |
| Rpim (anomalous) | 0.124 | 0.040 | 0.042 |
| Anomalous completeness | 98.5 | 93.8 | 88.2 |
| Anomalous multiplicity | 4.3 | 3.0 | 2.9 |
| Anomalous correlation | -0.199 | -0.060 | 0.118 |
| Anomalous slope | 0.483 | 0.938 | 1.072 |
| Total observations | 188206 | 121217 | 134065 |
| Total unique | 23245 | 19349 | 21708 |

Table 3 Data collection of FEZ1 peptide with hexamers or half-hexamers

8.2.2 Using GST-FEZ1 to obtain FEZ1-capsid complex structure by electron microscopy

To visualize FEZ1 by electron microscopy, I utilized GST as a marker. GST protein is a 27 kDa globular protein, and can be visualized as a round sphere by microscopy. Moreover, GST protein can also act as a dimerization factor, since FEZ1 has been previously described as a dimer [68]. This will anchor GST-FEZ1₁₅₈₋₁₉₈ to a hexamer dimer, which could possibly orient the FEZ1 and also allow for the visualization of the FEZ1-hexamer complex. However, even though I can see from the gel filtration that GST-FEZ1 binds nicely to hexamers and di-hexamers (**Figure 8-3A&B**), it is hard to resolve in the EM images of the negative-staining samples (**Figure 8-3C**). In the 2D class average of these EM images (**Figure 8-3D**), I observed that there are GST proteins in the middle of two hexamers, but it is hard to see the binding of FEZ1 in the center of hexamers.

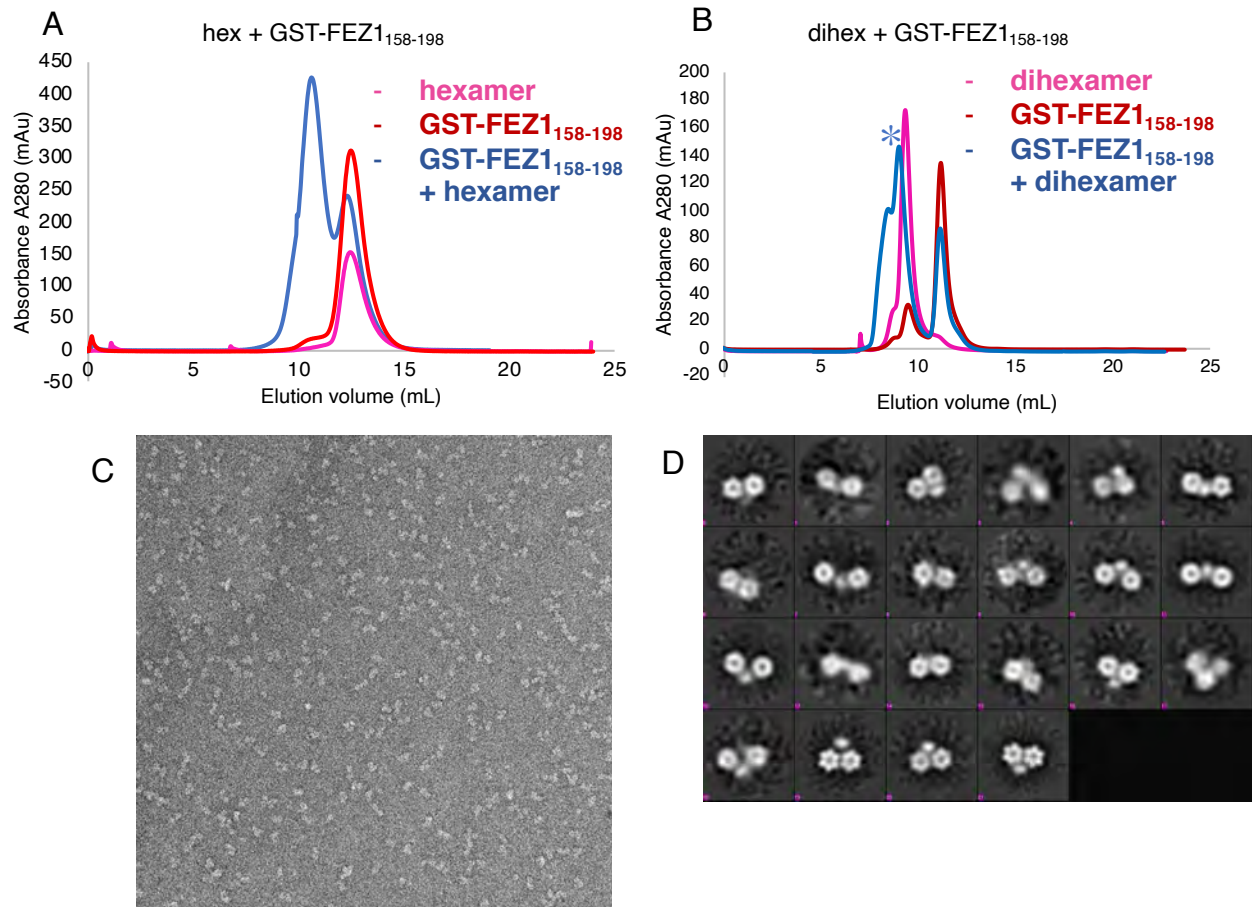


Figure 8-3 Using GST-FEZ1 to obtain FEZ1-capsid complex structure

(A) Size exclusion chromatography binding of hexamer with GST-FEZ1. (B) Size exclusion chromatography binding of dihexamer with GST-FEZ1. I took the peak of the mixture for negative-staining EM (indicated by asterisk). (C) Negative-staining EM image of the mixture complex from (B). (D) 2D class average of the GST-FEZ1 dihexamer complex.

8.2.3 CypA-FEZ1 fusion protein as a helical symmetry approach to capture the FEZ1-capsid complex

Cyclophilin A, known as CypA, a host factor that interacts with capsid, participating in virus infection and uncoating [99, 115, 116] [117-119]. From the structure of CypA with CA-NTD (PDB: 1AK4) [99], I can see that it is interacting with the flexible CypA loop of the CA. Because it is binding at a non-overlapping site in the CA, it would be a great tool

for the anchoring of FEZ1 onto the CA hexamer. Moreover, it could serve as a marker for breaking the symmetry of the hexameric capsid.

SEC shows that the CypA-FEZ1 binds with the capsid hexamer, as the elution peak is shifted to a larger size (**Figure 8-4A**). In pelleting assays, 80% of CypA binds to capsid tubes, and the interaction is not sensitive to salt concentration (**Figure 8-4B**). The binding of FEZ1₁₅₈₋₁₉₈ is sensitive to salt, increasing the salt concentration decreases the interaction of FEZ1 to capsid tubes. However, the fusion protein CypA-FEZ1₁₅₈₋₁₉₈ greatly enhanced the interaction of FEZ1 with the capsid tubes. To obtain the structure of the complex, I first tried X-ray crystallography of CypA-FEZ1 with both the hexamer and also the hexamer-221 (only has the NTD) (summarized in **Table 2**). I did see some crystals, and some of them were needle-like or star-like shaped, while some half the hexamers or half-hexamer shapes, but are very thin plates. I also saw some rectangular crystals (**Figure 8-4C**). However, optimization of the crystallization conditions did not improve and I did not get bigger-size crystals. As another attempt, I added in llama nanobody to the CypA-FEZ1 + capsid hexamer crystallization condition to see if it can help the breakage of the normal symmetry of hexamers. I did obtain several crystals, but the diffraction of these crystals did not yield good resolution.

On the other hand, I tried negative-staining EM technique with CypA-FEZ1 + capsid hexamer complex (**Figure 8-4D**). From the 2D class average images, I were able to see some masses that possibly indicated the position of CypA, but still could not get good images that confirm the binding of CypA-FEZ1 with capsid hexamer.

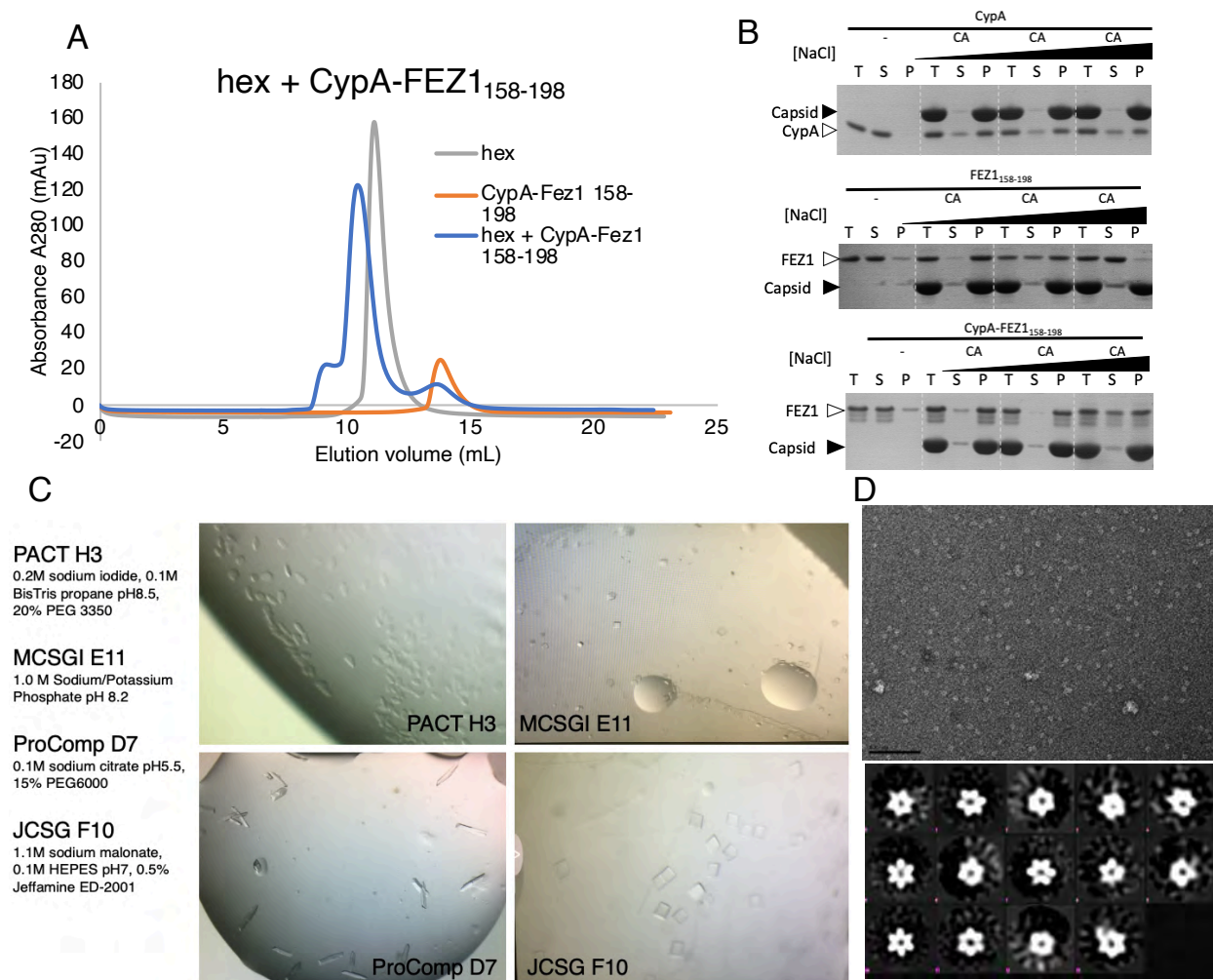


Figure 8-4 CypA-FEZ1 fusion protein as a helical symmetry approach to capture the FEZ1-capsid complex

(A) Size exclusion chromatography binding of hexamer with CypA-FEZ1. (B) Pelleting assay of CypA, FEZ1, and CypA-FEZ1 with CA tubes. CypA-FEZ1 enhanced the binding with CA tubes. (C) Crystals and the conditions of CypA-FEZ1 + hexamer. (D) EM image of negative-staining of the mixture complex from (A), and the 2D class average of the CypA-FEZ1 hexamer complex.

8.2.4 Utilizing the SpyTag/SpyCatcher system for the study of FEZ1-capsid complex

In order to align FEZ1 onto the hexamer and form a stable complex, I also utilized the SpyCatcher-SpyTag system. The idea is that only one of the six CA from the hexamer is tagged with SpyCatcher, which can interact with the SpyTag-FEZ1. This provides high local concentration as well as facilitates the orientation of a single FEZ1 on hexamer.

SpyCatcher (138 residues, 15kDa protein) and SpyTag (13-amino acid peptide) are derived from the *Streptococcus pyogenese* fibronectin-binding protein FbaB. They are able to rapidly and stably form covalent isopeptide bond upon mixture [120].

The mixture of SpyCatcher-hexamer (SpyCat-hex) with SpyTag-FEZ1 (FEZ1₁₇₈₋₁₈₈) yielded good binding and hence a sharp peak in gel filtration (**Figure 8-5A**). There are excess of SpyCat-hex in the peak, as indicated by the band on SDS-PAGE gel. To ensure that every SpyCat-hex is bound with SpyTag-FEZ1, I pooled the peak fractions and incubated with more SpyTag-FEZ1, and then ran the second gel filtration. This time all of the SpyCat-hex formed a complex with SpyTag-FEZ1, as the SpyCat-hex alone band disappeared (**Figure 8-5B**). Interestingly, a bigger molecular weight complex peak around 10.5 mL showed up, and there is a protein band around 75 kDa in SDS-PAGE, which could possibly be two SpyCat-hex (35.9 kDa) interacting with one SpyTag-FEZ1 (8 kDa). I took the peak fractions of the first and second peaks of the second SEC run and looked under negative-staining EM (**Figure 8-5C**). Image from the first peak showed larger complexes, while image from the second peak showed mostly single capsid hexamer, with occasionally two or three hexamers side-by-side. It is hard to tell that the SpyTag-FEZ1 is interacting with the SpyCat-hex. On the other hand, I also tried crystallization with this complex, and I got mostly small needle-shaped crystals. I tried to optimize these crystal conditions, but I was not able to get larger and better crystals (**Figure 8-5D**).

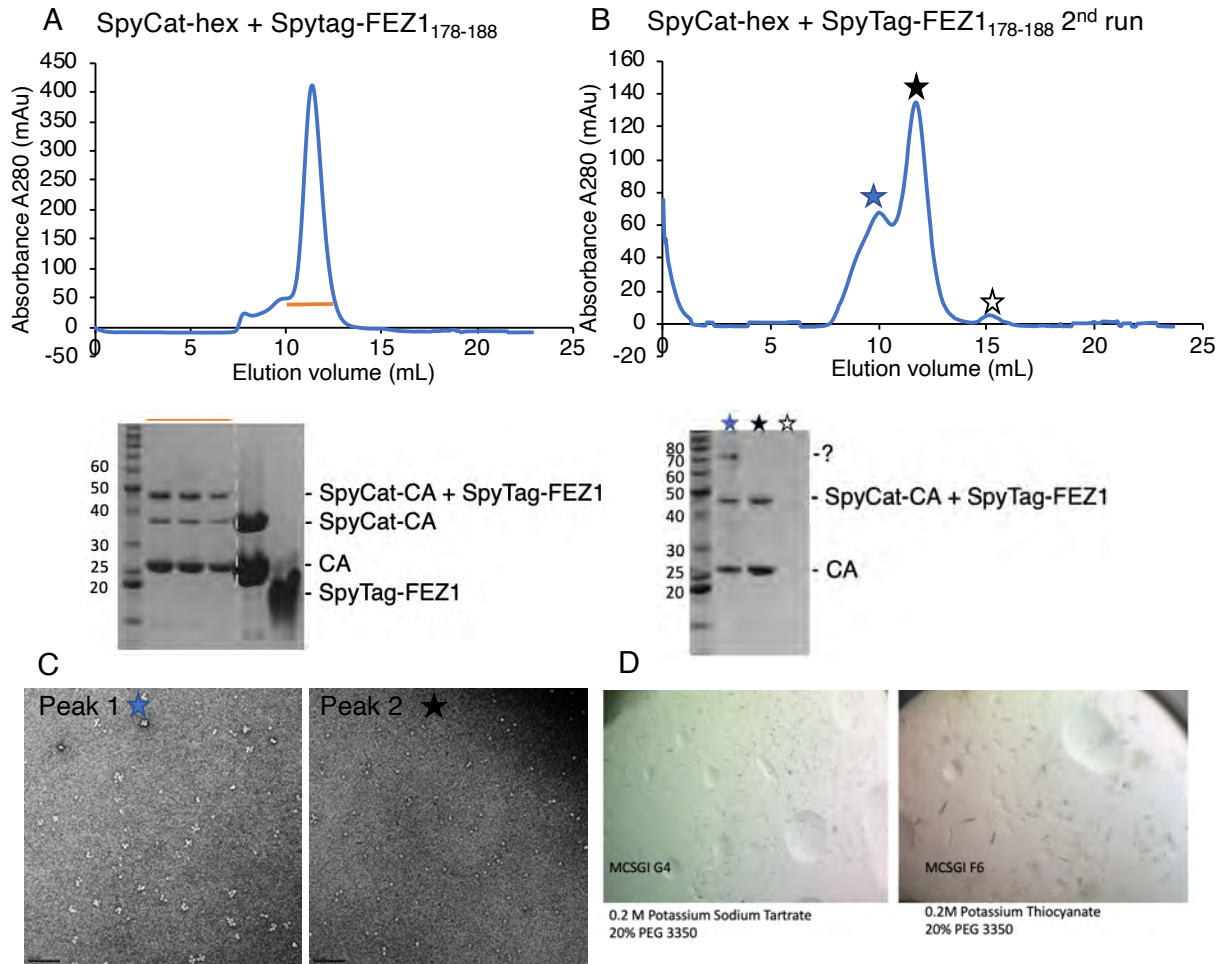


Figure 8-5 Utilizing the SpyTag/SpyCatcher system for the study of FEZ1-capsid complex
 (A, B) Size exclusion chromatography binding of SpyCat-hex with SpyTag-FEZ1. There is still excess of SpyCat-hex in the first run of SEC, therefore, incubated with more SpyTag-FEZ1 and ran the second SEC. the first and second peak (blue and black star, respectively) is taken for negative-staining EM. (C) Negative-staining EM image of the mixture complex from (B). (D) Crystals and the conditions of SpyCat-hex with SpyTag-FEZ1.

8.2.5 Using llama nanobody-FEZ1 to probe the structure of FEZ1-capsid complex

In order to form a tighter complex to enable the EM study of the FEZ1-capsid hexamer complex, I constructed the fusion protein of llama nanobody with FEZ1. A llama nanobody that has high affinity ($K_d = 0.69$ nM) to the CTD of capsid hexamer was discovered recently [121]. Based on the published nanobody-CA CTD structure,

nanobody would not interfere with the binding with FEZ1, and would provide a tighter binding for anchoring the FEZ1 onto the capsid hexamer.

I constructed the llama nanobody-FEZ1 fusion protein (will be referred to as llama-FEZ1 afterwards), and purified it to great purity. The behavior of llama-FEZ1 is very good, and I obtained large amount of pure proteins. For the SEC binding of llama-FEZ1 with capsid hexamers, I started with a concentration ratio of 1 hex: 1 llama-FEZ1, and found that there is an excess of capsid hexamers (**Figure 8-6A**). Under negative-staining EM, I can see that there are some protein densities sticking out of the hexamer, indicating the presence of llama-FEZ1 (**Figure 8-6B**). I tried several different concentration ratios of hex to llama-FEZ1. When increasing the ratio of hex: llama-FEZ1 to 1:7, since there is excess of FEZ1, each hexamer is theoretically bound with six llama-FEZ1 (**Figure 8-6C**). Under EM images of negative-staining samples, I can see that there are two or three hexamers side-by-side, which could possibly be indicating that llama and FEZ1 on the same fusion protein are binding to different hexamers (**Figure 8-6D**). To get llama-FEZ1s binding to a single hexamer, I added excess amount of llama-FEZ1 at a ratio of hex: llama-FEZ1 = 1:12 (**Figure 8-6E**). As shown by the cryo-EM image, some of the particles are a single hexamer (pink circle, **Figure 8-6F**). However, the particles seem not homogeneous enough for structure determination.

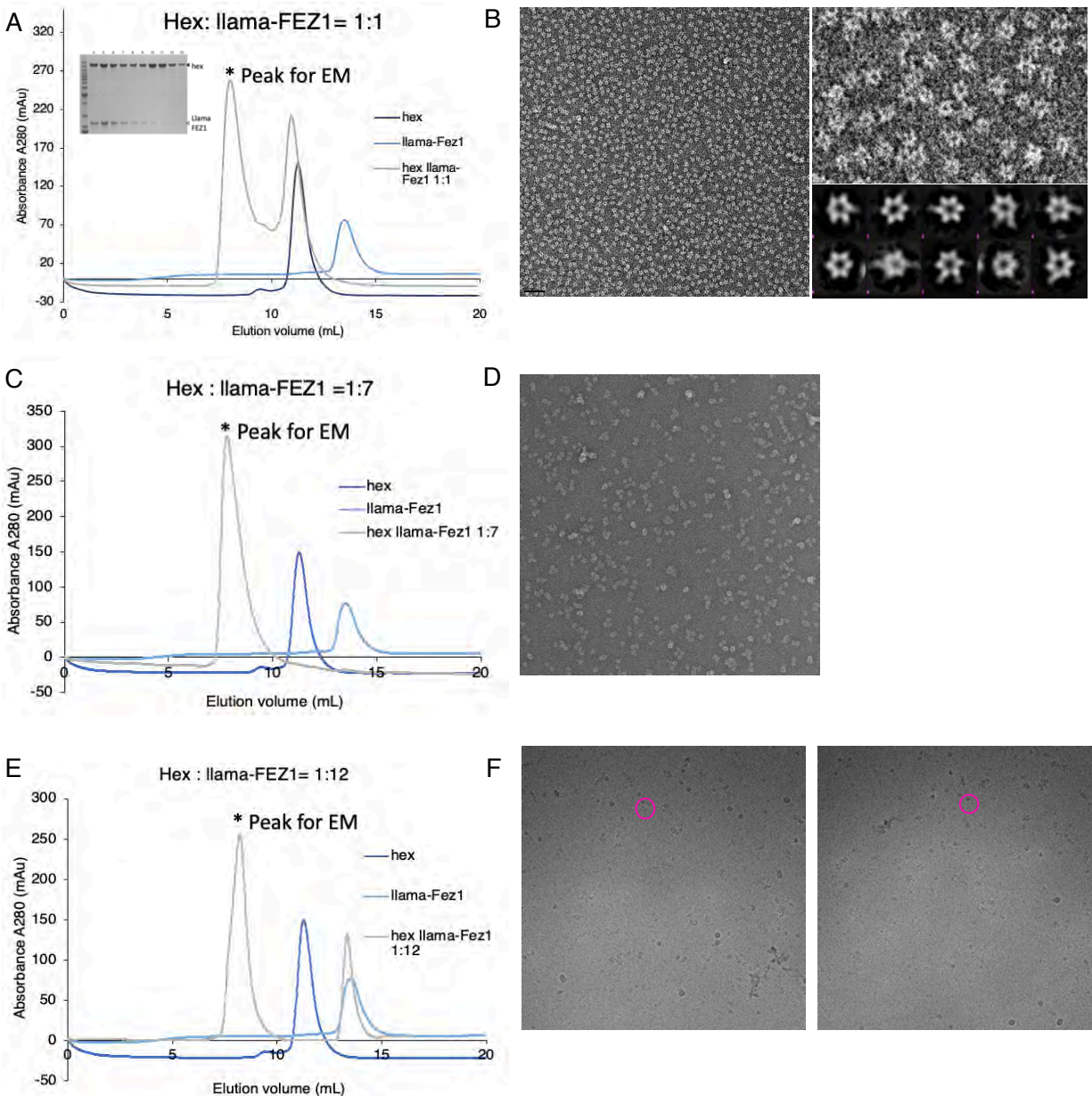


Figure 8-6 Using llama-FEZ1 to probe the structure of FEZ1-capsid complex

(A, C, E) Size exclusion chromatography of different concentration ratio of hexamer to llama-FEZ1. The peaks that are taken for negative-staining EM are indicated by an asterisk. (B, D, F) Negative-staining EM images of the mixture complex from (A, C, E), respectively. Pink circles in (F) indicates the presence of a single hexamer.

8.3 Discussion

Previously, structures of CA bound to host cofactors CPSF6 and Nup153 have been solved [85, 86]. Both host cofactors are binding at a preformed pocket in the NTD–

CTD interface, with the stoichiometry of one cofactor to one CA monomer (six cofactors per CA hexamer). Thus, the six-fold symmetry (P6) of the capsid hexamer is an advantage in solving these cofactor-capsid complexes. On the contrary, FEZ1 protein is binding at the center of the capsid hexamer as one FEZ1 per CA hexamer, thus it is challenging for structure determination. I discovered that FEZ1 is averaged out in co-crystal structures with CA hexamers. Moreover, since FEZ1 has many unstructured regions, this makes the structure solving with larger FEZ1 constructs challenging. As FEZ1 has multiple glutamate residues and there are six arginines in the center of the capsid hexamer, these glutamates and arginines may be interacting differently, adding to the already challenging structure solving process.

Despite substantial effort in both crystallization and electron microscopy studies, an atomic-resolution understanding of the FEZ1-CA interaction remains elusive. I have made extensive attempts of improving the binding affinity as well as trying to break the symmetry, but I was not able to achieve a structure of the FEZ1-CA complex. The inherent challenges of solving complex structures of factors that bind at the symmetrical capsid interfaces is not unique to FEZ1, as there are other factors such as MxB that also binds at the symmetrical tri-hexamer interface.

There are several other methods that could be promising, one of them being cryo-electron tomography. It has been used to yield TRIM proteins on CA cores, although it is still at low resolution [122]. Another method is to decorate the entire capsid tube with proteins and solve the protein-capsid structure utilizing helical reconstruction. This approach has been published in the structural study of capsid tube assemblies [123, 124].

Also, as the computational power of single-particle cryo-EM has greatly improved, it might provide another promising path toward solving the structure of FEZ1-CA.

9 Conclusions and Future Directions

The work presented herein demonstrates that FEZ1 is a unique HIV-1 capsid pattern sensor, which uses highly negatively charged acidic stretches to interact with the positively charged center pore of the CA hexamer. Although the interaction is driven by electrostatic contacts with multiple charged stretches on FEZ1, the recognition of CA hexamers appears to be highly specific, as there is no binding detected with CA pentamers that contain similar charge characters (**Figure 3-1G**). Consistent with FEZ1's role in early viral transport, I found that FEZ1 mutations that abolish its interaction with CA tubes greatly reduced both the accumulation of virus particles around the nucleus and HIV-1 infectivity. These results establish a solid link between FEZ1 and intracellular trafficking of HIV-1, substantiating its roles as an adaptor bridging viral capsid and kinesin-1 (**Figure 9-1A**).

The interaction between FEZ1 and HIV-1 capsid follows a common theme found in the cases of many other capsid-interacting proteins, where the simultaneous binding at multiple otherwise weak individual contact sites creates an avidity effect for a stable interaction [109, 122, 125-127]. Although FEZ1 contains a reasonably high-affinity CA hexamer-interacting site (FEZ1₁₇₈₋₁₈₈), the electrostatic nature of the interaction does not sustain the ionic strength conditions and the direct competition from high concentrations of dNTPs/NTPs and IP6 molecules in cells. HIV-1 solves this problem by using the

repeating nature of the capsid lattice to interact simultaneously with numerous negative patches within FEZ1. This highlights the advantageous capsid-targeting mode employed by many cellular protein factors, only relatively weak individual interaction sites need to be developed and the avidity effect increases the overall binding affinity by orders of magnitude [128, 129]. Furthermore, targeting multiple sites enables a capsid pattern-sensing ability that ensures a productive binding to the assembled capsid that contains the viral genome.

An important discovery from this work is that the center pore of the CA-hexamer is a conserved interaction hub for both small-molecule and protein cofactors in the cell (**Figure 9-1B**). This could be suggesting the delicate and timely regulation of trafficking, uncoating, and reverse transcription, as the factors involved in these processes are targeting the capsid center. The positively charged center of the CA hexamer, generated by residue R18, serves as an ideal interaction site with the highly negatively charged FEZ1 protein. The critical role of the R18 residue has been well documented. When mutated, there are aberrant and much fewer capsids, resulting in strikingly reduced HIV-1 infectivity [24, 108]. This ring of R18 has been indicated to form a pore for the recruitment of nucleotides for reverse transcription inside the capsid [94], and also for coordinating the polyanion IP6 to stabilize the capsid [130]. I demonstrated here that this CA hexamer pore can also be targeted by protein cofactors (**Figure 9-1B**). Our MD simulations show that FEZ1 is able to reach down into this arginine ring in the center of the CA hexamer, possibly due to its inherently flexible and unstructured nature. It is

conceivable that other cellular proteins with flexible, negatively charged regions can also bind HIV-1 capsid through this interaction mode.

Much of the HIV-1 early post-entry infection events still remain to be discovered. Here I showed that FEZ1 acts as a kinesin-1 adaptor protein that interacts with the HIV-1 capsid directly via avid electrostatic interactions, thereby linking HIV-1 particles to the host transport system. Overall, this study demonstrates FEZ1 as a novel HIV-1 capsid pattern sensor, which targets the conserved cellular cofactor-binding site at the CA hexamer center, and supports the requirement of this virus-host factor interaction for efficient transport and early infection of HIV-1.

Further work is needed to structurally characterize the detailed atomic interaction of FEZ1 with CA. Even though extensive methods are used to obtain the structure, more effort would be needed to optimize the crystallization condition, adding in binding partners, or to test out more FEZ1 constructs. Another more ambitious goal would be to visualize the transportation of CA capsid along the microtubule, with all the motor proteins and the adaptor proteins involved – dynein-dynactin-BicD2 and kinesin-FEZ1 (**Figure 9-1A**).

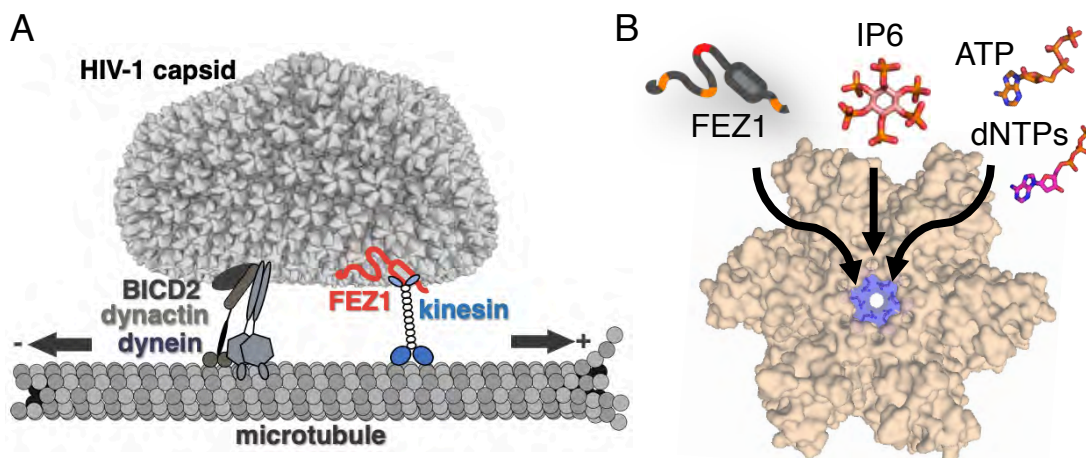


Figure 9-1 Schematic Models of HIV-1 Capsid Trafficking on Microtubules and a Conserved Targeting Site at the CA Hexamer Center

(A) Schematic of FEZ1 (red) bridging HIV-1 capsid to the kinesin motor (blue) and microtubule for trafficking (right). Other potential HIV-1 tracking machinery (BICD2/dynein/dynactin) is shown on the left. The arrows indicate the direction of trafficking. (B) Center of the CA hexamer is a conserved common interacting site for proteins (FEZ1), nucleotides (NTPs and dNTPs), and other cellular cofactors (IP6).

10 Material and Methods

10.1 Bacterial Strains

All molecular cloning was carried out in *E. coli* XL10-Gold Ultracompetent cells. All recombinant proteins were expressed and purified from the *E. coli* strain BL21(DE3). Both cell lines were routinely cultured at 37 °C while shaking at >220 RPM. XL10-Gold cells were grown in Luria Broth and BL21(DE3) cells were grown in either Luria Broth (starter culture) or Terrific Broth (for protein expression).

10.2 Human Cell Lines

Human microglia CHME3 cells (from undetermined sex) were previously described [63].

10.3 Protein expression and purification

N-terminal 6× His-tagged, GST-tagged, or MBP-tagged FEZ1 constructs were cloned into pET-28a (Novagen) with mutants created by QuickChange mutagenesis. They were transformed and expressed in *E. coli* BL21 (DE3) (Lucigen) grown in TB media to an OD₆₀₀ of 0.6 and induced with 0.5 mM isopropyl β-D-1-thiogalactopyranoside (IPTG) overnight at 16°C. The cells were harvested by centrifugation (5000 rpm, 10 min, 4°C) and resuspended in lysis buffer containing 50 mM Tris (pH 7.5), 400mM NaCl, and 0.1mM Tris(2-carboxyethyl)phosphine (TCEP) and followed by lysis with a microfluidizer. The lysate was centrifuged at 13,000 rpm for 40 min, 4°C and proteins were purified by passing through a nickel affinity column (Qiagen), a HiTrapQ anion exchange column (GE Healthcare) in 20 mM Tris (pH 8.0) using a 0–1000 mM NaCl (with 0.1mM TCEP) gradient elution, followed by a Superdex-200 gel-filtration column (GE Healthcare) in buffer 25 mM Tris (pH 7.0), 50 mM NaCl and 0.1 mM TCEP. The protein purity was examined by SDS-PAGE. All CA constructs were cloned into pET-11a (Novagen). CA proteins were overexpressed in *E. coli* BL21(DE3) cells at 25° C for 12 h by induction with 0.5 mM IPTG at OD₆₀₀ 0.6-0.8. CA proteins were purified by 25% w/v ammonium sulfate precipitation, dialysis into low-salt buffer (25 mM HEPES pH 7, 0.1 mM TCEP), and cation exchange chromatography. A list of the FEZ1 constructs used in this paper is summarized in **Table 4**.

| Construct | SEC | CA tube pelleting | ITC | Infectivity and trafficking |
|-------------------------------------|---|--|---|--|
| FEZ1 ₁₋₃₉₂ | | Binds CA tubes at physiological concentrations of salt, NTPs/dNTPs and IP6, and at pH 6, 7, or 8. No binding to R18D/R18A CA tubes. | | Functional for HIV-1 infectivity and virus core trafficking. |
| FEZ1 ₁₋₉₂ | Does not bind CA hexamer | Binds CA tubes at 50 mM but not at 150 mM NaCl. No binding to R18D CA tubes. | | |
| FEZ1 ₉₂₋₁₅₈ | Does not bind CA hexamer | Reduced binding to CA tubes with increasing salt concentrations. | | |
| FEZ1 ₉₂₋₁₉₈ | Binds CA hexamer, but not CA, 1/3- or 1/2-hexamer, pentamer, or 3-fold inter-hexamer interface. | Binds CA tubes at both 50mM and 150 mM NaCl. No binding to R18D CA tubes. | Binds CA hexamer at Kd ~300±60 nM | |
| FEZ1 ₉₂₋₁₉₈ 182-186EA | | | Binds CA hexamer at Kd ~2.5±0.3 μM | |
| FEZ1 ₁₅₈₋₁₉₈ | Binds CA hexamer | | | |
| FEZ1 ₁₅₈₋₁₉₈ 182EA | Reduced binding to CA hexamer | | | |
| FEZ1 ₁₅₈₋₁₈₂ | Does not bind CA hexamer | | | |
| FEZ1 ₁₇₈₋₁₈₈ | | Greatly reduced binding to CA tubes in the presence of 20 μM ATP, IP6, and nucleotides. | Strong binding to CA hexamer at Kd ~190±40 nM | |
| FEZ1 ₉₂₋₂₂₇ | Binds CA hexamer, greatly reduced binding to R18D CA hexamer | Binds CA tubes, but not with R18D tubes. Reduced binding to CA tubes with increasing salt concentrations. Binds CA tubes with CypA- and MxB-binding defective mutations. | | |
| FEZ1 ₁₉₈₋₃₉₂ | Does not bind CA hexamer | Binds CA tubes at 50 mM but not at 150 mM NaCl. No binding to R18D CA tubes. | | |
| FEZ1 ₁₋₃₉₂ 178-188EA | | | | Modest reduction in infectivity, no effect on trafficking |
| FEZ1 ₁₋₃₉₂ 158-198EA | | | | Significant defects in infectivity and trafficking |

Table 4 Summary of FEZ1 constructs.

10.4 Analytical size-exclusion chromatography (SEC)

The interaction between FEZ1 and cross-linked CA (A14C/E45C) hexamers was examined by SEC. CA hexamers were assembled as described previously [14]. Purified samples of FEZ1 (80 μM) were mixed with CA hexamer (20 μM) and applied to a Superdex 200 10/300 GL column (GE Healthcare) pre-equilibrated in 25 mM Tris, pH 8.0, 50 mM NaCl buffer. FEZ1 binding tests with small capsid assemblies (**Figure 3-1**) used 200 μL reaction volumes with 33 μM FEZ1 and 98 μM CA monomer (of the appropriate assembly). The UV absorbance at 280 nm was recorded to monitor the elution of FEZ1 and CA hexamer. For a typical SEC run, the eluted peak has a total volume of ~2 mL, resulting in a dilution factor of ~10.

10.5 CA Tube Pelleting Assay with purified FEZ1 proteins

Cross-linked CA (A14C/E45C) R18 (WT) and R18D tubes were dialyzed overnight at 4 °C into assembly buffer (1 M NaCl, 25 mM Tris pH 8.0), followed by dialysis into binding buffer (50 mM NaCl, 25 mM Tris pH 8.0). FEZ1 proteins were spun at 20,000 × g for 30 min at 4 °C. FEZ1 (5 μM) proteins were added to CA tubes and incubated at room temperature for 30 min. Subsequently, 7 μL aliquots were withdrawn and labeled as total. The remaining was pelleted at 20,000 × g for 30 min at 4 °C. Total, supernatant, and pellet samples were analyzed by SDS-PAGE. Pelleting experiments with ATP and dNTPs were performed as described with ATP concentrations as described and 20 μM dNTPs.

10.6 Isothermal Titration Calorimetry

The affinity of the FEZ1 protein for CA hexamer was determined using isothermal titration calorimetry (Nano ITC; TA Instruments). FEZ1 and the CA hexamer were dialyzed overnight in the buffer 25 mM Tris (pH 8), 50 mM NaCl. The CA hexamer (120 μM concentration in the syringe) was added in 30 injections of 1.6 μL into a 15 μM solution of purified FEZ1 protein at 25 °C in the cell. Data were analyzed using the NanoAnalyze software from TA Instruments. Results are from 3 independent experiments, and is represented as mean ± standard deviation.

10.7 Crystallization and data collection

Crystallization was performed using the microbatch under-oil method [131]. Protein sample at 2 mg/mL was mixed with precipitant at a 1:1 ratio (1 μL protein:1 μL precipitant) at room temperature. R18D CA in 50 mM NaCl, 25mM Tris pH 8 was crystallized in the condition containing 0.1M Tris-HCl pH 8.5, 8 % PEG 8000. Crystals were cryoprotected with precipitant containing 25% (Vol/Vol) glycerol before freezing in liquid nitrogen. All diffraction data were collected at the Advanced Photon Source NE-CAT beamline 24-IDE. Data statistics are summarized in **Table 1**.

10.8 Structure determination and refinement

The structure was solved by molecular replacement using PHASER [132] using the previously published CA structure (PDB: 3H47) as a search model. The model was refined with iterative rounds of TLS and restrained refinement using Refmac5 [133] followed by rebuilding the model to the $2F_o - F_c$ and the $F_o - F_c$ electron density maps using Coot [134]. Refinement statistics are summarized in **Table 1**. PyMol [135] with the APBS (Adaptive Poisson-Boltzmann Solver) [136] plug-in was used to calculate the surface electrostatic potential.

10.9 Negative-staining electron microscopy (EM)

To prepare samples for negative stain, the CA tubes were assembled as described above. Aliquots (3 μl) were adsorbed to a glow-discharged, 400-mesh, carbon-coated copper grid and stained with fresh uranyl formate (2%). Images were recorded on a TF20 electron microscope (FEI) equipped with a field-emission gun at the indicated magnification on a 4k × 4k Gatan UltraScan charge-coupled device camera (Gatan).

10.10 Atomic model building for molecular dynamic (MD) simulations

Initial coordinates of the HIV-1 CA hexamer were generated from a native full-length HIV-1 capsid protein (PDBID: 4XFX) [11], applying a six-fold symmetry. The two missing loops, residue 5 to 9 and residue 222 to 231, in the original 4XFX model were built using the model builder algorithm Modeller [137]. In addition, the protonation states of the titratable residues, particularly histidine, asparagine, lysine and cysteine, at pH 7.4, were determined and assigned by PDB2PQR [138]. There was no available atomic model of human FEZ1 protein when conducting this study. The initial model of the FEZ1₁₇₈₋₁₈₈ peptide was built by using the ab initio modelling protocol in Rosetta [139]. The glutamate and aspartate residues were all in deprotonated form, which resulted in -6 charges for this peptide. After being equilibrated in explicit water for 0.5 μ s, this FEZ1 peptide was combined with the CA hexamer model and placed at the entrance of the CA hexamer center channel. This complex was then solvated in a 110 Å x 120 Å x 90 Å TIP3P [140] water box and neutralized by 150 mM NaCl. The total atom count of this resulting FEZ1-CA hexamer model was ~122 K.

10.11 System preparation for MD simulation

After model building, the prepared model underwent a two-step energy minimization. The CA and FEZ1 protein were fixed at the first 10,000 steps of minimization, while the water molecules and ions were free to move. In the second minimizing stage, the fixed atoms were relieved but the heavy atoms of the proteins were restrained by a force constant of 10 Kcal/mol Å² for another 10,000 steps. The minimized model was then thermalized to 310 K with a rate of 1,000 steps/K while the harmonic restraints on protein heavy atoms were maintained. Next, these harmonic restraints on the heavy atoms were gradually released during a 100,000-equilibration run under 310 K and 1 bar. Minimization, thermalization and equilibration runs were carried out in NAMD 2.12 [141] at a time step of 2 fs. All bonds to hydrogen were constrained with the SHAKE (solute) or SETTLE (solvent) algorithms. Temperatures were regulated by the Langevin thermostat algorithm employing a damping coefficient of 1 ps⁻¹. The pressure was maintained by the Nose-Hoover Langevin piston pressure control, allowing isotropic cell scaling.

10.12 MD simulation production runs on Anton2

The production runs of Fez1-CA hexamer system were performed for 2 μ s on the special purpose supercomputer Anton2 [142] at the Pittsburgh Supercomputer Center (PSC). The CHARMM 36m [143] force field for protein was employed in the MD simulations. During the simulation, the temperature (310 K) and pressure (1 bar) were maintained by employing the Multigrator integrator [144] and the simulation time-step was set to 2.5 fs/step, with short-range forces evaluated at every time step, and long-range electrostatics evaluated at every second time step. Short-range non-bonded interactions were cut off at 17 Å; long range electrostatics were calculated using the k-Gaussian Split Ewald method [145]. The C α atoms involved in 2- and 3-fold inter-hexamer interfaces, namely helices 9, 10 and 11, were restrained with a force constant 1.0 Kcal mol⁻¹ Å⁻², to mimic the interactions with neighboring CA-hexamers in the P6 periodic cell.

10.13 Viruses

To generate HIV-1 luciferase reporter virus pseudotyped with WT envelope (HIV-1-WT-Luc), 293T cells were co-transfected with a plasmid encoding WT envelope along with the plasmid, pNL4.3.luc.R-E- (AIDS Reagent Repository no 3418). A GFP-tagged Vpr expressing vector was included in these co-transfections to generate a fluorescent version of this virus, HIV-1-WT-Luc-GFP-Vpr (Delaney et al 2017).

10.14 Generation of stable pools

Retroviruses encoding either control Flag (Control), or C' terminally FLAG-tagged versions of full length human FEZ1 (FEZ1), or the FEZ1 mutants (FEZ1^{1-392 178-188EA} and FEZ1^{1-392 158-198EA}) were used to infect human microglia CHME3 cells followed by selection to generate stable expressing pools, as previously described (Malikov et al 2015).

10.15 RNAi and measurement of early HIV-1 infection

For transient knockdowns, CHME3 cells were transfected with 60 pmol of a custom-made siRNA duplex targeting the FEZ1 3'-UTR (FEZ1nc), obtained from Ambion (siRNA sense and antisense sequences are CUUAUACUCUUAAGACUAAtt and UUAGUCUUAAGAGUUAAGct, respectively) using oligofectamine RNAiMAX transfection reagent (Invitrogen) as described previously (Malikov et al 2015). siRNA-treated cells were infected with HIV-1-WT-Luc for 48 h. Cultures were then lysed and luciferase activity was measured using the Luciferase Assay System (Promega). Knockdown levels were confirmed by western blot analysis using anti-FEZ1 antibodies (Cat #4280 from Cell Signaling). GAPDH was detected using anti-GAPDH (Cat #sc-25778 from Santa Cruz). The results are representative of at least three independent experiments.

10.16 Live imaging and analysis

CHME3 cells plated on 35-mm collagen-coated glass culture dishes (MatTeck, P35G-1.5-14C) were infected with HIV-1-WT-Luc- GFP-Vpr in CO₂-independent media via spinoculation for 30 min. The media was changed and acquisition locations were set up within the first 20 min. Timestamps starting at 0 represent the start and period of live-cell video microscopy beginning at 20 min post-infection, performed at 3 frames per min for 2 h. Short interval acquisitions were performed at 1 fps for a period of 300s as described previously [63]. Number of particles near nuclei were determined using MetaMorph imaging software (Molecular Devices). Up to 190 viral particles were counted per sample, and each experiment consisted of 2-4 cells. One-way ANOVA for correlated samples, with a confidence interval of 95% or greater was used to determine statistical significance in at least two independent experiments for each condition. Single virus particles were tracked in the TrackMate ImageJ plugin v2.8.1 [146] using estimated blob diameter 8.0 pixels, threshold 100 and frame to frame linking max distance 30 pixels. XML trace files were analyzed using Python 3.7.0 Jupyter notebooks (5.6.0) with Pandas (0.23.4) and Matplotlib (2.2.3) packages. In 3 independent experiments 1600-2800 tracks in 9-13 cells were analyzed per each condition. Equal-variances t-test was used to determine

statistical significances between data sets. The following representations of P values were used: *P<0.05, **P<0.01, ***P<0.001.

10.17 Data Deposition

The R18D CA hexamer structure and diffraction data have been deposited in the Protein Data Bank with an accession code of 6OMT.

11 Publications and News Articles

Publications:

Huang P*, Summers BJ*, Xu C, Perilla JR, Malikov V, Naghavi MH & **Xiong Y.** (2019). FEZ1 is recruited to a conserved cofactor site on capsid to promote HIV-1 trafficking. ***Cell Reports*** 28, 2373-2385. Epub Aug. 14, 2019.

Summers BJ, Digianantonio KM, Smaga SS, Huang P, Zhou K, Gerber EE, Wang W & **Xiong Y.** (2019). Modular HIV-1 Capsid Assemblies for Investigating Diverse Host-Capsid Recognition Mechanisms. ***Cell Host & Microbe*** 26, 216.

Commentary and News Articles:

[Building Complexity: Making and Breaking Synthetic Subunits of the HIV Capsid](#)

Leo C. James & Till Bocking

Cell Host & Microbe, Volume 26, Issue 2, 14 August 2019, Pages 151-153

[Study sheds light on HIV protein mechanisms](#)

ISHANA AGGARWAL 1:24 AM, SEP 03, 2019

Yale Daily News

[Researchers describe building blocks of HIV's protective shell](#)

By Bill Hathaway August 14, 2019

Yale News

Elucidating the mechanism of how yeast kinesin Kip2 promotes microtubule polymerization

1 Introduction

1.1 Tubulins and Microtubule

1.1.1 Microtubule introduction

$\alpha\beta$ -tubulin forms a stable heterodimer with each subunit bound to a guanine nucleotide, the GTP bound at the α -tubulin N-site (non-exchangeable site) is always buried in the interfaces within the tubulin dimer while β -tubulin had the E-site (exchangeable site) and can be hydrolyzed following incorporation into the microtubule lattice [147-150]. Unpolymerized tubulins exists as α -/ β -tubulin heterodimers, which are assembled longitudinally in a noncovalent, head-to-tail fashion into protofilaments, that in turn forms the 25-nm hollow cylindrical tubular structures, microtubules [151]. The canonical microtubules are made up of 13 protofilaments [152], but *in vitro*, microtubules ranging from 10 to 17 protofilaments are reported, with 14 protofilaments being the most common [153] (**Figure 9-1A&B**).

Microtubules are polar structures with the α -tubulin marking the side of the minus-end, while β -tubulin marks the plus-end of microtubules [154-156]. In cells, the microtubule minus-end is anchored to microtubule-organizing centers, and the most known factor being γ -tubulin ring complex (γ -TURC) [157]. Besides the microtubule nucleating activity of the γ -TURC, it can also bind and cap the minus ends of pre-formed microtubules [158]. In budding yeasts, the microtubule minus-end is tethered to the spindle pole body (SPB) [159]. On the other hand, the plus-end of microtubule is usually

extending towards the cell periphery, where it is freely exploring the cellular space via the “search and capture” mechanism [160, 161]. Indeed, microtubules exhibit a phenomenon called dynamic instability, in which the plus-ends of microtubules are constantly undergoing periods of polymerization / growth and depolymerization / shrinkage, caused by the addition and loss of $\alpha\beta$ -tubulin subunits [160]. The switch from growth to shrinkage is termed catastrophe, while the reverse is termed rescue [162] (**Fig 9-1C**).

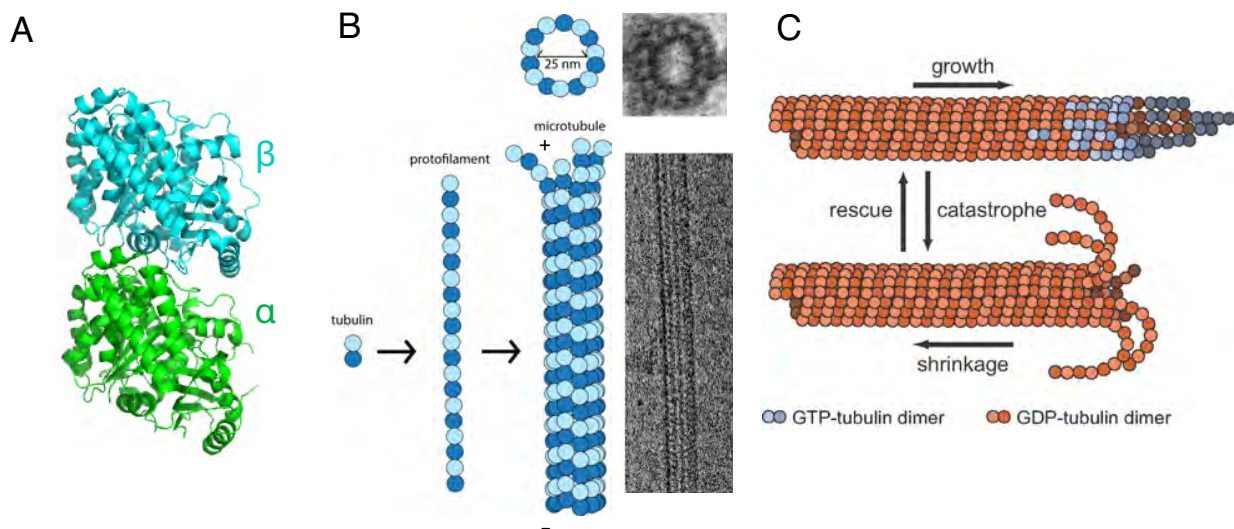


Figure 9-1 Microtubules are dynamic structures

(A) Structure of an α - β -tubulin heterodimer. (B) Microtubule is composed of protofilaments, which is in turn formed from alignment of tubulin heterodimers. The negative-staining EM image of the top view and side view of microtubules are shown. EM image adapted from [163]. (C) Microtubules exhibit dynamic instability, namely slow growth and rapid shrinkage. Adapted from [164].

1.1.2 MAPs regulate MT functions and dynamics

Microtubules play diverse roles in the cells, including cell motility, cell mitosis, and cargo transportation. They are regulated by large numbers of microtubule associated proteins (MAPs) [165, 166]. Generally, these MAPs can be categorized into different classes by their activity [167, 168]: proteins that stabilize microtubules, proteins that destabilizes or severs microtubules, plus-end tracking proteins (+TIPs) that regulate microtubule growth and catastrophe, reviewed in [169], and also motor proteins that utilize the energy of

nucleotide hydrolysis to generate force along microtubule, including transportation motors dynein and kinesin-1, and the microtubule sliding motors, kinesin-5 and -12 (which will be discussed in detail in the next part).

The first class of proteins that stabilizes microtubules includes proteins that promote polymerization and/or slow depolymerization. An example is the multi-TOG-domain proteins, such as XMAP215/DIS1 that are found in a wide range of organisms [170-172]. XMAP215 is a processive polymerase that adds multiple tubulin dimers to the growing plus-end and promotes microtubule polymerization [173]. Other examples include the classical MAPs (tau, MAP2, and MAP4), which contain common repeat structures and bind along the microtubule lattice and stabilizes it [174, 175]; the MAP6 or STOP (Stable-Tubule-Only Polypeptide) protein that protect microtubules from depolymerization in conditions such as low temperatures or treatment with depolymerizing drugs [176]; and the doublecortin and EMAP families, which are essential for neuronal migration during human brain development [177] and cancer [178], respectively. This class also includes proteins that associate with the minus ends of the microtubule and protect them from depolymerization, such as patronin and CAMSAP [179, 180].

The second class are proteins that are microtubule depolymerizing or severing proteins, including mitotic centrosome-associated kinesin (MCAK), spastin, and katanin [181, 182]. MCAK can remove the stabilizing GTP-cap and trigger catastrophe, while spastin and katanin are ring-shaped hexameric AAA ATPases that can bind to and generate internal breaks and sever microtubules into short pieces [182-184].

The third class are the plus-end tracking proteins +TIPs, such as the CLIP170, EB1, or Ndc80. CLIP-170 is the first identified +TIP [185, 186], that functions as an anti-catastrophe factor in fission yeast [187] and promotes rescue *in vitro* [188]. EB1 tracks the growing microtubule plus-end [189] and serve as a hub for other MAPs [190]. They increase microtubule rescue frequency and decrease the microtubule shrinkage rate [191-193]. The kinetochore–microtubule linker Ndc80, functions in cell mitosis [194].

To sum up, the functions of microtubules are closely regulated by a wide array of different MAPs.

1.2 Kinesins

1.2.1 Microtubule-based motor proteins

Active transport along directional cytoskeletal filaments is important in maintaining normal cell functions. Three large families are identified as molecular motors that participates in intracellular transport, myosin [195], dynein [196], and kinesin [197]. Myosin walks along actin-filaments to transport and drive muscle contraction. Dynein is a minus-end directed motor that is important for the motility of cilia and flagella [198, 199]. Kinesin moves along the microtubule for cargo transportations, cell motility, or cell mitosis [200].

All of these motors utilize the chemical energy from ATP hydrolysis to drive conformational changes that generate motile force. Here, I will focus on kinesin superfamily proteins.

1.2.2 Kinesin superfamily

Conventional kinesin, kinesin-1, was first discovered in 1985 from the giant axon of the squid [197, 201]. Kinesin-1 is a tetramer that consists of two kinesin heavy chains (KHC) with motor activity at one end, followed by α -helical coiled-coil dimerization domain (also known as stalk), and a tail that can interact with vesicles or organelles through its association with two kinesin light chains (KLC) [202]. Kinesins can exist in monomers, dimers or tetramers. Since then, a large family of kinesin proteins have been identified using genetic and biochemical approaches, and there are more than 600 kinesin sequences found in eukaryotes [202, 203].

A standardized nomenclature system introduced in 2004 renamed kinesins into numbers [204], and there are 14 groups with some ungrouped or orphan kinesins. Kinesins within the same family perform similar cellular functions [205, 206], and these kinesins contain a highly-conserved globular motor domain that consists of the microtubule binding site [207] and the ATP hydrolysis catalytic pocket [208]. The structure of the motor domain was first identified by x-ray crystallography of truncated constructs derived from rat kinesins [209, 210], and now many more kinesin motor domain structures are determined [reviewed in [202]]. The position of the kinesin motor domain can be at either the N- or C-terminus, or in the middle of the kinesin polypeptide chain [211]. Generally speaking, kinesins with amino-terminal motor domains move towards the plus-end of microtubules, while kinesins with carboxyl-terminal motors move towards the minus-end. Kinesins with a central motor domain usually destabilizes microtubules, such as Kif2A of the kinesin 13 family [212]. In contrast to the highly-conserved motor domain,

the N- or C-terminus of kinesins are evolutionarily diverged [213], and serve a wide variety of functions in cells.

1.2.3 Kinesins regulate microtubule dynamics

Kinesins utilize the mechanical energy from ATP-hydrolysis for a conformational change that results in a power stroke for force generation and production of mechanical work [214-216]. Kinesin-1 moves along the microtubule in a hand-over-hand manner [217], and it is a highly processive motor protein that takes more than hundred steps before dissociating from the microtubule [218-220]. Each step is 8 nm [221], and it hydrolyzes one ATP per step [222, 223]. In contrast, there are non-processive kinesins such as *Drosophila* kinesin-10 Nod [224], or those that have an unconventional ATP hydrolysis cycle, such as *Xenopus* kinesin-13 MCAK [225] which targets the microtubule end by diffusion and uses ATP-hydrolysis to remove tubulin dimers [226].

1.2.4 Kinesins throughout the budding yeast cycle

The genome of budding yeast is relatively small and tractable, giving it the advantage for studying motor proteins involved in mitotic spindle function. In budding yeasts, there are one cytoplasmic dynein, Dyn1, and six kinesins, Cin8, Kip1, Kip2, Kip3, Kar3, and Smy1 [227] (**Figure 9-2**). There are three main functions of these budding yeast motor proteins: transportation of cargoes, microtubule attachment to the cortex, and the regulation of microtubule dynamics. Of these seven motor proteins, only Smy1 is not involved in spindle function [206, 228], while the rest of them are essential for yeast cell

mitosis and participates in mitotic spindle function and positioning. Because of the functional overlap of these motors, none of them are uniquely required for cell viability [227].

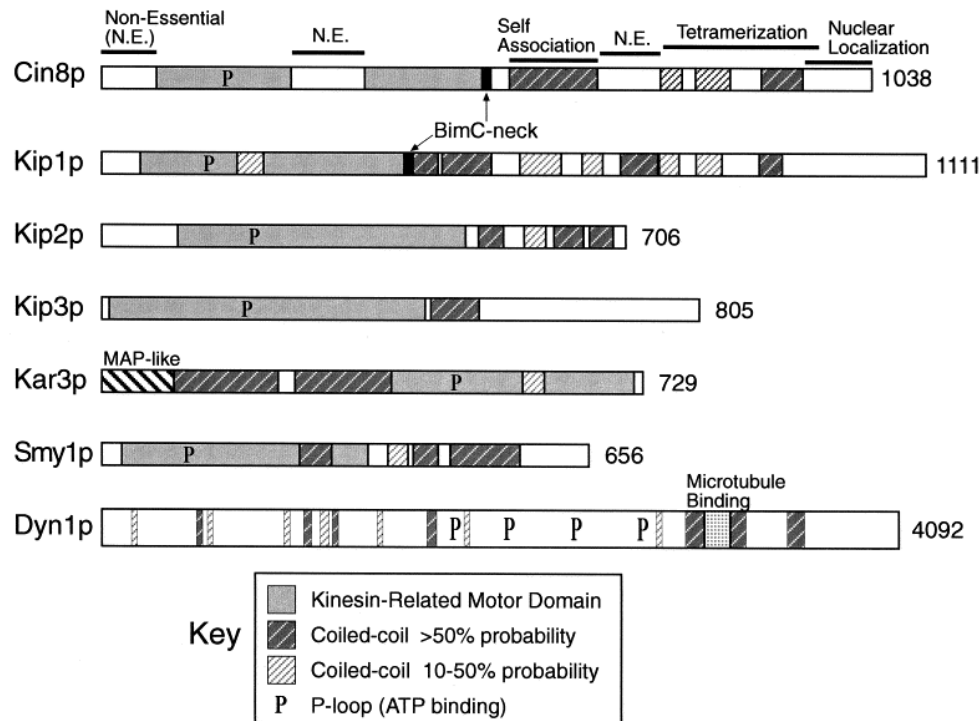


Figure 9-2 Kinesin and dynein motors in the budding yeast.

These are the eight motor proteins discovered in budding yeast. The motor domain, ATP binding site, and also the coiled-coil regions are indicated. Adapted from [227].

1.3 Kip2

1.3.1 Identification of *Saccharomyces cerevisiae* kinesin Kip2

Kip2, kinesin-related protein 2, was first identified in a PCR screening for the highly-conserved regions of the kinesin motor domain [229]. Kip2 shows 38% amino acid sequence identity to *Drosophila melanogaster* KHC [229], and the conserved sequence includes the microtubule binding site [207] and the GX₄GKT ATP binding and hydrolysis site [208].

Originally, Kip2 was classified as a member of the kinesin-7 family, based on the close homology to the conserved motor domain of kinesin-7 CENP-E [230-232]. However, the N- and C-terminus of Kip2 has diverged from other kinesin families, and now it is more thought of as an “orphan” kinesin motor.

The Kip2 gene is located on the left arm of chromosome 16, and has an open reading frame of 706 amino acids [233][234]. The motor domain of Kip2 is 102-493 amino acid, and the C-terminus of Kip2 is predicted to have three α -helical coiled-coil forming heptad repeats, which is involved in the dimer formation of Kip2 [229][235]. The 90-amino acid long N-terminus of Kip2 is rich in serine residues [229], and contains phosphorylation sites that can be phosphorylated by kinases such as mitotic Cdc28 (the budding yeast Cdk1) [236], and GSK-3/Mck1 [237].

1.3.2 Kip2 regulates microtubule dynamics indirectly in budding yeast cell mitosis by transportation of other MAPs to microtubule plus-ends

Kip2 was first shown to participate in yeast cell mitotic spindle positioning in 1997 [238, 239]. Spindle positioning in budding yeast ensures that the spindle elongates along the mother-bud axis during anaphase. In this paper, they found that *KIP2* deletion strains had more nuclear migration effect and thus higher level of binucleate cells [238]. Furthermore, *kip2 Δ* cells had shorter and lower numbers of cytoplasmic microtubules than wild-type, and is more sensitive to the microtubule depolymerizing drug benomyl [238]. The phenotype of low cytoplasmic microtubule numbers was most distinct during telophase, suggesting that stabilization of microtubules by Kip2 occurs during this cell

stage [240]. Deletion of KIP2 results in extremely short astral microtubules (aMTs), whereas KIP2 overexpression leads to cells with abnormally long aMTs [241]. These studies shown that Kip2 mediates MT stabilization against depolymerization [238, 241, 242].

In yeasts cell mitosis, spindle positioning depends on two overlapping pathways, the dynein (dyn1) pathway and the Kar9 pathway. In both pathways, Kip2 transports +TIPs (including yeast homologues of EB1 (Bim1) and CLIP-170 (Bik1)) to the plus-ends of aMTs. In the Kar9 pathway, Kip2 is needed for sufficient accumulation of the +TIP Kar9 at aMT plus ends [243], where Kar9 mediates interactions of aMTs with cortical actin for pre-anaphase spindle positioning and nuclear migration close to the bud [244-246]. In the dynein pathway, Kip2 transports Bik1 and cytoplasmic dynein from the spindle poles to the plus ends of aMTs [241, 247-249]. Subsequently, dynein is unloaded from aMTs and bound at the cell cortex, where it pulls on aMTs and promotes correct positioning of the mitotic spindle in anaphase [250]. These studies demonstrate that Kip2 indirectly regulates microtubule dynamics through transportation of other proteins like Bik1, Bim1, and dyn1, and that the microtubule growth promotion is dependent on Bik1 [241, 247-249].

1.3.3 Kip2 directly regulates microtubule dynamics by acting as a polymerase and anti-catastrophe factor

Using microtubule dynamic assays, Anneke et al. found that Kip2 alone *in vitro* is a microtubule polymerase and an anti-catastrophe factor [251]. In the presence of ATP,

Kip2 increased the growth rate of microtubules about 3-fold and decreased the catastrophe frequency around 10-fold, with no effect on the shrinkage or rescue rate. Kip2 is a highly processive motor, that the average run distance before dissociating was $4.1 \pm 0.3 \mu\text{m}$ (also known as the run length). The velocity of Kip2 is $5.0 \pm 0.9 \mu\text{m/s}$, and it was shown to be dwelling at the microtubule plus-end for $30 \pm 26 \text{ s}$ before dissociation. Thus, Kip2 is a highly processive motor with long run lengths and end residence times. Moreover, they found that Kip2 promotes microtubule growth in a length-dependent manner, meaning that the increase in microtubule growth rate as well as the reduction in catastrophe frequency by Kip2 is proportionate to increasing length of microtubules. In summary, Anneke et al. found that Kip2 promotes microtubule growth *in vitro* in a length-dependent manner using positive feedback mechanism, and “pave its own way” during yeast cell mitosis.

1.4 Aims and Scope

Microtubules are dynamic structures that play essential roles in the cell cycle, cell motility, and cellular transport, and are regulated by a diverse array of microtubule associated proteins (MAPs) or motor proteins. Kip2 is a yeast kinesin motor protein that can translocate processively along the microtubules to the plus-end and is involved in mitotic spindle positioning and stabilization of microtubules during cell cycle [238, 240].

Previously, it was thought that Kip2 regulates microtubule length indirectly by transporting microtubule positive regulators Bik1 and dynein to the microtubule plus end [241, 247]. Recently, Hibbel et al. found that Kip2 alone can directly increase microtubule

growth [251]. However, the molecular mechanism by which Kip2 increases microtubule growth rate is unknown. Because Kip2 is able to processively translocate to and dwell on the microtubule plus-end for around one minute, I hypothesize that Kip2 acts as a polymerase and catalyzes the addition of tubulins to the microtubule plus end. To test this, I aimed to map the binding interface(s) of Kip2 with tubulins, perform microtubule dynamic assays and motility assays to examine the dynamic instability parameters and the effect on microtubule growth, and the ultimate goal was to obtain the structure of Kip2-tubulin/microtubule complex. These results will unveil the molecular mechanisms of how Kip2 promotes microtubule polymerization.

2 Biophysical and Biochemical Properties of Kip2

2.1 Expression and purification of Kip2

To observe the effect of full-length Kip2 (Kip2FL) promoting microtubule polymerization, I have expressed Kip2FL in *E. coli* cells and for purification by protein column chromatography (**Figure 10-1A**). The purification scheme is first through an affinity Ni column, because all of the Kip2 constructs have a His-tag. Next, the proteins were run through gradient ion exchange column, and then through the size exchange column. I was able to obtain a good amount of homogeneous protein for experiments (**Figure 10-1B**).

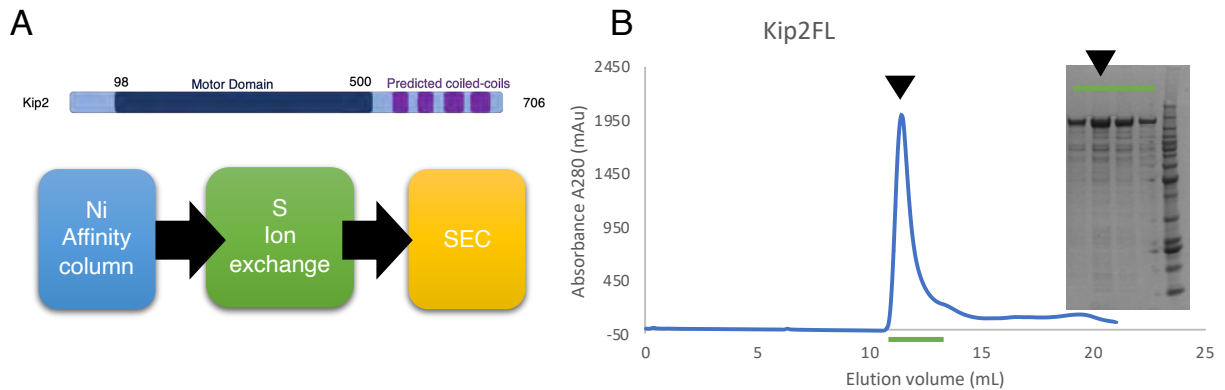


Figure 10-1 Purification of Kip2FL

(A) Schematic of domains of the full-length Kip2 protein (Kip2FL), and the purification method. (B) Size exclusion chromatography of the Kip2FL.

2.2 *In vitro* reconstitution of microtubule dynamics

To answer biological questions, *in vitro* reconstitution methods can be useful. It can confirm molecular models and hypothesis without the complicated environment inside cells [252]. In this approach, purified proteins are used to reconstitute a minimal process of interest, and this provides a valuable experimental tool for understanding the biochemical processes.

In the field of reconstitution of microtubule dynamics, numerous studies have been devoted to the development of novel microscopy-based assays to probe microtubule dynamics [253], and also to reconstitute microtubule dynamics under physiological conditions [254]. Moreover, *in vitro* assays have been used to probe microtubule dynamics mechanistically [255], to reconstitute microtubule plus-end tracking [256], and to characterize various MAPs [173, 257, 258]. It has proven to be a powerful tool in the field of study of microtubules.

Previously, it was showed that Kip2 enhances microtubule growth *in vitro* [251]. In order to further study the mechanism of how Kip2 promotes microtubule polymerization,

I made different Kip2 constructs and utilized the *in vitro* reconstitution of microtubule dynamics. To determine the effect of different Kip2 constructs on microtubule dynamics, microtubules were grown at 12 μ M free bovine tubulin from the ends of GMPCPP-stabilized microtubule seeds made from rhodamine-labeled porcine tubulin (TAMRA-tubulin) [259] (**Figure 10-2**). Stabilized microtubule seeds were imaged using EPI-fluorescence, whereas dynamic microtubule extensions were imaged using IRM microscopy at a frame rate of 0.33 Hz.

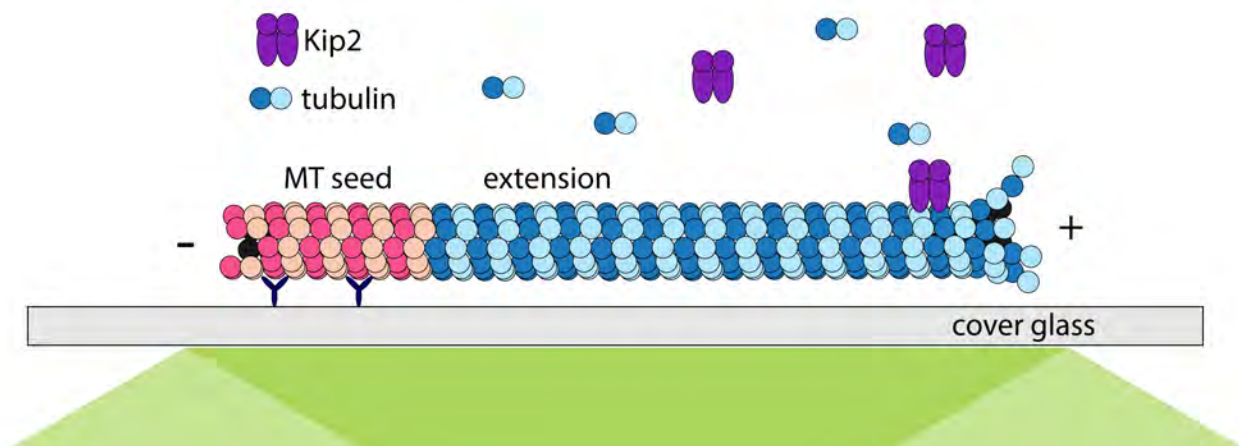


Figure 10-2 Schematic of dynamic microtubule assay

Schematic of the experimental design. Non-labeled porcine tubulin in solution polymerizes onto the ends of GMPCPP-stabilized, rhodamine-labeled microtubules (red) bound to the coverslip with anti-rhodamine antibodies (blue).

2.3 Full-length Kip2 promotes microtubule growth by acting as a microtubule polymerase and anti-catastrophe factor

Kip2 was shown to promote microtubule growth by enhancing the growth rate and reducing the catastrophe frequency [251]. To confirm this effect of Kip2 on microtubule dynamics, I repeated the *in vitro* microtubule dynamic assays with 0 nM, 20 nM, and 40

nM full-length Kip2 (Kip2FL), in the presence of 1 mM ATP and 12 μ M bovine tubulin. Addition of Kip2 greatly increased the average microtubule length from $3.2 \pm 0.1 \mu\text{m}$ without Kip2 (control, 0 nM Kip2), to $7.3 \pm 0.2 \mu\text{m}$ at 20 nM Kip2, and to $10.2 \pm 0.2 \mu\text{m}$ at 40 nM Kip2. (**Figure 10-3 A**). The mean length of the freshly polymerized microtubules was measured ten minutes after addition of Kip2 and tubulin to the surface-bound microtubule seeds. Note that with high concentrations of Kip2, there was no catastrophe so the microtubules grew extensively long and are frequently curving and bending out of the TIRF field, so it became increasingly difficult to measure microtubule length.

Next, I measured the growth rate, shrinkage rate, and catastrophe frequency of microtubules with 0 nM, 20 nM, and 40 nM Kip2FL, in the presence of 1 mM ATP and 12 μ M bovine tubulin. In **Figure 10-3 B**, I can see that these kymographs revealed that microtubules undergo catastrophe, the switching from slow growth to rapid shrinkage, both with and without Kip2 present in the assay. Thus, dynamic instability of microtubules was successfully reconstituted *in vitro*. Microtubule growth rate was increased up to 2-fold from $0.45 \pm 0.01 \mu\text{m}/\text{min}$ without Kip2 to $0.64 \pm 0.01 \mu\text{m}/\text{min}$ at 20 nM Kip2, and to $0.83 \pm 0.02 \mu\text{m}/\text{min}$ at 40 nM Kip2 (**Figure 10-3 B**).

To quantify the effect of Kip2 on catastrophe frequency, the total number of catastrophes observed per experimental condition was divided by the total duration of microtubule growth of all microtubules in that experimental condition. This microtubule catastrophe frequency strongly decreased from 0.19 per minute without Kip2, to <0.05 per minute at 20 nM Kip2 and to <0.005 per minute at 40 nM Kip2 (**Figure 10-3 C**).

Lastly, microtubule shrinkage rate was quantified from the slope of microtubules that experienced catastrophe, for all microtubules per experimental condition. Kip2 did not affect microtubule shrinkage rate at 20 nM Kip2 (**Figure 10-3 D**). At 40 nM Kip2, catastrophe events were too rare to reliably quantify microtubule shrinkage velocity. In summary, microtubules shrink at a rate of $\sim 8 \mu\text{m}/\text{min}$, regardless of whether Kip2 is present in the assay.

To sum up, *in vitro*, full-length Kip2 alone increases the average microtubule length and growth rate, and reduces the catastrophe frequency, without affecting the shrinkage rate. These results are consistent with the findings in literature [251].

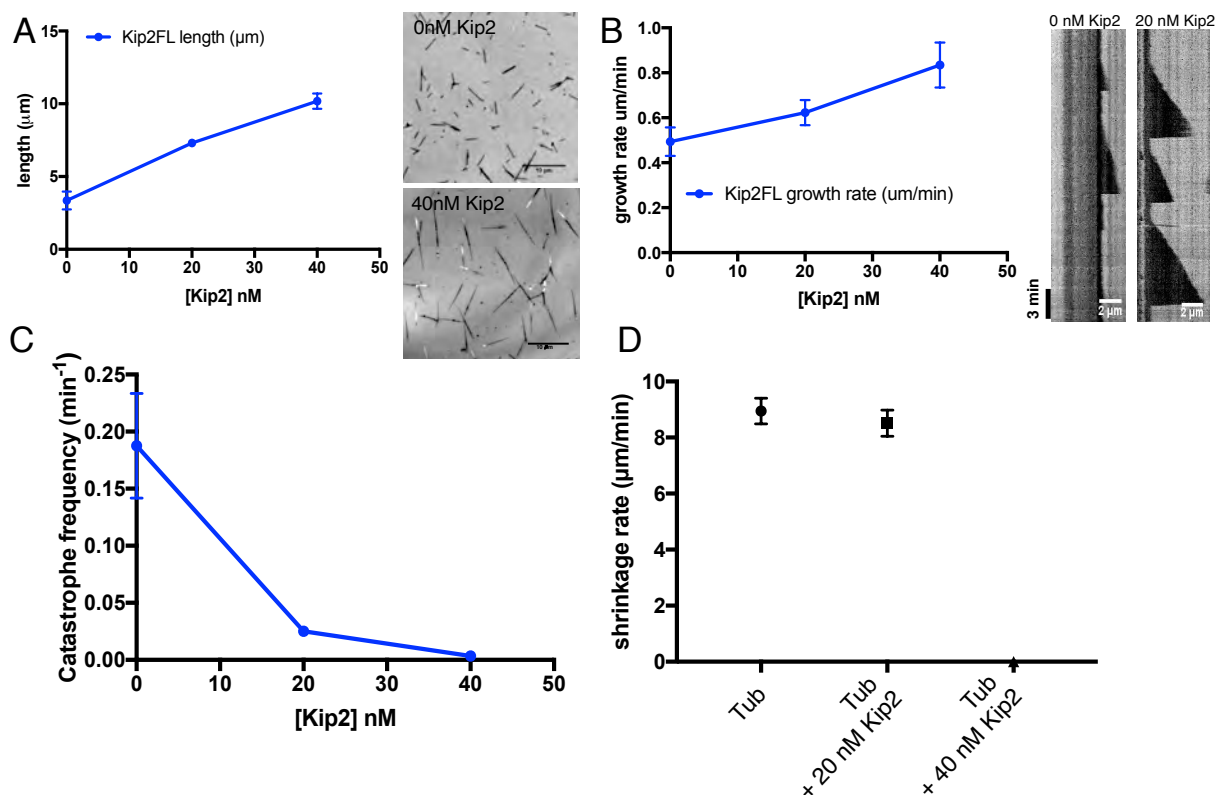


Figure 10-3 Full-length Kip2 increases the growth rate and reduces the catastrophe frequency of dynamic microtubules

(A) Kip2FL increases the length of microtubules. (B) Kip2FL increases the growth rate of microtubules. (C) Kip2FL reduces the catastrophe frequency of microtubules. (D) Kip2FL has no effect on the shrinkage rate of microtubules.

2.4 Kip2 C-terminus may contain potential tubulin/microtubule interaction site

I have successfully reconstituted the microtubule dynamic system of full-length Kip2 and obtained comparable dynamic results to published literature [251]. The polymerase activity of Kip2 suggests that it contains binding sites for tubulins/microtubules, so next I examined the Kip2 sequence and tried to pinpoint the binding site of Kip2 with tubulins/microtubules.

I first looked at the Kip2 C-terminus (Kip2C, Kip2 residues 561-706, Kip2 region after the motor domain) and found that it contains positive charges that could potentially interact with the negatively charged tubulin tail. Moreover, structural prediction with PSIPRED and COILS showed that it has multiple helices and four coiled-coils (**Figure 10-4 A&B**), which could be important for dimerization and maybe also the interaction sites for cargo or adaptor proteins. Another piece of evidence comes from the result that the N-terminus of Kip2 (Kip2 residues 1-80, Kip2 region before the motor domain) is dispensable for promotion of microtubule growth and motility while C-terminus is not (**Figure 10-4 C**) [251]. Moreover, Kip2C seems to bind to microtubules in a microtubule pelleting assay **Figure 10-4 D**). Therefore, I decided to look into the effect of Kip2C on microtubule dynamics.

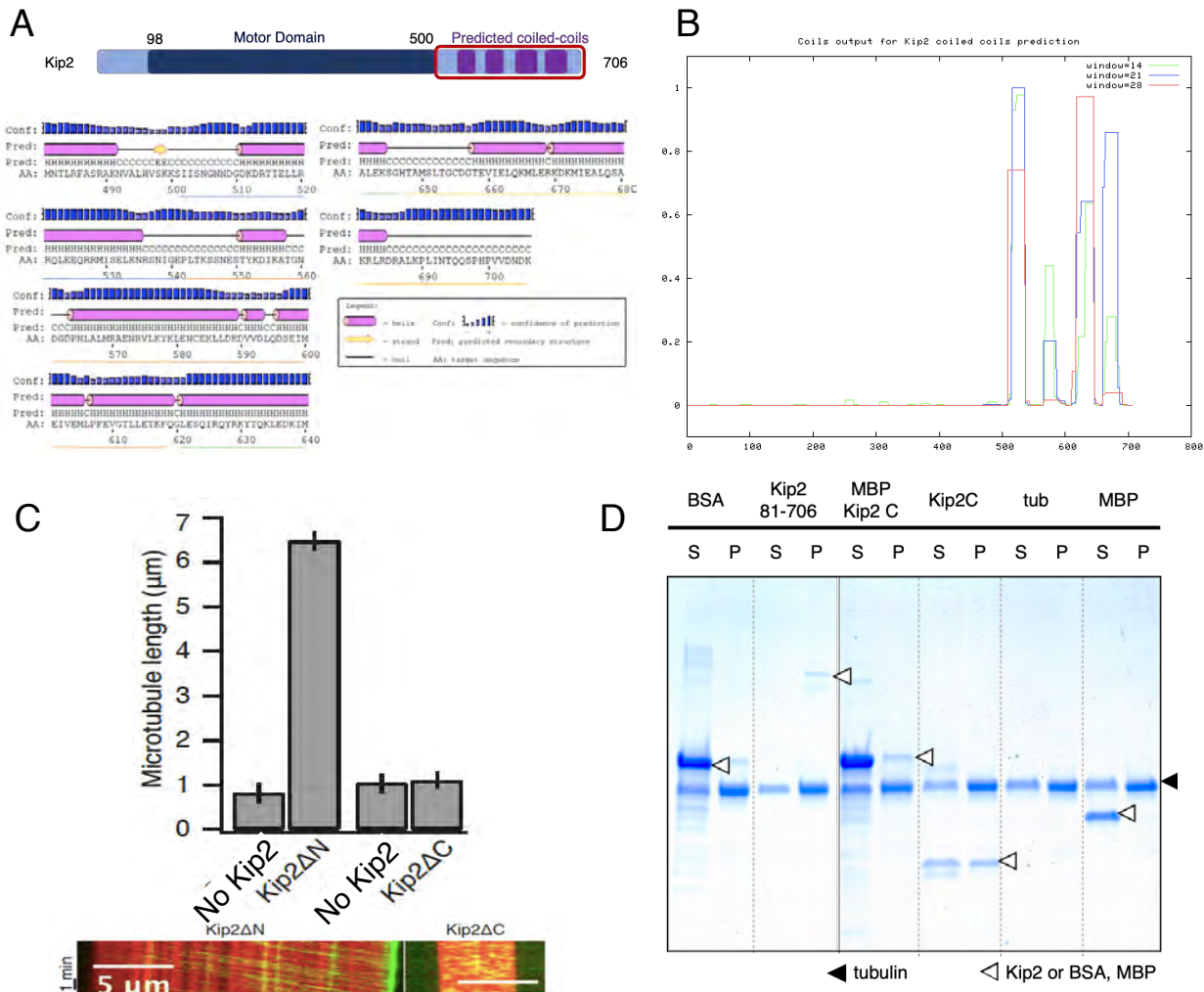


Figure 10-4 Structure Predictions of Kip2C and its role in microtubule polymerization

(A) Structure prediction of Kip2C indicates that it contains multiple helices. The software used is PSIPRED. (B) Coiled-coil prediction of Kip2C shows that it contains four coiled-coils. The software used is COILS. (C) Kip2 C-terminus is indispensable for promotion of microtubule length and Kip2 motility, as indicated by the lack of increase in microtubule growth and no Kip2 motility in Kip2ΔC, while Kip2 N-terminus is not. Adapted from Anneke Hibbel thesis. (D) Microtubule pelleting assay shows that Kip2C is binding to microtubules, with BSA as a negative control, and Kip2 81-706 as a positive control. Black arrowhead indicates tubulins, while white arrowhead indicates either Kip2, BSA, or MBP. S, supernatant; P, pellet.

2.5 Kip2 C-terminus does not affect microtubule dynamics

To confirm the effect of Kip2 C-terminus (Kip2C) on microtubule dynamics, I performed *in vitro* microtubule dynamic assays with 40 nM Kip2C, in the presence of 1 mM ATP and 12 μM bovine tubulin, using the full-length Kip2 (Kip2FL) as a control.

Addition of Kip2C did not affect the average microtubule length, it is comparable to without Kip2, $4.93 \pm 1.35 \mu\text{m}$ without Kip2 (control, 0 nM Kip2) and $4.40 \pm 1.09 \mu\text{m}$ at 40 nM Kip2C, while it is $15.07 \pm 4.16 \mu\text{m}$ at 40 nM Kip2FL. (**Figure 10-5 A**). The mean length of the freshly polymerized microtubules was measured ten minutes after addition of Kip2 and tubulin to the surface-bound microtubule seeds. Note that with high concentrations of Kip2FL, there was no catastrophe so the microtubules grew extensively long and are frequently curving and bending out of the TIRF field, so it became increasingly difficult to measure microtubule length.

Next, to characterize the effect of Kip2C on microtubule dynamics, the parameters of dynamic instability were characterized. I measured the growth rate, shrinkage rate, and catastrophe frequency of microtubules with 40 nM Kip2C, in the presence of 1 mM ATP and 12 μM bovine tubulin, using the full-length Kip2 (Kip2FL) as a control. In **Figure 10-5 B**, I can see that the microtubule growth rate was not affected, $0.39 \pm 0.08 \mu\text{m}/\text{min}$ without Kip2 and $0.32 \pm 0.08 \mu\text{m}/\text{min}$ at 40 nM Kip2C, while it is $0.82 \pm 0.09 \mu\text{m}/\text{min}$ at 40 nM Kip2FL.

To quantify the effect of Kip2C on catastrophe frequency, the total number of catastrophes observed per experimental condition was divided by the total duration of microtubule growth of all microtubules in that experimental condition. Microtubule catastrophe frequency was not affected, 0.208 per minute without Kip2 and 0.208 per minute at 40 nM Kip2C, while at <0.005 per minute at 40 nM Kip2FL (**Figure 10-5 C**).

Lastly, microtubule shrinkage rate was quantified from the slope of microtubules that experienced catastrophe, for all microtubules per experimental condition. 40nM

Kip2C did not affect microtubule shrinkage rate (**Figure 10-5 D**). At 40 nM Kip2FL, catastrophe events were too rare to reliably quantify microtubule shrinkage velocity. In summary, microtubules shrink at a rate of $\sim 6\text{-}8\ \mu\text{m}/\text{min}$, regardless of whether Kip2 is present in the assay.

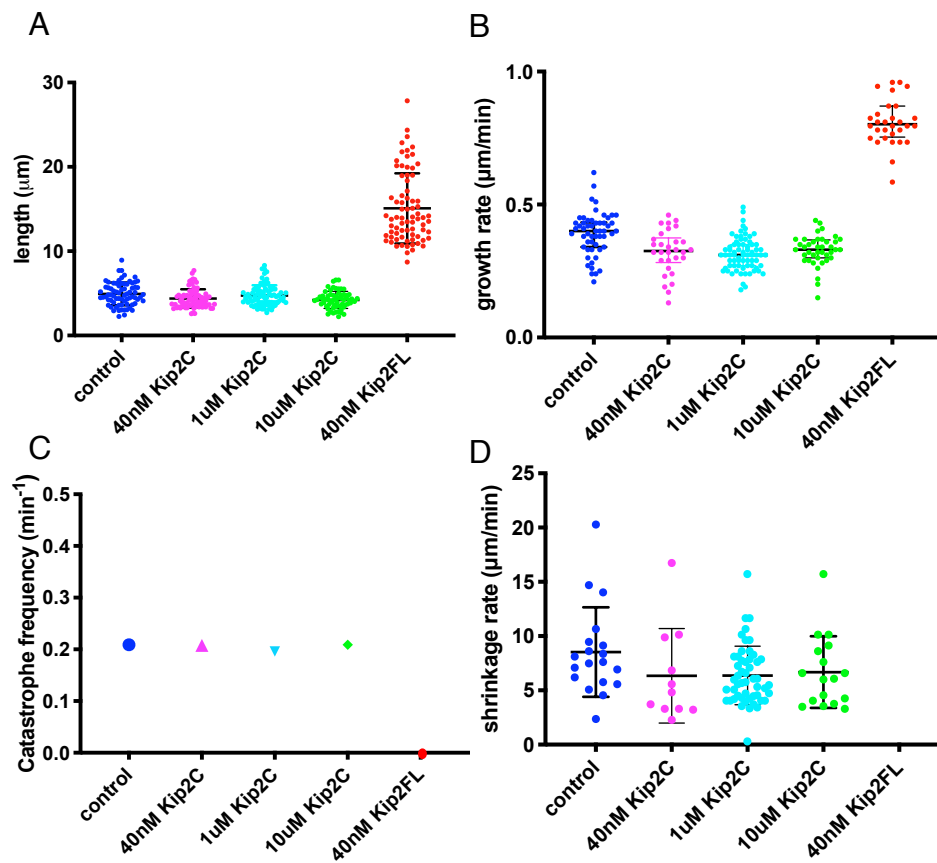


Figure 10-5 Kip2C does not affect microtubule dynamics, even at very high concentrations

(A) Kip2C does not affect the length of microtubules. (B) Kip2C does not increase the growth rate of microtubules. (C) Kip2C does not reduce the catastrophe frequency of microtubules. (D) Kip2C has no effect on the shrinkage rate of microtubules

2.6 High concentration of Kip2 C-terminus still does not have effect on microtubule dynamics

Previously, it was found that Kip2 requires ATP to promote microtubule growth [251]. In 1 mM ATP, Kip2 can increase the microtubule length, and also promote growth rate and reduce catastrophe frequency. On the contrary, no effect was seen in 1 mM AMPPNP. Since Kip2 exerts effect on the microtubule plus-end, it requires motility for it to transport along the microtubule to reach the plus-end. ATP hydrolysis is at least needed for processive motility to localize to the microtubule plus-end. Once at the plus-end, Kip2 may promote microtubule growth without consuming energy, like XMAP215 [173]. Therefore, I reasoned that it could be not enough Kip2C is landing on the microtubule plus-end for it to have effect. As a result, I tested higher concentration of Kip2C, up to 10 μ M Kip2C.

To confirm the effect of higher concentration of Kip2C on microtubule dynamics, I performed *in vitro* microtubule dynamic assays in the presence of 1 mM ATP and 12 μ M bovine tubulin, using the full-length Kip2 (Kip2FL) as a control. Addition of high concentration of Kip2C did not affect the average microtubule length, it is comparable to without Kip2, 4.93 ± 1.35 μ m without Kip2 (control, 0 nM Kip2) and 4.74 ± 1.21 μ m at 1 μ M Kip2C, and 4.21 ± 1.01 μ m at 10 μ M Kip2C. (**Figure 10-5 A**).

Next, I measured the growth rate, shrinkage rate, and catastrophe frequency of microtubules with high concentration of Kip2C, in the presence of 1 mM ATP and 12 μ M bovine tubulin, using the full-length Kip2 (Kip2FL) as a control. In **Figure 10-5 B.**, I can see that the microtubule growth rate was not affected, 0.39 ± 0.08 μ m/min without Kip2

and 0.31 ± 0.06 $\mu\text{m}/\text{min}$ at $1\mu\text{M}$ Kip2C, while it is 0.33 ± 0.05 $\mu\text{m}/\text{min}$ at $1\mu\text{M}$ Kip2C. Microtubule catastrophe frequency was also not affected, 0.208 per minute without Kip2 and 0.196 per minute at $1\mu\text{M}$ Kip2C, and at 0.235 per minute at $10\mu\text{M}$ Kip2C (**Figure 10-5 C**). Similarly, higher concentration of Kip2C did not affect microtubule shrinkage rate (**Figure 10-5 D**). At 40 nM Kip2FL, catastrophe events were too rare to reliably quantify microtubule shrinkage velocity. In summary, microtubule shrink at a rate of ~ 6 $\mu\text{m}/\text{min}$, regardless of whether Kip2 is present in the assay.

To sum up, *in vitro*, Kip2C alone does not affect the average microtubule length, the growth rate, and the catastrophe frequency, without affecting the shrinkage rate.

2.6 Kip2MC1 affects microtubule dynamics by reducing catastrophe frequency

Kip2 C-terminus alone did not have effect on microtubule dynamics, so I rationalized that the motor domain is still needed for end-directed motility, and possibly even for polymerase activity. Therefore, I constructed a minimal dimerization construct of Kip2 that has motility. It contains the motor domain with the first predicted coiled-coil in the C-terminus, and will be referred to as Kip2MC1.

To observe the effect of Kip2MC1 on microtubule dynamics, I started with the *in vitro* microtubule dynamic assays with 40 nM Kip2MC1, in the presence of 1 mM ATP and $12\mu\text{M}$ bovine tubulin. Addition of Kip2MC1 mildly increased the average microtubule length from 3.43 ± 0.21 μm without Kip2 (control, 0 nM Kip2) to 5.88 ± 0.33 μm at 40 nM Kip2MC1, as compared to 8.65 ± 1.30 μm at 40 nM Kip2FL. (**Figure 10-6 A**). The mean length of the freshly polymerized microtubules was measured ten minutes after addition

of Kip2 and tubulin to the surface-bound microtubule seeds. Microtubule growth rate was also mildly increased from 0.23 ± 0.07 $\mu\text{m}/\text{min}$ without Kip2 to 0.32 ± 0.06 $\mu\text{m}/\text{min}$ at 40 nM Kip2MC1, compared to 0.87 ± 0.07 $\mu\text{m}/\text{min}$ at 40 nM Kip2FL (**Figure 10-6 B**).

On the other hand, microtubule catastrophe frequency was strongly decreased from 0.19 per minute without Kip2, to <0.05 per minute at 40 nM Kip2MC1, compared to <0.005 per minute at 40 nM Kip2FL (**Figure 10-6 C**). The microtubule shrinkage rate for control (without Kip2) is about 6 $\mu\text{m}/\text{min}$, but the shrinkage rate at 40 nM Kip2MC1 and at 40 nM Kip2FL is hard to measure, as catastrophe events were too rare to reliably quantify microtubule shrinkage velocity.

Interestingly, when I increased the concentration of Kip2MC1, it enhanced the effect on microtubules. At 100 nM Kip2MC1, the average microtubule length increased to 5.88 ± 0.33 μm (**Figure 10-6 A**). The microtubule growth rate was increased to 0.42 ± 0.07 $\mu\text{m}/\text{min}$ at 100 nM Kip2MC1 (**Figure 10-6 B**). Microtubule catastrophe frequency was strongly decreased from 0.19 ± 0.04 per minute without Kip2, to <0.005 per minute at 100 nM Kip2MC1 (**Figure 10-6 C**).

To sum up, Kip2MC1 mildly increases the average microtubule length and growth rate while strongly reduces the catastrophe frequency, without affecting the shrinkage rate *in vitro*.

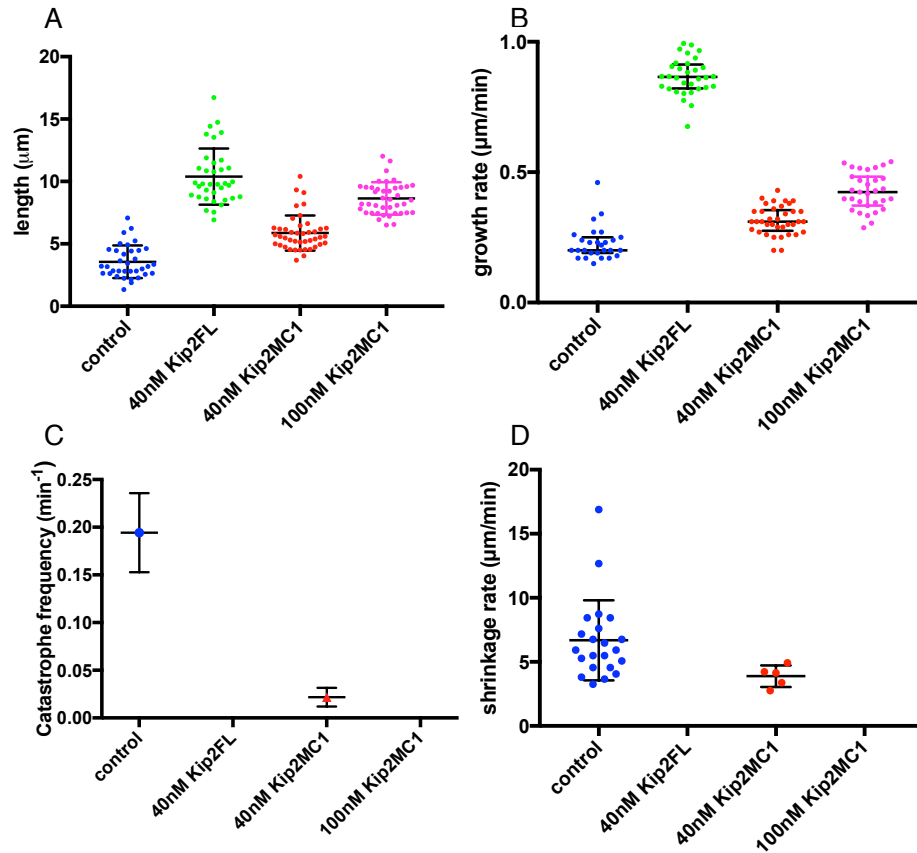


Figure 10-6 Kip2MC1 affects microtubule dynamics by reducing catastrophe frequency

(A) Kip2MC1 increases the length of microtubules moderately. (B) Kip2MC1 increases the growth rate of microtubules moderately. (C) Kip2MC1 strongly reduces the catastrophe frequency of microtubules. (D) Kip2MC1 has no effect on the shrinkage rate of microtubules.

2.7 Kip2MC1 lowers the GTP tubulin off-rate constant

Kip2MC1 particularly lowered the catastrophe frequency, therefore, I was curious to see if it does this by affecting the GTP-tubulin dissociation rate. To test whether Kip2MC1 influences the GTP-tubulin dissociation rate, I measured the microtubule shrinkage rate of GMPCPP-stabilized microtubules, incubated without or 40 nM Kip2MC1, using 40 nM Kip2FL as a control. This experiment is done without addition of free tubulin. The rationale is that the spontaneous depolymerization of GMPCPP-stabilized microtubules mimics the GTP-tubulin off-rate of growing microtubules. In the presence of

ATP, 40 nM Kip2FL decreased the shrinkage rate of GMPCPP-stabilized microtubules from around 0.007 $\mu\text{m}/\text{min}$ without Kip2 to around 0.002 $\mu\text{m}/\text{min}$ at 40 nM Kip2FL (**Figure 10-7**). Kip2MC1 has an intermediate effect, the shrinkage rate was around 0.005 $\mu\text{m}/\text{min}$.

Thus, assuming that GMPCPP-tubulin is a good analog for GTP-tubulin, this result suggests that Kip2FL decreases the GTP-tubulin dissociation rate up to 3-fold in the absence of free tubulin.

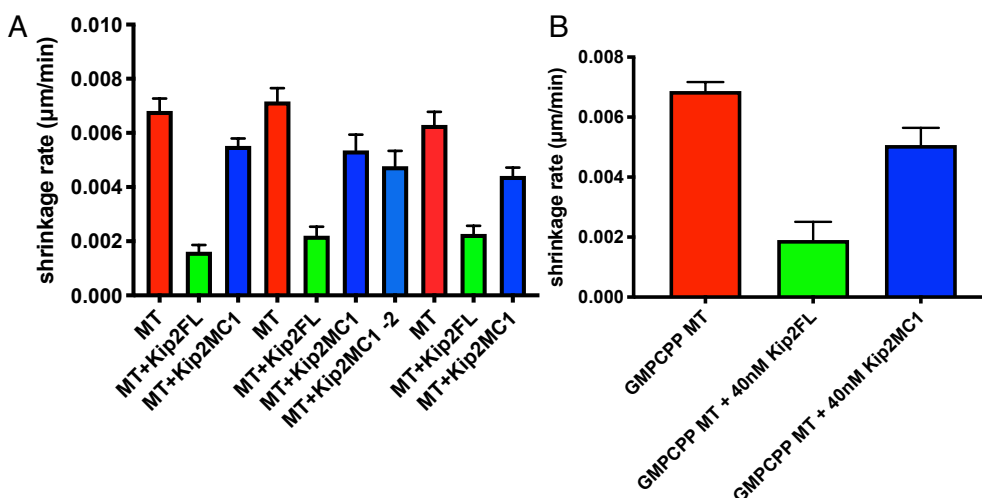


Figure 10-7 Depolymerization of GMPCPP-stabilized microtubules by Kip2FL and Kip2MC1

(A) All data sets of microtubule shrinkage rates of GMPCPP-stabilized microtubules in 1 mM ATP without free tubulin. Shrinkage rates were measured in the absence (MT) and in the presence of 40 nM Kip2FL or Kip2MC1. Both Kip2FL and Kip2MC1 lowers the shrinkage rate of GMPCPP-stabilized microtubules in ATP, to a different extent. (B) The average microtubule shrinkage rate of all data sets.

3 Single molecule motility assays

3.1 A single-molecule motility assay to study biophysical properties of Kip2

Kip2 has a highly conserved kinesin motor domain [206, 213, 229] and can processively translocate along microtubules to the plus-end, where it affects the microtubule dynamics [241, 251].

To further investigate how Kip2 could affect microtubule plus-end dynamics, its biophysical properties were measured in single-molecule motility assays (**Figure 11-1**). To ensure single-molecule Kip2 concentrations, typically around 1 nM Kip2 constructs were added to surface-bound GMPCPP-stabilized microtubules, without free tubulin in solution. Stabilized microtubules were imaged using EPI-fluorescence, whereas single Kip2-eGFP/RFP molecules were imaged using TIRF microscopy at a frame rate of 0.5 Hz, or by continuous streaming at ~10 Hz.

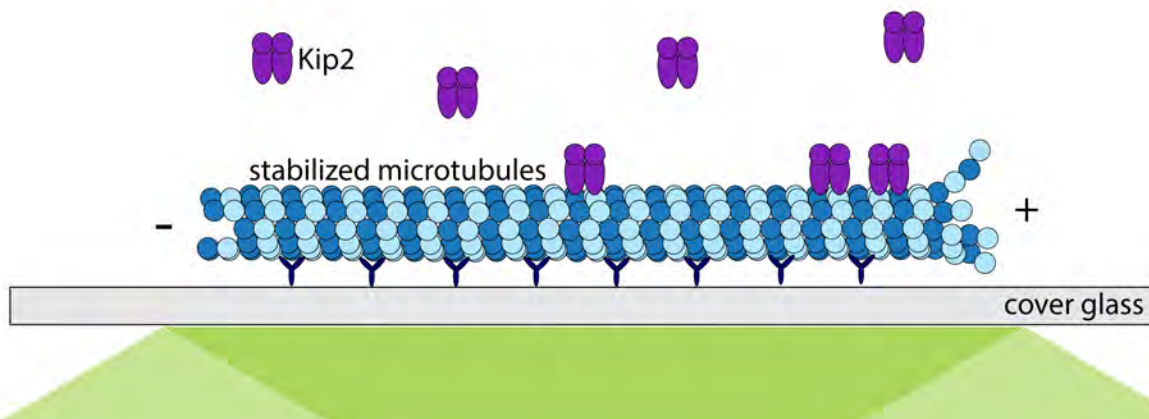


Figure 11-1 Schematic of the single-molecule motility assay.

Schematic of the experimental design. GMPCPP-stabilized microtubules are fixed to the surface of the cover glass with antibodies, and Kip2 are added in without addition of free tubulins.

3.2 Full-length Kip2 is a highly processive motor that dwells at microtubule plus-ends

To study the behavior of Kip2 on stabilized microtubules, I first started with reconstituting the system of full-length Kip2 motility assay, using rat kinesin-1 rK430 as a control. I created kymographs from the single-molecule motility assays and confirmed that in 1 mM ATP, Kip2^{FL}-eGFP molecules associated with GMPCPP-stabilized microtubule lattices and walked processively towards the microtubule plus-end (**Figure 11-2 A**) at a

velocity of $5.0 \pm 0.9 \mu\text{m}/\text{min}$ at 28°C (mean \pm SD, $n = 674$). On the other hand, rK430 translocates at $1.0 \pm 0.1 \mu\text{m}/\text{s}$ on the microtubule (**Figure 11-2 B**) [260]. These data are consistent with the published literature. To sum up, I have successfully reconstituted the Kip2 motility system and confirmed that Kip2 is a processive kinesin that uses its ATP-hydrolyzing motor domain to translocate at a velocity of $5 \mu\text{m}/\text{min}$, which is one order of magnitude slower than the canonical vesicle transporting kinesin-1 [261].

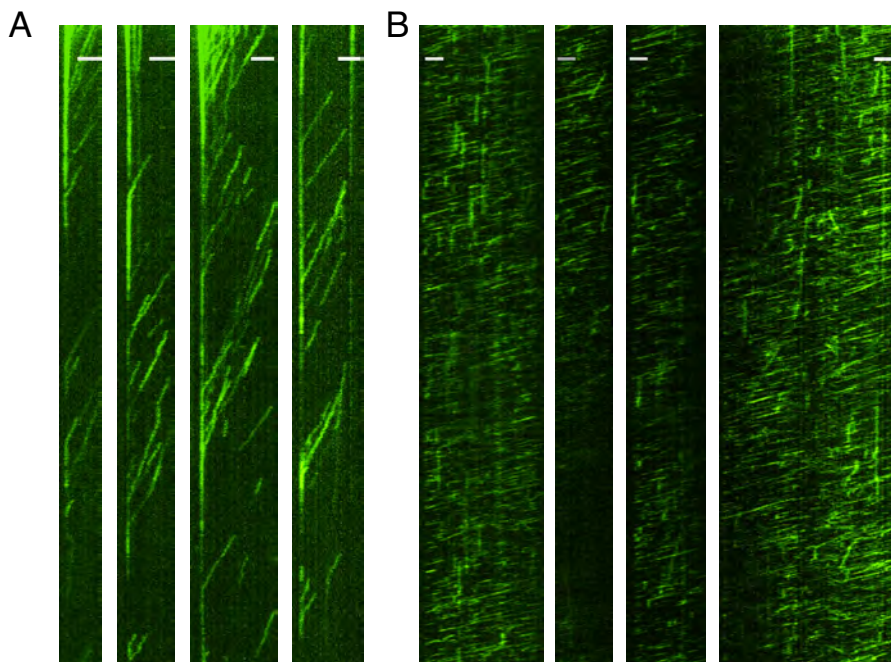


Figure 11-2 Full-length Kip2 is a highly processive motor that dwells at microtubule plus-ends
 (A) In 1 mM ATP, Kip2FL walks processively towards the microtubule plus-end at a velocity of $5.0 \pm 0.9 \mu\text{m}/\text{min}$. Kip2 is also dwelling at the microtubule plus-end. (B) In 1 mM ATP, rK430 translocates at $1.0 \pm 0.1 \mu\text{m}/\text{s}$ on the microtubules. Scale bar, $2 \mu\text{m}$.

3.3 Kip2MC1 has comparable velocity to full-length Kip2

To examine the velocity of Kip2MC1, I created kymographs from the single-molecule motility assays, and measured the velocity of Kip2MC1 on GMPCPP-stabilized microtubules. In 1 mM ATP, Kip2MC1-RFP molecules walked processively towards the microtubule plus-end (**Figure 11-3**) at a velocity of $5.0 \pm 0.9 \mu\text{m}/\text{min}$ at 28°

C (mean \pm SD, n = 674). The velocity of Kip2MC1 is comparable to full-length Kip2. In summary, Kip2MC1 is also a processive kinesin that uses its ATP-hydrolyzing motor domain to translocate at a velocity of 5 $\mu\text{m}/\text{min}$.

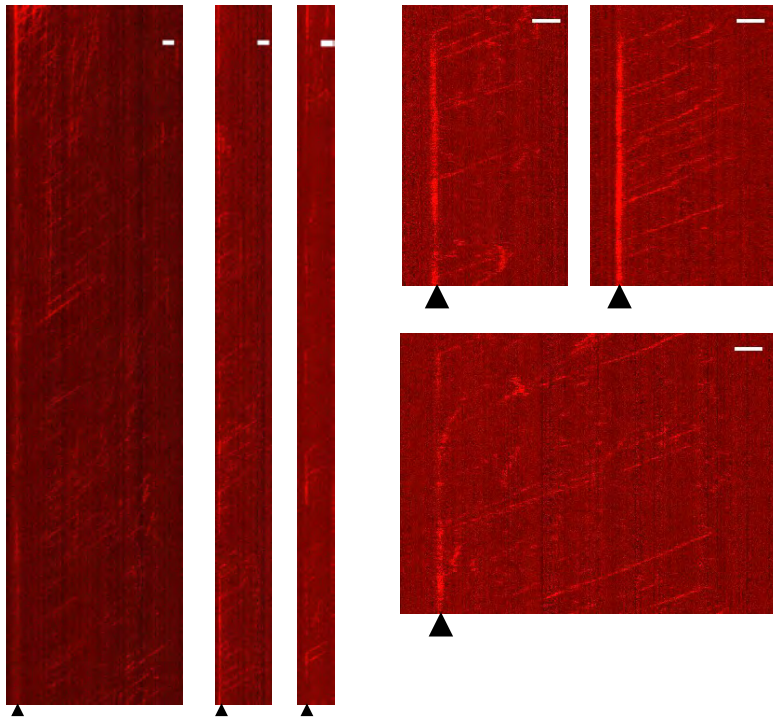


Figure 11-3 Kip2MC1 is also a processive motor that dwells at microtubule plus-end
 In 1 mM ATP, Kip2MC1-RFP molecules walked processively towards the microtubule plus-end at a velocity of $5.0 \pm 0.9 \mu\text{m}/\text{min}$, similar to the full-length Kip2. Black arrowhead indicates the dwelling behavior of Kip2MC1. Scale bar, 1 μm .

4 Visualization of the Kip2-microtubule complex using electron microscopy

In order to study Kip2 interaction with microtubules, especially the effect of Kip2 on the ends of microtubules, I decided to use electron microscopy to try to capture the structure of Kip2 with microtubules. As a positive control, I used the rat kinesin-1 rK430 protein, which has previously been shown to be decorating the microtubules, and the structure of its motor domain binding to microtubules/tubulins has been solved [262, 263] [PDB 3J8X; 4HNA].

Using negative-staining EM, I was able to obtain very nice and straight GMPCPP stabilized microtubules (**Figure 12-1 A**), and the protofilaments can be seen very clearly. In the positive control rK430 + MT, I was able to see the decoration of rK430 on microtubules (**Figure 12-1 B**). For examining Kip2 interaction with microtubules, I first tried loading the microtubules onto the grids first, and then load on the Kip2 proteins. This method gives very clean backgrounds, and less microtubule bundling. However, it seems that not enough Kip2 proteins are loaded onto the grid (**Figure 12-1 C & D**), possibly due to not enough Kip2 concentration (~200 nM), or not enough incubating time (~1 min). Therefore, as a second attempt, I tried mixing of Kip2 with microtubules first, in the presence of AMPPNP, incubate for 30 min, and then load the mixture onto grids. I took several images, and observed that Kip2FL and Kip2MC1 may be interacting with the microtubules (**Figure 12-1 E & F**). But because of the high concentration of the proteins (~500 nM – 750 nM), the backgrounds of the grids are high. I am working on optimizing the method and the concentration of Kip2 proteins so that I can get Kip2 decoration on the microtubules without noisy backgrounds.

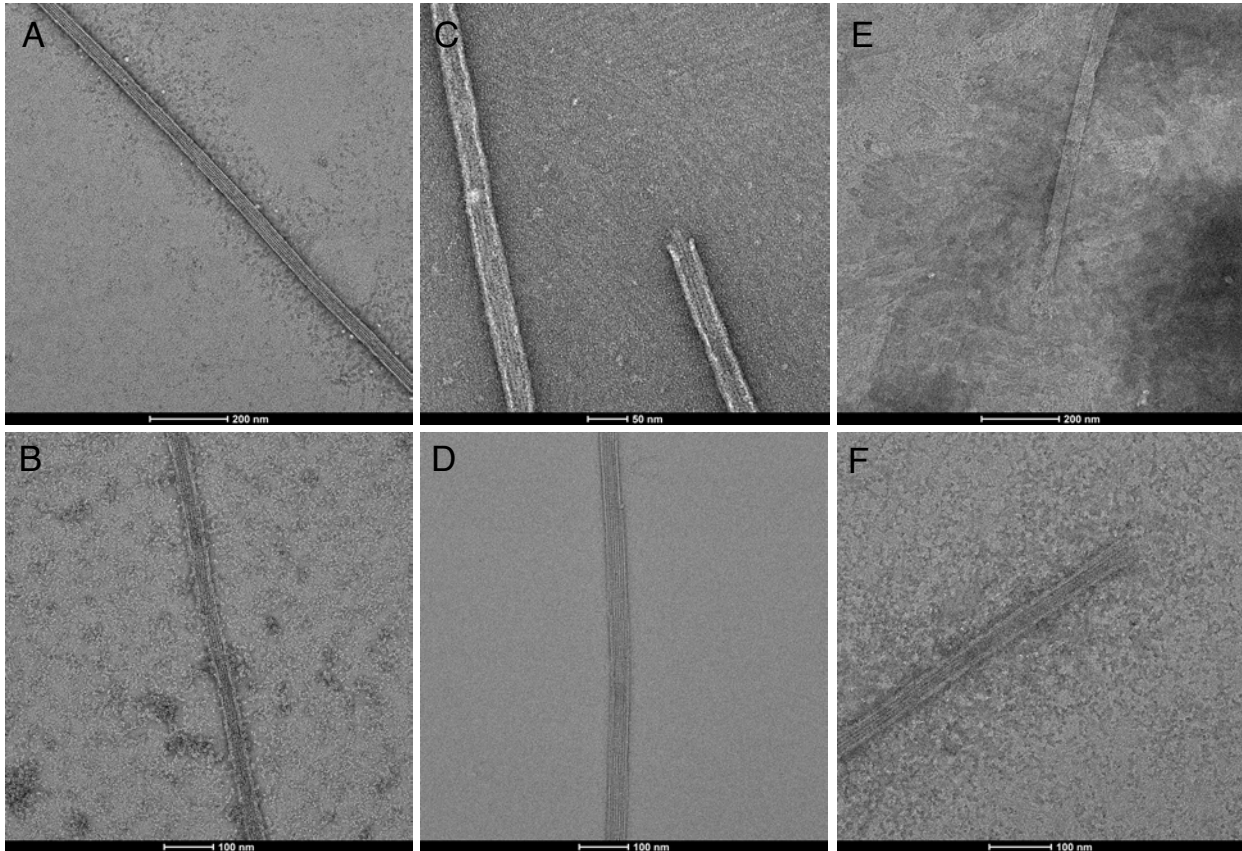


Figure 12-1 Negative-staining EM images of Kip2 proteins with microtubules

(A) GMPCPP-stabilized microtubules alone. (B) GMPCPP-stabilized microtubules with kinesin-1 rK430. (C) & (D) First attempt of GMPCPP-stabilized microtubules with Kip2FL & Kip2MC1, respectively. (E) & (F) Second attempt of GMPCPP-stabilized microtubules with Kip2FL & Kip2MC1, respectively.

5 Discussion and Future Direction

5.1 Confirming that Kip2 promotes microtubule growth *in vitro* at physiologically relevant protein concentrations without accessory proteins

I have performed *in vitro* reconstitution microtubule dynamics experiments of full-length Kip2 and confirmed that Kip2 regulates microtubule dynamics as a polymerase and anti-catastrophe factor in the absence of accessory proteins [251]. The concentration of Kip2 used is 20 nM and 40 nM, which is comparable to the concentration of Kip2 in budding yeast is ≈ 25 nM [264]. Therefore, the effects observed are physiologically relevant.

5.2 Kip2 C-terminus alone does not have effect on microtubule dynamics

Kip2 was shown to promote microtubule growth by enhancing the growth rate and reducing the catastrophe frequency [251], and it might be functioning as a polymerase, namely, processively adding tubulins to the growing microtubule plus-end. To test this hypothesis, I examined the sequences of Kip2 carefully, and decided to look into the C-terminus of Kip2. The reason is that, firstly, I found that it contains positive charges that could potentially interact with the negatively charged tubulin tail. Second, structural prediction showed that it has multiple helices and four coiled-coils (**Figure 10-4 A & B**), which might be critical for dimerization and/or interaction sites for cargo or adaptor proteins.

However, when I first tried with 40 nM Kip2C, I did not observe any effect on microtubule dynamics - the length, growth rate, catastrophe frequency, and shrinkage rate are all similar to the control (without Kip2). To check if it is due to not enough Kip2C landing on the microtubule plus-end for it to exert effect, I decided to use very high concentration of Kip2C. This will ensure that there are enough Kip2C landing on the microtubule plus-end. But increasing the concentration of Kip2C did not show any effect on microtubule dynamics.

The Kip2 C-terminus is critical for Kip2 motility, because it has the dimerization domain which was needed for dimerization and translocation along the microtubule, and it was previously found that Kip2 Δ C has no motility. But besides the dimerization, I thought the C-terminus might also contain tubulin/microtubule binding site(s), so it could

be functioning in a mechanism similar to the Stu2p/XMAP215/Dis family, a processive polymerase. These proteins use $\alpha\beta$ -tubulin-interacting TOG (tumor overexpressed gene) domains to promote microtubule growth. Yeast Stu2p has two TOG domains, one of them anchors to the microtubule lattice, while the other TOG can distinguish between unpolymerized and polymerized forms of $\alpha\beta$ -tubulin and bind to the curved form to catalyzes their addition into the microtubule [265]. I thought the Kip2 C-terminus could also have this kind of stabilizing effect on microtubules, where it is still able to dimerize, with part of them anchoring to the microtubule lattice while the coiled-coils at the very C-terminus can bind to and add tubulin to the microtubule end. Apparently, Kip2C did not have similar effects.

As a result, I reasoned that possibly Kip2 still requires the motor domain for end-directed motility and possibly polymerase activity. This is consistent with published literature, that the effect of Kip2 on microtubule growth promotion requires ATP hydrolysis [251]. It is found that in AMPPNP, there are no increase in length nor growth rate, and no reduction in catastrophe frequency. Therefore, unlike XMAP215, Kip2 does not passively promote microtubule growth. XMAP215 is a processive polymerase that diffuses along the microtubule, and can add multiple tubulin dimers once at the microtubule end without consuming energy. These results demonstrate that the ATP-hydrolyzing motor domain of Kip2 plays a key role in modulating microtubule dynamics.

5.3 Kip2MC1 is the minimal motility construct that has comparable velocity to Kip2FL

Because Kip2 C-terminus alone (Kip2C) does not have effect on microtubule dynamics, I decided to look at the effect of motor domain. I constructed the minimal motility construct Kip2MC1, which contains the motor domain and only the first coiled-coil for dimerization.

I was interested in testing if Kip2MC1 has motility, and if so, how does the velocity of Kip2MC1 compare to the full-length Kip2. I discovered that the minimal motility construct Kip2MC1 has similar velocity to Kip2FL, both around 5 $\mu\text{m}/\text{min}$, which is a magnitude slower than the canonical kinesin-1 [266]. Therefore, minimal construct, namely the motor domain alone, is able to account for the motility of Kip2.

5.4 Kip2MC1 affects microtubule dynamics by reducing the catastrophe frequency

Kip2 increases the tubulin on-rate and decreases the tubulin off-rate, which leads to decrease in microtubule catastrophe frequency as predicted [164]. To further pinpoint which part of Kip2 contributes to this effect, I measured the microtubule dynamics of Kip2MC1. I found that Kip2MC1 only increases the length of microtubules moderately. Moreover, it also only increases microtubule growth rate mildly, suggesting that possibly the other domains outside motor and the first coiled-coil of Kip2 contributes to microtubule growth promotion. On the other hand, it strongly reduces the catastrophe frequency, nearly fully recovered the effect of full-length Kip2. These effects are concentration dependent.

I examine this strong decrease in catastrophe frequency but mild increase in growth rate of microtubules further by analyzing the catastrophe frequency k_{cat} . For the catastrophe frequency analysis, it was predicted to be increasing with both the rate of GTP hydrolysis (h) and the GTP-tubulin dissociation rate k_{off} and decreases with the microtubule growth rate $k_{\text{on}} \cdot [\text{Tb}]$ [164]:

$$k_{\text{cat}} \approx 4 \frac{h k_{\text{off}}}{k_{\text{on}} [T]}$$

This comes from a recent theoretical model hypothesizing that the terminal GTP-cap can protect the microtubule plus-end, if the GTP-tubulin dissociation from a protofilament end does not expose GDP-tubulin in the next position.

To obtain GTP-tubulin dissociation rate k_{off} , I measured the microtubule shrinkage rate of GMPCPP-stabilized microtubules, incubated with or without 40 nM Kip2MC1 and Kip2FL (in the absence of free tubulin). The rationale is that the spontaneous depolymerization of GMPCPP-stabilized microtubules mimics the GTP-tubulin dissociation rate k_{off} of growing microtubules.

I found that while the full-length Kip2 (Kip2FL) decreases the shrinkage rate of GMPCPP-stabilized microtubules 3-fold, Kip2MC1 only decreases the shrinkage rate about 2-fold. Therefore, the nearly 10-fold decrease in catastrophe frequency k_{cat} in Kip2MC1 is not fully explained by the reduction in GTP-tubulin dissociation rate k_{off} . Therefore, further experiments are needed to measure the GTP-tubulin association rate k_{on} to see if it can account for the reduction in k_{cat} by Kip2MC1. This can be done by

measuring the growth rate v_g of microtubules under different tubulin concentrations with a fixed amount of Kip2MC1. As the growth rate v_g is defined as

$$v_g = k_{on} [T] - k_{off}$$

we can obtain GTP-tubulin association rate k_{on} from the slope of the line. As Kip2MC1 only increases the growth rate v_g around 1.7-fold, I expect that the k_{on} will not increase a lot. This might be hinting that although Kip2MC1 can account for the great reduction in catastrophe frequency, there are other domains in Kip2 that participates in the microtubule growth promotion.

5.5 Possible mechanisms of how Kip2 affects microtubule dynamics

Without Kip2, tubulin dimers randomly encounter the microtubule plus-end by diffusion. These short-lived interactions often lead to tubulin dimers diffusing away. With Kip2, tubulin dimers are added to the plus-end and microtubule growth are promoted. Some possible mechanisms of how Kip2 affects tubulin binding kinetics are provided:

1. Kip2 can localize to the microtubule plus-end and processively add free tubulins to the growing microtubule
2. Kip2 stabilize an intermediate state of the microtubule
3. Kip2 could increase lateral protofilament interactions.
4. Kip2 could possibly also promote tubulin dimer straightening when incorporating into the microtubule lattice

In general, Kip2 can increase the tubulin on-rate by binding free tubulin dimers from solution, or decrease the tubulin off-rate by stabilizing an intermediate state of the incoming tubulin dimer by enforcing microtubule longitudinal interactions or lateral protofilament interactions. These mechanisms could explain the increase in microtubule growth rate and decrease in catastrophe frequency. I have found that Kip2MC1 can explain the reduction in catastrophe frequency, therefore, it is possible that Kip2 translocates to the end of the microtubule, where one of the motor domains is stabilizing the end, and possibly the other motor domain is reaching out for free tubulin dimers. To elucidate the molecular details of how Kip2 affects microtubule growth, I am in the process of determining the structure of full-length Kip2 and Kip2MC1 with tubulins/microtubules.

5.6 Towards a detailed molecular understanding of the mechanism of Kip2 microtubule growth promotion

To comprehensively understand the mechanism by which Kip2 affects tubulin binding kinetics I started to solve the crystal structure of Kip2 associated with tubulin using X-ray crystallography and to study Kip2 at microtubule plus-ends using cryo-electron microscopy. I have tried out different techniques of incubating the sample on the EM grids, and are optimizing the concentration and incubation time to reduce the background noise on the grid without affecting the binding of Kip2 on microtubules. Hopefully this would give us an idea of how Kip2 is promoting microtubule polymerization.

6 Material and Methods

6.1 Protein expression and purification

N-terminal 6xHis-tagged Kip2 constructs were expressed in *E. coli* BL21 (DE3). Cells were resuspended in BRB20 and lysed using a microfluidizer. Cell debris was clarified by centrifugation at 26,892 X g for 25 min. The Kip2 constructs were purified using first a Ni-NTA affinity column, then through an ion exchange column, and lastly with size-exclusion chromatography Superdex 200 10/300 GL column in final buffer BRB20.

6.2 Tubulin and Microtubule preparation protocols

6.2.1 Purification of bovine brain tubulin

Bovine brain tubulin was purified as described in [259] in joint effort with members of the Howard lab. Final PC tubulin was concentrated prior to cycling using 15 ml spin-filters with a 30 kDa cut-off (Amicon).

6.2.2 Cycling of tubulin

All Bovine tubulin was cycled prior to usage to remove inactive (unpolymerizing) tubulin, free nucleotides in solution and aggregates, as described in [259]. The cycled tubulin concentration was measured by absorbance at 595 nm using Bradford reagent (Biorad) in a spectrophotometer.

6.2.3 Labeling of tubulin

Bovine tubulin was labeled with Alexa Fluor 488 or TAMRA (Invitrogen), as described in [267].

6.2.4 Polymerization of GMPCPP-stabilized microtubules

Reagents used to polymerize GMPCPP-stabilized microtubules are 1mM GMPCPP and 1 mM MgCl₂ in BRB80, with bovine tubulin at a final concentration of 2 μM. Reagents were mixed, incubated on ice for 5 minutes and transferred to 37°C to allow polymerization of microtubules. For dynamic microtubule assays, GMPCPP stabilized microtubules were incubated at 37°C for 20 minutes, while for stabilized microtubule assays, GMPCPP-stabilized microtubules were incubated for 1.5 hours. Subsequently, microtubules were diluted in 350 μL BRB80 at room temperature and centrifuged for 6 minutes using a Beckman airfuge to remove free tubulin. After centrifugation, the supernatant was aspirated and the pellet was resuspended in 200 μL BRB80.

6.3 Microscopy assay protocols

6.3.1 Glass silanization

Glass cover slips sized 22x22 ± 0.005 mm and 18x18 ± 0.005 mm (Menzel-Glaeser) were silanized as described in [253].

6.3.2 Flow cell preparation

Flow cell chambers were made as described in [253], using silanized coverslips but parafilm instead of double-sided scotch. Flow cell channels were prepared at the bench as follows:

1. 20 μ L BRB80 was flown into the flow cells.
2. Anti-rhodamine antibodies (Sigma-Aldrich) diluted 1:50 in BRB80 were flown into the channel and incubated for 10 minutes.
3. The channel was washed with 40 μ L BRB80 to remove unbound antibodies.
4. 20 μ L F127 (Sigma-Aldrich) was flushed in and incubated for 30 minutes to passify the cover glass surface.
5. Channels were washed with 80 μ L BRB80 to remove unbound F127.
6. 20 μ L of stabilized rhodamine-labeled microtubule seeds, diluted 1:10 in BRB80, were perfused into the channel using filter paper and incubated for 10 minutes.
7. The channel was washed 2 times with 20 μ L BRB20 to remove unbound microtubule seeds and to substitute BRB80 for BRB20. Next, the chamber holder was mounted onto the microscope to allow the flow cell channels to heat to 28°C.

6.3.3 Dynamic microtubule assay with bovine tubulin

Dynamic microtubule assays were performed to measure effects of Kip2 on dynamic microtubules grown with labeled porcine tubulin. For dynamic microtubule assays, flow cell channel preparation continued as follows: 20 μ L polymerization buffer including 12 μ M 8% Alexa-488 labeled tubulin and Kip2 or Kip2-eGFP in solution was perfused into the channel. TIRF microscopy time-lapse imaging was started exactly 10 minutes after perfusion of the polymerization buffer.

6.3.4 Single-molecule motility assay

Single-molecule motility assays were performed to measure biophysical properties of fluorescently labeled Kip2 on nondynamic microtubules. For single-molecule motility assays, flow cell channel preparation continued as follows: 20 μ L motility buffer including Kip2-eGFP in solution was perfused into the channel. TIRF microscopy time-lapse imaging was started directly after perfusion of motility buffer into the channel.

6.3.6 TIRF Microscopy

Rhodamine-labeled proteins were excited by EPI-fluorescence using a HBO100 mercury lamp. EGFP-labeled proteins were excited using a 488 nm laser line (Ion Laser Technology). Imaging was performed with an Andor iXon camera on a Zeiss Axiovert 200M microscope with a Zeiss \times 100/1.46 plan apochromat oil objective and standard filter sets. An objective heater (Zeiss) was used to warm the sample to 28 °C.

6.3.7 DIC Microscopy

The set-up used in the DIC microscopy experiments was described in [268].

6.3.8 Image and data analysis

Image analysis was performed by creating kymographs of microtubule growth events and single-molecule motility events in Fiji/ImageJ. Data analysis was performed using Graphpad or Excel software packages.

6.3.9 Statistics and graphics

Statistical analyses were performed using Graphpad, Excel, Fiji/ImageJ and Adobe Illustrator software packages.

Appendix I: Construction of Novel Tubulin Assemblies for Molecular Studies of Microtubule Associated Proteins

1 Introduction

1.1 Microtubule Conformations

Microtubules possess this hallmark property of “dynamic instability”, the frequent switch between growth and shrinkage [160]. Research studies of structural, biochemical, and *in vitro* reconstitution data has advanced the understanding of dynamic instability, the regulation of it by different MAPs, and also the different structures of tubulins/microtubules. Early EM studies showed that $\alpha\beta$ -tubulin could form a diversity of polymers [269], and the first cryo-EM structure of microtubules showed the different structures of the straight and tapered growing ends, versus the curved and peeling outwards shrinking ends [270]. Later, further cryo-EM study showed that the growing end of microtubules could also be curving outward [271]. The first structure of the straight $\alpha\beta$ -tubulin was solved from cryo-electron crystallographic studies of Zn-induced $\alpha\beta$ -tubulin sheets [272-274], while the curved form was solved from X-ray crystallography of the stathmin RB3 and $\alpha\beta$ -tubulin complex [275, 276]. An intermediate conformation was also seen in a cryo-EM study of the GMPCPP-stabilized microtubule [277]. Since then, multiple structural complexes with GTP-bound $\alpha\beta$ -tubulin was solved [265, 278, 279], including those bound with stathmin RB3 [280], DARPin [279], or with the microtubule polymerase Stu2/XMAP215 family TOG domain [170, 281]. These structures reveal the morphology diversity of microtubules, and their different regulation by MAPs (**Table 5**). I am curious to see if I can utilize part of

these MAPs, especially the tubulin sequestering proteins, to reconstruct part of the microtubule for structural studies.

| | Angle Value | PDB id |
|------------------------|-------------|----------------------|
| Microtubule | 1.1° | 3JAK |
| Tubulin–kinesin–DARPin | 9.2° | 4HNA |
| Tubulin–SLD–TTL | 10.5° | 4I4T |
| Tubulin–SLD | 10.6° | 3RYC |
| Tubulin–SLD–DARPin | 10.6° | 4F6R |
| Tubulin–iiH5 | 11.2° | 6GWD |
| Tubulin–kinesin–DARPin | 11.6° | 4LNU |
| Tubulin–DARPin | 11.9° | 4DRX |
| Tubulin–TOG | 12.2° | 4U3J |
| Tubulin–TOG | 13.5° | 4FFB |
| Tubulin–DARPin | 13.5° | 5EYP |
| Tubulin–CPAP–DARPin | 14.4° | 5ITZ |
| Tubulin–kinesin–DARPin | 14.7° | 5MIO |
| Tubulin–iE5 | 18.2° | 6GWC |

Table 5 List of tubulin-MAP structures

These are the complex structures of tubulins with different MAPs, with or without tubulin sequestering proteins, deposited in the Protein Data Bank. The angles between tubulins are indicated. Adapted from [282].

1.2 EM Technology Development of Imaging Microtubules/Tubulins and Challenges

The fast development of cryo-electron microscopy [283] has taken us into a new era of protein structure determination. Microtubules can be captured in solution-like state in cryo-EM [284], and allowed the determination of the protofilaments configurations [285].

To decipher the regulation mechanism of microtubules by various MAPs and motor proteins, two alternative strategies have been utilized to obtain high resolution structures of MAPs bound to tubulins or microtubules: 1) using cryo-EM helical averaging of MAPs decorated on assembled microtubules, and 2) using tubulin sequestering proteins to solve MAP-tubulin complex structures by X-ray crystallography. Combining cryo-EM imaging

with 3D reconstruction, the binding of kinesin motor domains and other MAPs are determined. On this edge, cryo-EM can now reach atomic resolution due to recent advances in technology, but requires MAPs to be uniformly bound to microtubules, which has been difficult to achieve for some MAPs experimentally. It is noteworthy that recently, the improvement in EM detectors [286] as well as software development [287] not only greatly enhanced the resolution of MT-protein complex structures, but are also able to distinguish the subtle differences between α - and β -tubulin (reviewed in [288]).

On the other hand, tubulin-sequestering proteins stably bind to and prevent the polymerization of tubulin, thus allowing for solution-based binding and structural studies of MAP-tubulin complexes. This sequestration is critical to keeping MAP-tubulin complexes homogeneous and soluble when studying MAPs that strongly promote the assembly of microtubules, such as tau. Stathmin RB3 and DARPin D1 (Designed Ankyrin Repeats Protein) are tubulin-sequestering proteins used in structural studies [279, 289], which is further introduced below. However, the current tubulin-sequestering proteins do not support extended tubulin assemblies that are required for binding of many MAPs. Here, I are set out to design a tubulin assembly that contains all the required binding interfaces for the study of different MAPs.

1.3 Tubulin Sequestering Proteins

RB3 and D1 are the two most common tubulin sequestering proteins that can serve as a tool for construction of the soluble pieces of tubulin assemblies. RB3 has an α -helical stathmin-like domain (SLD) that can sequester two tubulin heterodimers in a slightly

curved form [275], while DARPin D1 protein inhibit microtubule assembly by capping the longitudinal interface of β -tubulin and stopping polymerization at the plus end [279]. Crystal structures of tubulins with these tubulin-sequestering proteins have been solved [279, 289] (PDB ID: D1 4DRX, RB3: 3RYH), and the complexes have been used for other biophysical studies [263, 276, 290, 291].

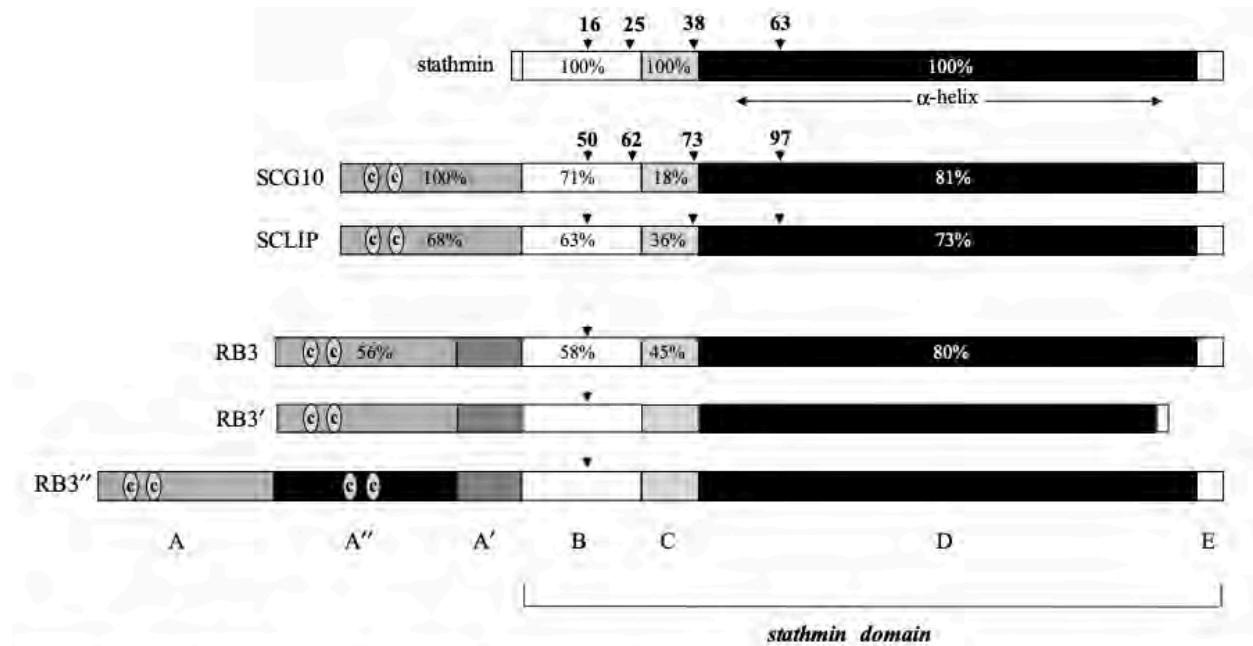
1.3.1 Stathmin RB3

Stathmin, also known as Op18 [292] or p19 [293], is a 17-19 kDa cytoplasmic small regulatory phosphoprotein that is in the neural protein family which includes SCG10, SCLIP, and RB3 (splice variants RB3' and RB3'') [reviewed in [294]]. The stathmin proteins share a highly-conserved stathmin-like domain (SLD) (**Appendix 1-1**), and induces microtubule depolymerization during interphase and cell mitosis [295]. Its effect on microtubules are regulated by phosphorylation [296].

The structure of stathmin contains the N-terminal beta-hairpin domain, which is the regulatory domain that contain four phosphorylation sites [295]. The C-terminus is an alpha-helical coiled-coil structure, and is shown to be interacting with two tubulin heterodimers [275]. Stathmin recognizes the naturally curved formation of tubulin dimers and sequesters it in this curved form by binding along their sides and capping at the α -tubulin end [297].

RB3 protein, a family of the stathmin SLD, was engineered to sequester one to four tubulin heterodimers that can be used as tools for structural studies [289]. The RB3, which sequesters two tubulin heterodimers, are shown to have an affinity of $K_a =$

$1.9 \pm 0.9 \times 10^6 \text{ M}^{-1}$ [297]. The shorted form of RB3 (will be labeled as SRB3, short-RB3, in this thesis), was shown to be binding to a single tubulin heterodimer with affinity $K_d = 1 \text{ nM}$ [289].



Appendix 1-1 Domain organization and sequence similarities of the stathmin family protein.

The stathmin family protein, including stathmin, SCG10, SCLIP, and different splice variants of RB3. The sequence similarity is marked in percentage. Adapted from [295].

1.3.2 DARPin

DARPin proteins (designed ankyrin repeat proteins), are genetically engineered proteins that are mimicking antibodies [298]. They are derived from natural ankyrin repeat proteins, which consists of many 33-amino-acid modules, each forming a structure of a β -turn and two anti-parallel α -helices [299], which are stacked against each other and form right-handed solenoid structure with a continuous hydrophobic core and a large solvent accessible surface. The ankyrin repeat domains usually consists of four to six

repeats, but up to 29 consecutive repeats can be found in a single protein (reviewed in [300]).

To develop binding partners to tubulins, a DARPin library [301] was screened through ribosome display [302, 303]. In this assay, the longitudinal interface of α -tubulin was immobilized to the wells of microtiter plates, thus this screened for binding of DARPins to the exposed β -tubulin. The strongest hit was identified and named D1 [279]. D1 binds to tubulin in 1:1 ratio shown by size exclusion chromatography coupled to multi-angle light-scattering analysis (SEC-MALS), and the binding affinity to GDP-tubulin ($K_d = 120 \pm 10$ nM) was found to be very similar to that of GTP-tubulin ($K_d = 155 \pm 10$ nM) [279]. In the 2.2 Å resolution crystal structure of the tubulin-D1 complex, D1 interacts with only the longitudinal interdimer interfaces of tubulin, namely helices H11 and H6, and loop T5. Although the binding mode is very different from that of RB3-tubulin complex (T2R) [276], both sequestered tubulins in an identical intrinsically curved form. Moreover, D1 inhibited microtubule assembly at the plus-end in a dose-dependent, ATP-independent manner [279].

Tubulin-DARPin complex is a useful tool for studying the interactions of MAPs-tubulin complex. Using this tool, the motor domain of kinesin motor in complex with tubulin was solved and it was shown that ATP hydrolysis causes the motor core subdomain movement and the docking of neck-linker, revealing the structural changes of motor domain in ATP hydrolysis cycle [263, 304].

1.2 End-binding protein EB1

Human end-binding protein EB1, is a highly conserved plus-end tracking protein (+TIP) [189, 191, 256] It is a 35 kDa leucine zipper protein, and contains an positively charged 130 aa N-terminal microtubule binding CH domain (calponin-homology domain) [305, 306], the 130-191 aa unstructured intermediate domain, and the negatively charged C-terminus that has a coiled-coil for dimerization, and an end acidic tail that is a central hub for interaction with other +TIPs [307]. EB1 was first identified in a yeast two-hybrid screen as an interacting partner to the adenomatous polyposis coli (APC) tumor suppressor protein [308]. EB1 has been found in different organisms, including the homologue Bim1 (binding to microtubules 1) in the budding yeast *Saccharomyces cerevisiae* [309], and fission yeast *Schizosaccharomyces pombe* Mal3 homologue [310]. EB1 was shown to increase both microtubule growth and catastrophe frequency [311], and had important roles in regulation of microtubule dynamics, cell mitosis, and cell polarity [312, 313].

EB proteins bind between microtubule protofilaments except at the seam, in the center of four tubulin heterodimers, interacting with the tubulins through electrostatic interactions [314, 315]. EB1 was shown to recognize the GTP-cap at microtubules end [314], and preferentially binds to GMPCPP microtubule lattice compared to GDP lattice [316, 317]. Recently, it was also shown to be recognizing structural disruptions and tapered microtubule ends regardless of the nucleotide state, and the recognition is based on a diffusion-limited binding model that facilitates the tip tracking of EB1 at microtubule

growing ends [318]. Moreover, at high concentrations, EB binding can lead to a partial lattice compaction of a preformed 14-pf GMPCPP-MT [319].

1.3 Tau protein

Tau promotes microtubule polymerization and stabilizes microtubules in the axons, maintaining a microtubule network that is important for normal neuronal growth [320, 321]. Due to alternative splicing, there are six isoforms of tau, each having up to two N-terminal acidic regions (0N to 2N), a proline-rich region (PRR), and either three or four repeats (3R or 4R, R1 to R4) in the microtubule-binding domain (MTBR) [322] (**Appendix 2-8 A**). In neurodegenerative diseases such as Alzheimer's disease, tau is hyper-phosphorylated, causing it to detach from microtubules and form aggregated paired helical filaments (PHF) [323]. Models of the tau microtubule interaction include tau binding to the microtubule outer surface longitudinally along the protofilaments [324], and that tau binds to multiple tubulin dimers, with one proposing that tau can bind a tubulin heterodimer in a U-turn conformation that favors longitudinal assembly with additional tubulin heterodimers, thus providing the straightening force for microtubule polymerization [290]. Importantly, several studies have shown that significant portions of tau become ordered upon microtubule binding, making it amenable to high-resolution structural techniques. Recently, a paper from the Nogales lab have solved the tau structure partially using cryo-EM. In their model, they have reconstructed the four repeats of the MTBR R1 or R2 binding domain of tau, and observed that it is binding along the outside surface of microtubules [325]. Their structure of the MT-tau complexes showed that each binding of

tau repeat is centered on α -tubulin and three tubulin monomers, and adopts an extended conformation that spans both intra- and interdimer interfaces.

1.4 Aim and Scope

This part of my research aims to develop new tools for biochemical and structural studies of the regulation of microtubules by a wide range of MAPs and motor proteins, in particular to decipher the functional interactions between tau and tubulins in regulating the stability of microtubules.

1.4.1 Develop novel tubulin assemblies

Microtubules are key players in essential cellular functions, and are regulated by MAPs. Investigating MAP-microtubule interactions at high resolution will yield important insights into their important functions. However, a key challenge is the lack of suitable, soluble tubulin assemblies for structural studies. Crystallization of MAP-microtubule complexes has been very challenging due to the highly polymerizing/aggregation nature of microtubules. Even with the advancement of electron microscopy, there are still several technical issues limiting the use of the helical reconstruction method, such as the need of uniform decoration of MAPs around microtubules, and the pseudo-helical nature and high heterogeneity of microtubules in morphology. With the design of my tubulin-sequestering proteins, a series of homogeneous, soluble and stable tubulin assemblies can be formed and studied by many well-established biochemical and structural biology methods. Moreover, my tubulin assemblies can capture the different structural features during the microtubule dynamic assembly-disassembly cycle, such as the free tubulin heterodimers

(SRB3-D1), the curved protofilaments at microtubule ends during shrinkage (RB3-D1), and the straight protofilaments encompassing the microtubule lattice during growth (RB3-D1-D1, Nter-RB3-D1-D1, with or without the addition of relaxing linkers). With the design of these tubulin sequestering protein-tubulin complexes, I will be able to obtain homogeneous and stable tubulin assemblies and use both X-ray crystallography and electron microscopy to study their interactions with diverse MAPs.

1.4.2 Study of tau function and mechanism

As an aging population, neurodegenerative diseases affect millions of people worldwide. In 2016, around 47 million people lived with dementia, 22.9 million in Asian countries, and over 9.9 million new cases are reported every year [326]. Alzheimer's Disease is the most common form of dementia, with 35.6 million people worldwide, and this number will grow to 115.4 million by 2050. In the brains of patients with Alzheimer's Disease, tau loses the native interaction with microtubules and forms insoluble neurofibrillary tangles. Therefore, there are growing interests in developing tau-focused therapeutics.

Establishing the interaction of different tau constructs with my newly developed tubulin assemblies will contribute greatly to understanding the roles of tau in cellular function and diseases. First, deciphering the key interactions of tau with tubulin is important, since these residues could also be critical for pathogenic aggregation of tau and may be stabilized in alternative conformations [327]. This suggests that the therapeutic stabilization of the microtubule-bound conformation of tau may be able to delay the pathogenic aggregation and neurotoxicity of tau. Second, the binding difference

between different regions of tau to microtubules will reveal important regulation of microtubule by tau during development, and these regions exist in different tau isoforms. While there is only one tau isoform in the fetal neuron, adult neuron has 6 tau isoforms. The ratio of various tau isoforms is tightly regulated during development [328]. Third, obtaining the structure of tau with different tubulin assemblies is invaluable.

By comparing the conformational changes between tau binding to various forms of tubulin, I can decipher how tau promotes the assembly of microtubules from tubulin heterodimers, thus elucidating the mechanism by which tau promotes microtubule stabilization. Moreover, the structural model will provide a framework to study the physiological roles of the post-translational modifications of Tau, including phosphorylation [329], lysine acetylation [330, 331] or proline isomerization [332], which would be beneficial for developing therapies for neurodegenerative diseases.

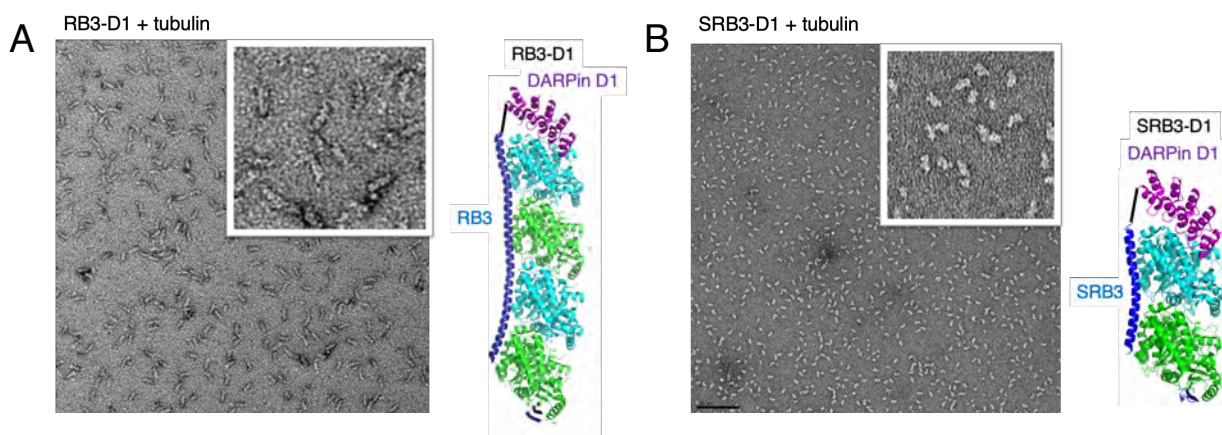
Despite extensive studies, the molecular mechanism of tau remains largely unknown, including the exact number and locations of tau binding sites on α - and β -tubulin monomers, and the mechanism of tau mediated microtubule growth promotion. Therefore, I aim to study the mechanism of tau at the molecular level, by a combination of detailed mapping and high-resolution structural work. Challenges in studying tau include the potentially dynamic nature of the tau-tubulin interaction, the strong polymerization inclination of tubulin in the presence of tau, and potential disordered regions of tau between the ordered regions bound to tubulin. Therefore, I will design stable constructs of tau and tubulin, and resolve the structure with crystallography or cryo-EM to provide a more complete understanding.

2 Construction of Novel Tubulin Assemblies and the Structural Study of Tau

2.1 RB3-D1 and SRB3-D1 forms stable complexes in gel filtration and negative-stain EM

To facilitate the structural studies of MAPs, I have designed a variety of soluble multi-tubulin platforms using the tubulin-sequestering proteins RB3 and DARPin. With these sequestering proteins, I can recreate interfaces found in assembled microtubules in discrete, homogenous, and soluble segments.

I have constructed two RB3-DARPin fusion proteins, termed SRB3-D1 and RB3-D1, that stably sequester either one (SRB3-D1) or two (RB3-D1) tubulin heterodimers and have validated their structures using negative-stain EM (**Appendix 2-2 A&B**). The two tubulin heterodimers sequestered by RB3-D1 are positioned similarly to heterodimers found in microtubule protofilaments, while the single heterodimer sequestered by SRB3-D1 is analogous to free tubulin. All of these multi-tubulin complexes are suitable for both crystallization and cryo-EM structural studies.



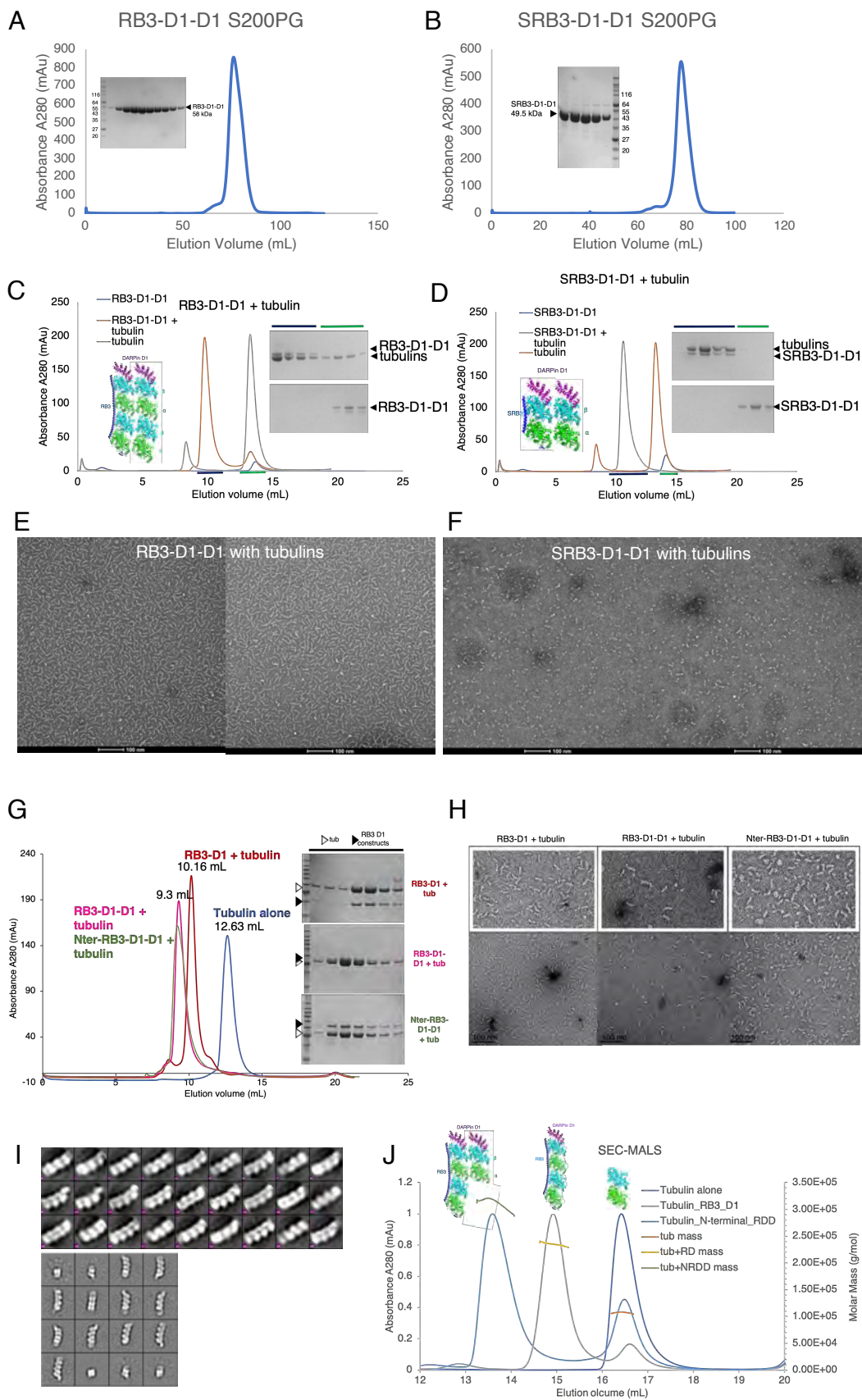
Appendix 2-1 SRB3-D1 & RB3-D1 fusion proteins form stable complexes with tubulins

Negative-staining EM images are on the left, and the cartoon figures are on the right. (A) RB3-D1 form stable complex with two tubulin dimers. (B) SRB3-D1 form stable complex with a single tubulin dimer.

2.2 Fusion of Stathmin with DARPin, the construction of RB3-D1-D1, Nter-RB3-D1-D1 and SRB3-D1-D1

In order to recreate the other interaction interfaces in microtubules, I have fused another DARPin D1 to RB3-D1 and SRB3-D1 (**Appendix 2-3 A&B**). These proteins can be purified pretty well, and form stable binding interactions with tubulins. In the size exclusion chromatography, they form larger complexes and shift significantly to the left as compared to the single-row tubulin assembly, RB3-D1 + tubulin, indicating that they are forming larger complexes (**Appendix 2-3 C&D**). However, under negative-stain EM, it is hard to distinguish the individual two-row of tubulins (**Appendix 2-3 E&F**).

I suspected that tubulin sequestering fusion proteins might not be tightly holding the two rows of tubulins enough, therefore, I added in a stathmin RB3 β -hairpin into the construct, to cap another tubulin. The binding showed that it is shifting to a larger volume, as compared to the RB3-D1 (**Appendix 2-3 G**). To confirm the complex, negative-staining EM and 2D classification was performed, and it seems that they are not forming these two-row tubulin assemblies (**Appendix 2-3 H&I**). Furthermore, to determine the stoichiometry of the binding of tubulins per Nter-RB3-D1-D1, size exclusion chromatography coupled to multi-angle light-scattering analysis (SEC-MALS) was performed. It can be seen that the N-ter-RB3-D1-D1 with tubulin complex (tub+NRDD) is around 330 kDa, meaning that there is possibly only three (not four) tubulin heterodimers in the complex (**Appendix 2-3 J**).

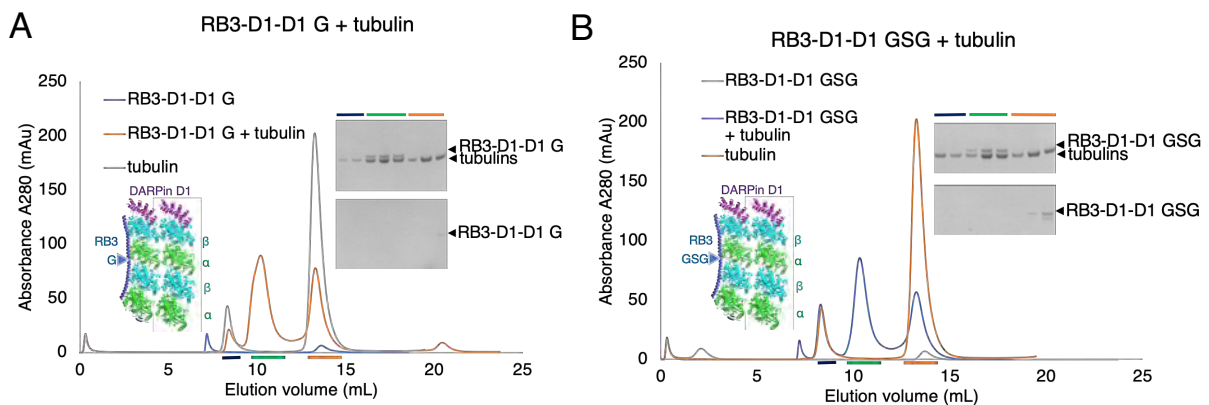


Appendix 2-2 RB3-D1-D1, SRB3-D1-D1, and Nter-RB3-D1-D1 form stable complexes with tubulins

(A&B) The purification of RB3-D1-D1 and SRB3-D1-D1 with S200 size exclusion chromatography showed that the protein is pure and homogeneous, yielding a single and nice peak. (C&D) Binding of RB3-D1-D1 or SRB3-D1-D1 with tubulins showed that the mixture is forming a stable complex, which is shifting to a larger molecular weight. (E&F) Negative-staining EM images of RB3-D1-D1 or SRB3-D1-D1 with tubulins. (G) Binding assays of tubulins with different RB3/D1 fusion constructs. (H) Negative-staining EM images of RB3/D1 fusion proteins with tubulins. (I) 2D classification of EM images of Nter-RB3-D1-D1 with tubulins. (J) Size exclusion chromatography coupled with multiangle light scattering (SEC-MALS) to determine the molecular weight of the tubulin complexes. Tubulin alone or tubulin with RB3-D1 are used as controls.

2.3 Adding flexible linkers into RB3-D1-D1 did not improve the tubulin assembly

Because the binding of RB3 to tubulins are modular [289], so I thought that adding in flexible linkers in between the modular tubulin binding sites of RB3 could help relax the curvature and help zip up the tubulin two rows. I have expressed and purified the tubulin sequestering constructs, and performed SEC binding assay. The addition of flexible linkers did not improve the formation of the two-row tubulin assembly, on the contrary, it actually prevented the formation of larger assemblies, as demonstrated by the lincreased amount of free tubulins (**Appendix 2-4 A&B**).

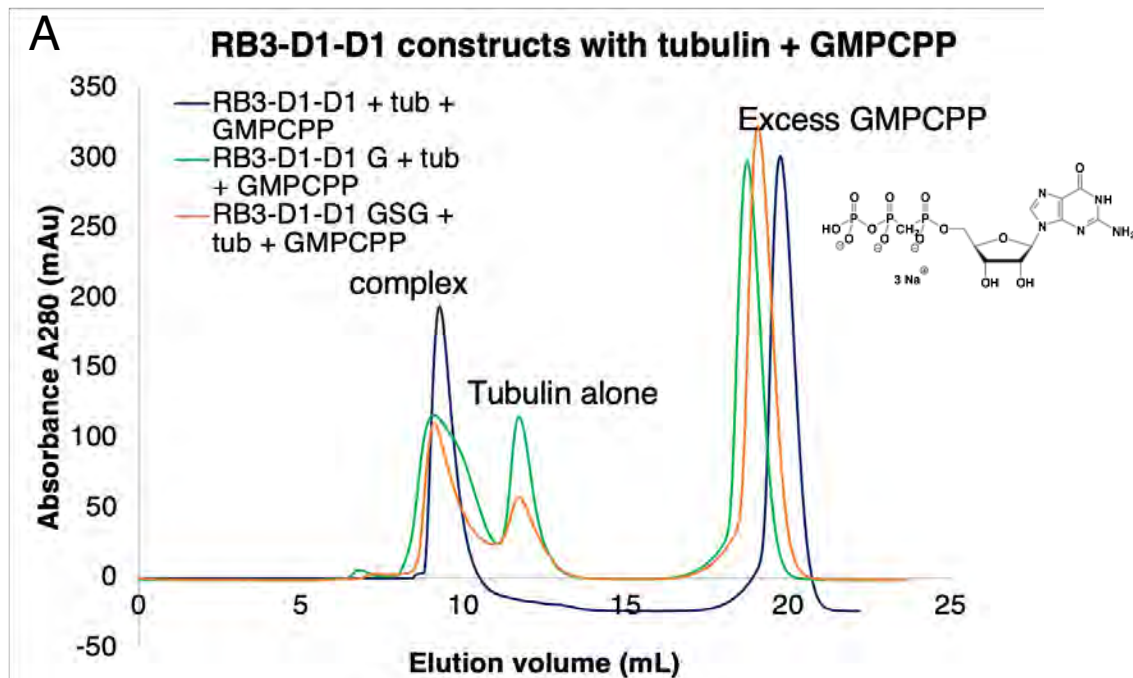


Appendix 2-3 Adding in linkers to help relax the curvature of RB3

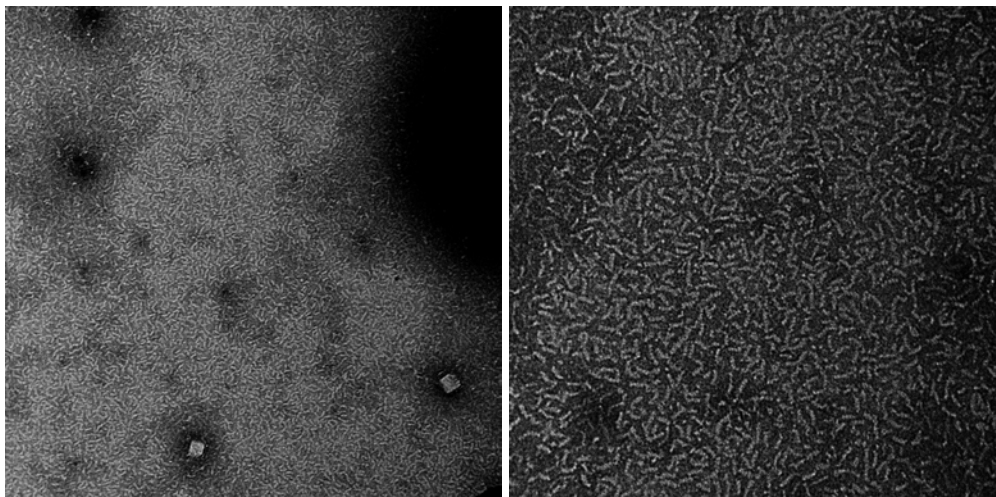
(A&B) Size-exclusion chromatography (SEC) binding assay of RB3-D1-D1 G or GSG with tubulins. Cartoon diagram of the complex is shown in the bottom left corner, and the SDS-PAGE gel shows the binding of the bands.

2.4 Adding in nucleotides did not affect the octamer assembly

To mimic the straight conformation of microtubules, I decided to experiment if the addition of nucleotides would help. In size exclusion chromatography binding assay, the addition of nucleotides did not significantly change the position of the peak, and the elution volume did not change, meaning that there is no larger complex that is formed. Adding in nucleotide GMPCPP into RB3-D1-D1 G + tubulin or RB3-D1-D1 GSG + tubulin also did not improve the tubulin octamer complex formation (**Appendix 2-5 A**). Under negative-stain EM, the formation of the tubulin complex is also similar to the single-row RB3-D1 + tubulin (**Appendix 2-5 B**).



B



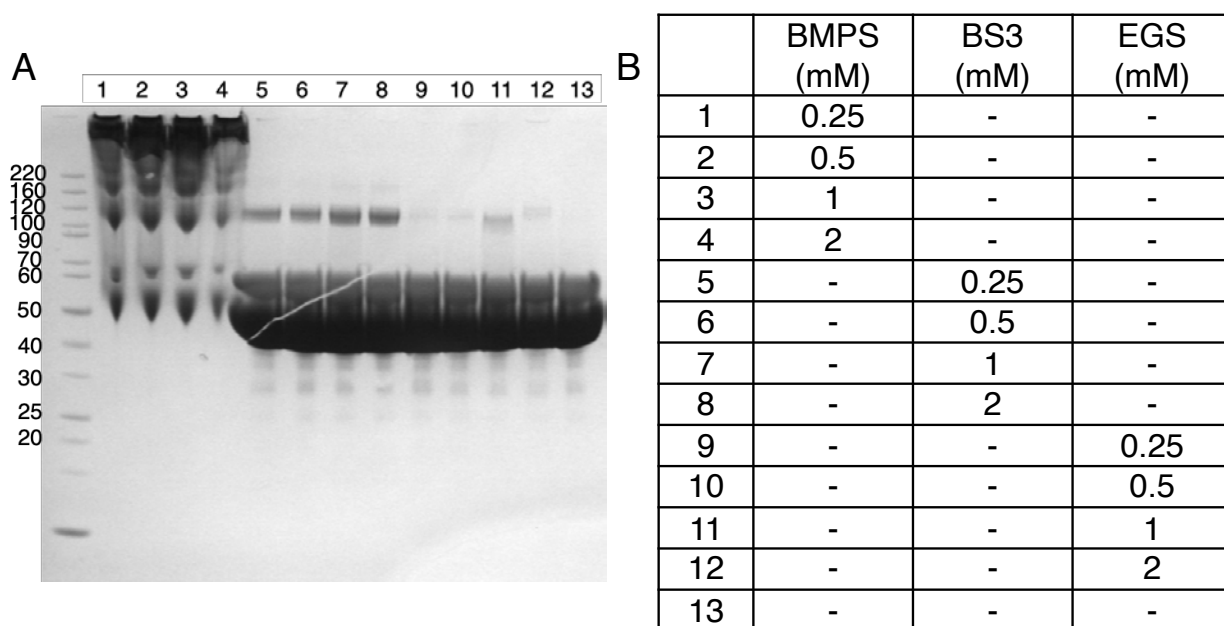
Appendix 2-4 Addition of GMPCPP did not improve the tubulin assembly

(A) Size-exclusion chromatography (SEC) binding assay of RB3-D1-D1, RB3-D1-D1 G or GSG with tubulins, with the addition of 1 mM GMPCPP. (B) Negative-staining EM images of the RB3-D1-D1 with tubulins and GMPCPP.

2.5 Crosslinking of the tubulin octamer

To see if I can promote the double-row tubulin assembly, another approach I tried is the crosslinking of the tubulin assembly using different crosslinkers. These three linkers

are EGS, BMPS, and BS3 (**Appendix 2-6 A&B**). EGS, ethylene glycol bis(succinimidyl succinate), is a crosslinker that contains amine-reactive NHS-ester ends that can react with primary amines. BMPS, N- β -maleimidopropyl-oxysuccinimide ester, is an amine-to-sulfhydryl crosslinker that contains NHS-ester and maleimide reactive groups that are reactive towards amino or sulfhydryl groups. BS3, bis(sulfosuccinimidyl)suberate, that has sulfo-NHS ester and is reactive towards the primary amines. I tried with negative-staining EM, however, I got mostly aggregates. More optimization such as adding in detergents might help with making the grids.



Appendix 2-5 Crosslinking of the tubulin assemblies

(A) Crosslinking of tubulins with Nter-RB3-D1-D1 with crosslinkers BMPS, BS3, or EGS. (B) The conditions used in (A).

2.6 Using EB1 to help forming the tubulin assembly

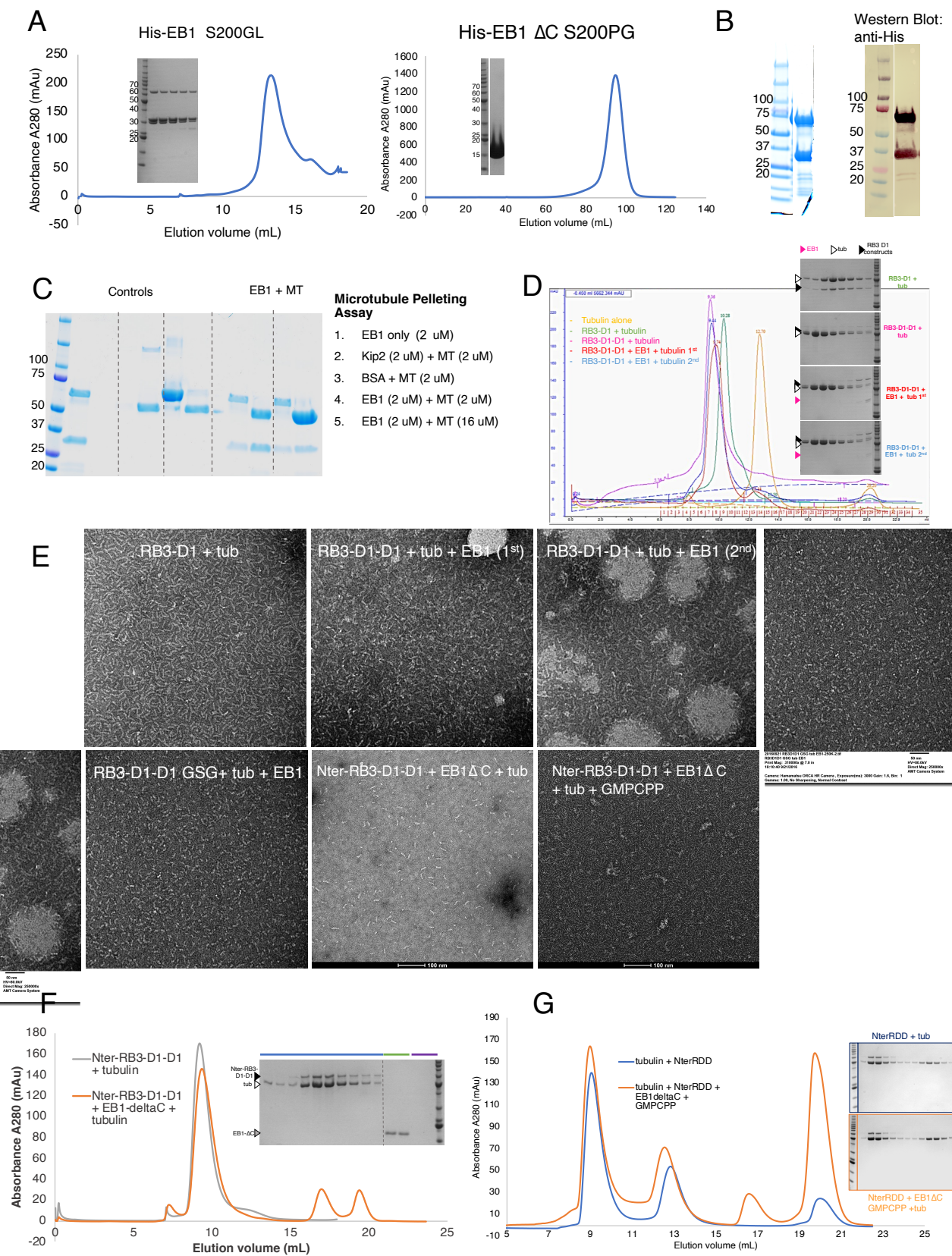
In order to help form the tubulin octamer assembly, end-binding protein EB1 is used. EB1 binds to the center of the four tubulin heterodimers, therefore, it could be promoting the formation of the tubulin lateral interactions.

The expression of 6-His tagged full-length EB1 is in good amount, and the purification scheme is to first go through a nickel affinity column, Q anion exchange column, and then the size exclusion S200 column. On the SDS-PAGE gel, I got two groups of protein, the lower bands is approximately the size of the monomer 32 kDa (with the lowest band possibly being a degradation product), and the higher band is the size of a dimer (**Appendix 2-7 A, left**). To confirm that they are EB1 proteins, I performed Western Blot and microtubule pelleting assay. In Western Blot, I can see that the anti-His antibody is recognizing the 6His-EB1 protein (**Appendix 2-7 B**). In microtubule pelleting assay, I can see that EB1 is indeed interacting with microtubules (**Appendix 2-7 C**).

Next, I did a SEC binding assay of EB1 with the tubulin assembly, RB3-D1-D1 and tubulin. As can be seen in both the SDS-PAGE gel and the chromatogram, there is no significant shift of the EB1+ RB3-D1-D1 + tubulin mix as compared to the RB3-D1-D1 + tubulin, possibly due to not high enough concentration of EB1 for it to form a complex with tubulin (**Appendix 2-7 D**). Nevertheless, I took the peaks of the binding assays, and performed negative-staining to observe the complex. RB3-D1 + tubulin serves as a control, as it shows a single row of tubulins. The density is on the higher end, so it is hard to separate each of the particles. Nevertheless, it seems that in RB3-D1-D1 + tubulin, and also EB1+ RB3-D1-D1 + tubulin, there is no double rows of tubulins (**Appendix 2-7 E**).

The attempt of mixing EB1 + RB3-D1-D1 GSG + tubulin also did not improve the assembly of the two rows of tubulin.

To have a better EB1 construct, I engineered the EB1- Δ C, which only has the N-terminal Calponin Homology domain that binds to the microtubule. It expressed in high amount in *E. coli*, and is a well-behaving protein that gives good yield. After going through similar purification scheme as the full-length EB1, I have a homogenous peak of EB1- Δ C (**Appendix 2-7 A, right**). I used this protein to examine the binding interaction with tubulin assemblies. From both the SDS-PAGE gel and the chromatogram, there is no significant shift of the EB1+ N-ter-RB3-D1-D1 + tubulin mix as compared to the N-ter-RB3-D1-D1 + tubulin (**Appendix 2-7 F**). Furthermore, addition of the nucleotide GMPCPP did not help improve the formation of the two-row tubulin assembly (**Appendix 2-7 G**). I took the peak of the binding assay, and performed negative-staining to look at the complex. There are some large aggregates in the field, but I did not see any two-row tubulin complex (**Appendix 2-7 E**).



Appendix 2-6 EB1 in the binding of tubulins and RB3/D1 constructs

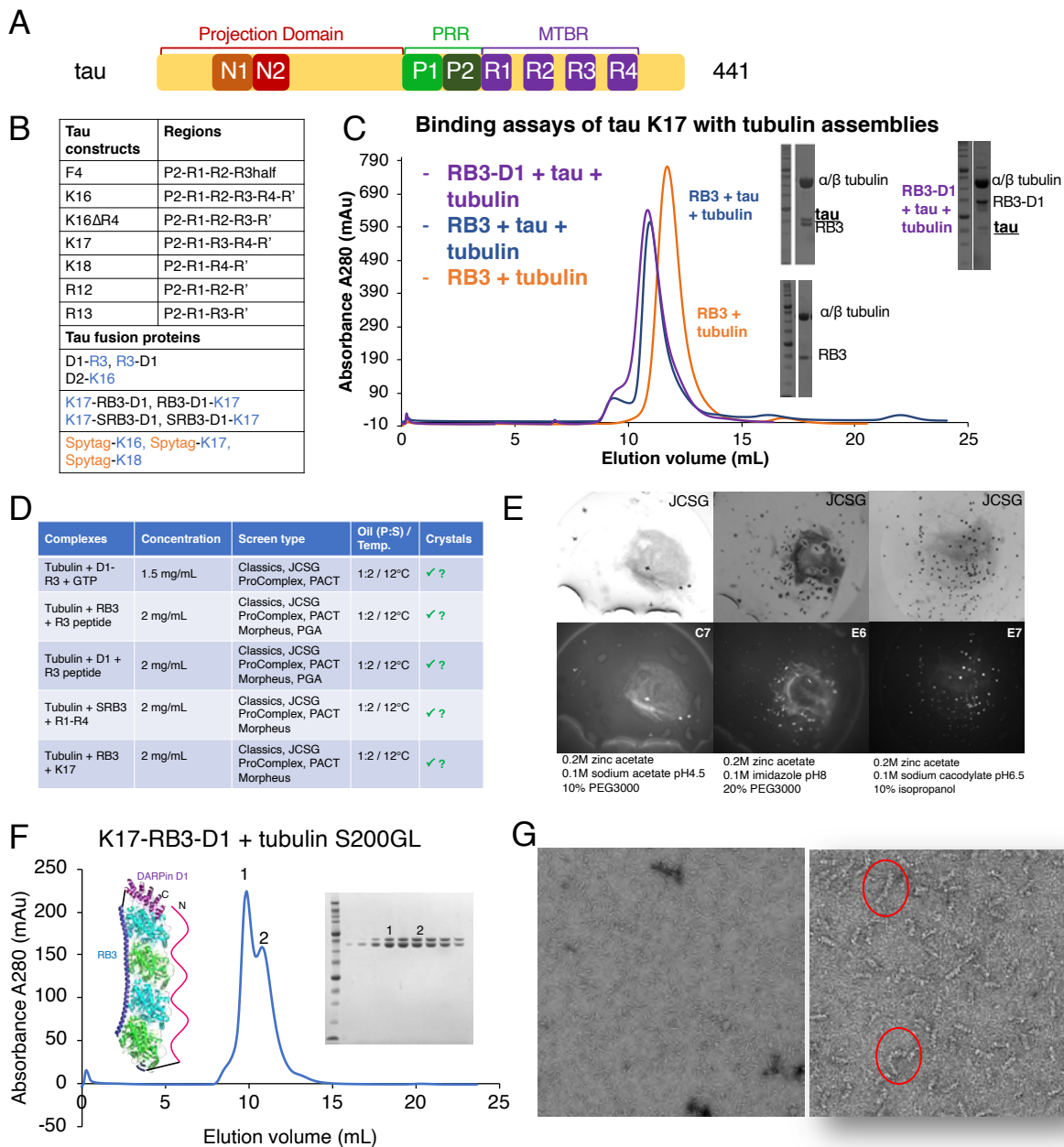
(A) Purification of EB1 (left) and EB1 Δ C (right) on size exclusion columns. (B) Western blot to confirm the validity of EB1 protein. (C) Microtubule pelleting assay of EB1 protein to confirm the binding of EB1 to microtubules. (D) addition of EB1 in the binding assays of RB3/D1 constructs with tubulin. (E) Negative-staining EM images of EB1 with RB3/D1 constructs and tubulins. (F&G) SEC binding assays of EB1 with Nter-RB3-D1-D1 and tubulins, without (F) or with (G) the addition of GMPCPP.

2.7 Structural studies of tau using these tubulin assemblies

To determine the optimal construct of tau-tubulin complex for crystallization, I designed different tau constructs and performed binding assays. The PRR and MTBR regions of tau are suggested to be important for tau binding with microtubules [322], while the projection domain is very flexible [333] and unstructured even in the aggregated PHF and microtubule-bound state of tau [334, 335]. Thus, I made constructs containing only the regions of PRR and MTBR repeat regions 3R (also designated as tau K17, PRR with R1, R3, R4) or 4R (PRR with R1-R4) (**Appendix 2-8 B**).

To start with, I have constructed and performed the size exclusion binding assays of tau K17 with RB3 tubulin assembly, and they seem to be forming a complex of 1 tau protein to 2 tubulin heterodimers (**Appendix 2-8 C**). However, when I was trying to crystallize this complex with commercial screening kits, it seems to be polymerizing in to microtubules and precipitating out of the crystal drop. Upon using the improved tighter sequestering RB3-D1 tubulin assembly, I was able to get initial crystal hits (**Appendix 2-8 D&E**). I have tried optimizing the crystallization conditions, and also make complexes of RB3-D1/tubulin assemblies with the other tau constructs, but I could not obtain large enough crystal for further shooting.

As a result, I turned to making tighter complexes of tau and tubulin, with the help of fusing with tubulin sequestering proteins. I have constructed the fusion proteins K17-RB3-D1 and K17-SRB3-D1 constructs to see if fusing the RB3-D1 with tau K17 can help promote the complex formation with tubulins (**Appendix 2-8 F**). Interestingly, in the traces of size exclusion chromatography binding of K17-RB3-D1 with tubulins, there are two peaks, the first peak eluting around 10mL and the second peak eluting around 11.5 mL. The molecular weight approximation of the first peaks is around ~440 kDa, meaning that the tau K17 is dangling out and interacting with another tubulin dimers, different from the two tubulin dimers that RB3-D1 is binding with. The molecular weight approximation of the second peak is around ~250 kDa, which is the K17-RB3-D1 is interacting with two tubulin heterodimers. I took both peaks and did negative-staining EM, and the images showed mostly two heterodimers complexes, with some of them being larger complexes with 3-4 tubulin dimers (**Appendix 2-8 G**). This could possibly be indicating that the tau is indeed interacting with tubulins, and maybe reaching out to different tubulins than those bound by RB3-D1. This makes up a promising construct, and could be further pursued with cryo-EM.



Appendix 2-7 Structural investigation of tau interaction with tubulins

(A) Domain structure of the full-length tau, with two N-terminal acidic regions (N1, N2), a proline-rich region (PRR), and four repeats (R1 to R4) in the microtubule-binding domain (MTBR). (B) List of tau constructs that I have or I constructed. (C) Size exclusion chromatography binding assays of the tau K17 with tubulin assemblies, indicating the complex formation of tau K17 with tubulin assemblies. (D) The crystallization conditions used. (E) The small star-like crystals of tau K17 with RB3-D1 tubulin assembly. The top panels are the crystal under visible light, while the bottom panels are the crystal under UV light, which demonstrates the crystals are indeed protein crystals. Conditions are labeled. (F) SEC binding assay of tau fusion protein K17-RB3-D1 binding with tubulins. Cartoon figure and the SDS-PAGE gels are shown. (G) Negative-staining EM image of the first peak of (F), with some of the larger complexes circled in red.

3 Discussion

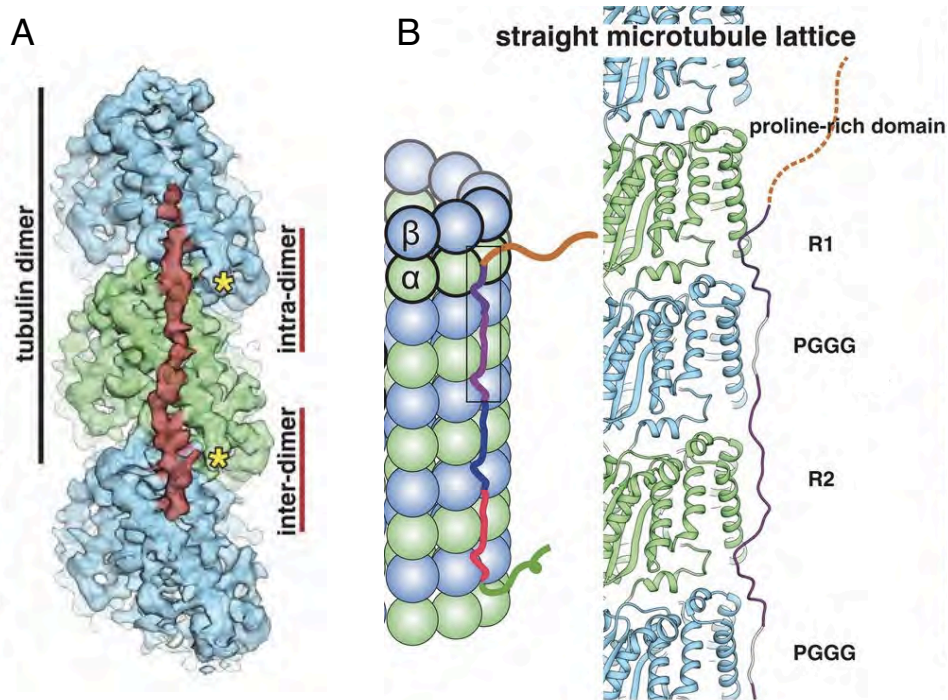
Microtubules are an indispensable part of the cytoskeletal system, and are regulated by numerous MAPs. Because microtubules play multiple important roles in the cells, structural studies of the MAP-microtubule complexes would provide critical insights into the regulation of microtubules. However, even with the advancement of electron microscopy, there are still limitations to solving the structures of MAP-microtubule complexes with current techniques. To creatively work around this problem, I had the idea of making tubulin assemblies that are able to recapitulate the binding interfaces of microtubules. In order to construct these novel tubulin assemblies, I have tried many different methods, including making fusion proteins from RB3 and D1, adding in the linkers to relax the curvature of RB3, adding in nucleotides to help straightening up the tubulins, and also trying out binding partners. These methods have not yet proven to be making the two row tubulins, and the closest result that I get is Nter-RB3-D1-D1, which is only binding to three tubulin dimers. One of the reason that the construction of my tubulin assembly is challenging could be due to the intrinsic curvature of the $\alpha\beta$ -tubulin dimer. There are several studies showing that the structures of the GTP-bound tubulin are in a curved conformation [265, 278, 279]. Further evidence comes from biochemical experiments that the binding affinity of MAPs to tubulins are the same for GTP-bound tubulins versus GDP-bound tubulins, including Stathmin RB3 [297, 336], DARPin [279], and the TOG domain from Stu2 [265]. These could be suggesting that the unpolymerized form of tubulins are in a curved conformation regardless of the nucleotide state [278, 337, 338], in contrast to the idea that the conformation of GDP-tubulin is bent while that of

GTP-tubulin is straight [339]. This indicates that the straightening process is happening in the microtubule lattice, and that the lateral interactions needed that drive $\alpha\beta$ -tubulin conformational changes are not by binding of GTP [338].

I think one way of approaching this challenge is having stronger capping proteins, which are able to take tubulins off from the straightened part of the microtubule besides stopping the tubulins from polymerizing. To achieve this and improve the tubulin assemblies, I actively searched through literature for other potential tubulin capping proteins. I found α Rep protein, which is constructed from screening a library of α -tubulin capping proteins [340]. These α Rep proteins inhibit microtubule assembly and specifically block growth at the microtubule minus-end. iH5 of α Rep, binds tightly to tubulins with affinity around 95 nM. This would be a better binding partner for capping the α -tubulin as compared to the stathmin N-terminus β -hairpin, and hopefully would provide a tighter interaction to zip up the two rows of tubulins. Once succeeded, this novel tubulin assembly could be advantageous in the structural and mechanistic studies of MAPs with microtubules/tubulins.

Although free tau lacks stable secondary and tertiary structure in solution [320, 341], it is predicted that it will locally fold [327] and become structured upon microtubule binding [342]. To have mechanistic insights into tau regulation of microtubules, I was trying to solve the tau-tubulin crystal structure to observe what structures tau uses to interact with microtubules and the key interaction residues involved in this interaction. Moreover, I was trying to compare the conformational changes between tau binding to free tubulin dimers, curved and straight protofilaments (using my tubulin platforms SRB3-

D1, RB3-D1, and Nter-RB3-D1-D1, respectively) and elucidate the mechanism by which tau stabilizes microtubule. I have tried extensively with different tau constructs and different methods of obtaining the structure of tau-tubulin complex, but not yet succeeded. I have tried crystallization extensively using the microbatch-under-oil method [343], however, I wasn't able to get good crystals for shooting. One interesting thing noteworthy is that the crystals I got all had zinc ion in their conditions, which is important in the formation of microtubules [344]. This could be due to the highly flexible nature of tau, and also that it is really hard to have tau proteins stably bind to the tubulin complexes. The Nogales group showed a structure that is made up of four-repeats of R1 region of tau binding to microtubules [325]. Their model shows that each tau repeat is centered on a single α -tubulin and connecting three tubulin monomers, having an extended conformation that includes both intra- and interdimer interfaces. They found that the major site of phosphorylation Ser262 is an important point of contact with tubulin, and also mapped out the anchor point, tau R1, that is the major tau-tubulin binding site. Although their discovery is a major breakthrough, key questions remain. Because they did not obtain the four R-regions of tau with tubulin structure, the structures that they have are based on four repeats of R1 or R2, which still leaves the question open: what are the different roles of the different R repeats of tau? Are they regulated differently and interact differently with tubulins? And also, the role of the C-terminal tail of tubulins in this binding interaction. These are interesting questions that remains to be addressed.



Appendix 3-1 Tau binding to microtubules

(A) The binding of a stretch of tau spans over three tubulin monomers, binding across both intra- and interdimer tubulin interfaces (only one repeat of tau is shown). The positions of the C termini of tubulin are indicated with asterisks. (B) The model of tau binding along a protofilament. Adapted from [325].

4 Material and Methods

4.1 Protein expression and purification

RB3/D1 or tau constructs were expressed in *E. coli* BL21 (DE3). Cells were resuspended in 50 mM phosphate pH 7.4, 150 mM KCl (RB3/D1) or 50 mM KCl (tau), 1 mM EGTA, 1 mM MgCl₂, 0.5 mM TCEP and lysed using a microfluidizer. Cell debris was clarified by centrifugation at 26,892 X g for 25 min. These proteins were purified using Ni-NTA affinity column followed by salt gradient ion exchange column, and lastly through and size-exclusion chromatography Superdex 200 10/300 GL column.

4.2 Size-exclusion chromatography (SEC) binding assays

RB3/D1 constructs were mixed with tubulins, with or without the addition of tau constructs, for 30 minutes to 1 hour on ice in the binding assays. Then these complex mixtures were applied to a Superdex 200 10/300 GL column (GE Healthcare). The UV absorbance at 280 nm was recorded to monitor the elution of SAMHD1 oligomers.

4.3 Crystallization

The tau-tubulin complex was crystallized in the presence of RB3/D1 constructs, with commercial conditions and the microbatch under oil method. Protein at 1-5 mg/mL was mixed with crystallization buffer at a 1:1 ratio (1 μ L protein: 1 μ L precipitant) and incubated

at room temperature 25 °C. Optimization of crystals are done based on the conditions of the obtained crystal.

4.4 Negative-staining EM

RB3/D1 constructs with tubulin complex are diluted in buffer, and then put on the carbon holey grids for obtaining images of negative-staining EM. Procedure is similar to that described above in section 10.9.

References

1. Brown, T.R., *I am the Berlin patient: a personal reflection*. AIDS Res Hum Retroviruses, 2015. **31**(1): p. 2-3.
2. UNAIDS. 2018 GLOBAL HIV STATISTICS. 2019 [cited 2019/12/27]; Available from: http://www.unaids.org/sites/default/files/media_asset/UNAIDS_FactSheet_en.pdf
3. Matthew Warren, Second patient free of HIV after stem-cell therapy, Nature Letters, 05 MARCH 2019
4. Barre-Sinoussi, F., A.L. Ross, and J.F. Delfraissy, *Past, present and future: 30 years of HIV research*. Nat Rev Microbiol, 2013. **11**(12): p. 877-83.
5. Novikova, M., et al., *Multiple Roles of HIV-1 Capsid during the Virus Replication Cycle*. Virol Sin, 2019. **34**(2): p. 119-134.
6. Jia, X., Q. Zhao, and Y. Xiong, *HIV suppression by host restriction factors and viral immune evasion*. Curr Opin Struct Biol, 2015. **31**: p. 106-14.
7. Ganser, B.K., et al., *Assembly and analysis of conical models for the HIV-1 core*. Science, 1999. **283**(5398): p. 80-3.
8. Li, S., et al., *Image reconstructions of helical assemblies of the HIV-1 CA protein*. Nature, 2000. **407**(6802): p. 409-13.
9. Zhao, G., et al., *Mature HIV-1 capsid structure by cryo-electron microscopy and all-atom molecular dynamics*. Nature, 2013. **497**(7451): p. 643-6.
10. Sundquist, W.I. and H.G. Krausslich, *HIV-1 assembly, budding, and maturation*. Cold Spring Harb Perspect Med, 2012. **2**(7): p. a006924.
11. Gres, A.T., et al., *STRUCTURAL VIROLOGY. X-ray crystal structures of native HIV-1 capsid protein reveal conformational variability*. Science, 2015. **349**(6243): p. 99-103.
12. Byeon, I.J., et al., *Structural convergence between Cryo-EM and NMR reveals intersubunit interactions critical for HIV-1 capsid function*. Cell, 2009. **139**(4): p. 780-90.
13. Ganser-Pornillos, B.K., A. Cheng, and M. Yeager, *Structure of full-length HIV-1 CA: a model for the mature capsid lattice*. Cell, 2007. **131**(1): p. 70-9.
14. Pornillos, O., et al., *X-ray structures of the hexameric building block of the HIV capsid*. Cell, 2009. **137**(7): p. 1282-92.
15. Ehrlich, L.S., B.E. Agresta, and C.A. Carter, *Assembly of recombinant human immunodeficiency virus type 1 capsid protein in vitro*. J Virol, 1992. **66**(8): p. 4874-83.
16. Gross, I., H. Hohenberg, and H.G. Krausslich, *In vitro assembly properties of purified bacterially expressed capsid proteins of human immunodeficiency virus*. Eur J Biochem, 1997. **249**(2): p. 592-600.
17. Campbell, E.M. and T.J. Hope, *HIV-1 capsid: the multifaceted key player in HIV-1 infection*. Nat Rev Microbiol, 2015. **13**(8): p. 471-83.
18. Rasaiyaah, J., et al., *HIV-1 evades innate immune recognition through specific cofactor recruitment*. Nature, 2013. **503**(7476): p. 402-405.
19. Liu, Z., et al., *The interferon-inducible MxB protein inhibits HIV-1 infection*. Cell Host Microbe, 2013. **14**(4): p. 398-410.
20. Hilditch, L. and G.J. Towers, *A model for cofactor use during HIV-1 reverse transcription and nuclear entry*. Curr Opin Virol, 2014. **4**: p. 32-6.
21. Schaller, T., et al., *HIV-1 capsid-cyclophilin interactions determine nuclear import pathway, integration targeting and replication efficiency*. PLoS Pathog, 2011. **7**(12): p. e1002439.
22. Yamashita, M. and A.N. Engelman, *Capsid-Dependent Host Factors in HIV-1 Infection*. Trends Microbiol, 2017. **25**(9): p. 741-755.
23. Fassati, A., *Multiple roles of the capsid protein in the early steps of HIV-1 infection*. Virus Res, 2012. **170**(1-2): p. 15-24.
24. Forshey, B.M., et al., *Formation of a human immunodeficiency virus type 1 core of optimal stability is crucial for viral replication*. J Virol, 2002. **76**(11): p. 5667-77.
25. Tang, C., et al., *Antiviral inhibition of the HIV-1 capsid protein*. J Mol Biol, 2003. **327**(5): p. 1013-20.

26. Zhang, J., X. Liu, and E. De Clercq, *Capsid (CA) protein as a novel drug target: recent progress in the research of HIV-1 CA inhibitors*. Mini Rev Med Chem, 2009. **9**(4): p. 510-8.
27. Thenin-Houssier, S. and S.T. Valente, *HIV-1 Capsid Inhibitors as Antiretroviral Agents*. Curr HIV Res, 2016. **14**(3): p. 270-82.
28. Fenstermacher, Katherine (2013): The mature HIV virion. figshare. Figure. <https://doi.org/10.6084/m9.figshare.862069.v2>
29. Ganser-Pornillos, B.K., et al., *Assembly properties of the human immunodeficiency virus type 1 CA protein*. J Virol, 2004. **78**(5): p. 2545-52.
30. Pornillos, O., B.K. Ganser-Pornillos, and M. Yeager, *Atomic-level modelling of the HIV capsid*. Nature, 2011. **469**(7330): p. 424-7.
31. Luby-Phelps, K., *Cytoarchitecture and physical properties of cytoplasm: volume, viscosity, diffusion, intracellular surface area*. Int Rev Cytol, 2000. **192**: p. 189-221.
32. Gaudin, R., et al., *HIV trafficking in host cells: motors wanted!* Trends Cell Biol, 2013. **23**(12): p. 652-62.
33. Sabo, Y., et al., *HIV-1 induces the formation of stable microtubules to enhance early infection*. Cell Host Microbe, 2013. **14**(5): p. 535-46.
34. Fernandez, J., et al., *Microtubule-associated proteins 1 (MAP1) promote human immunodeficiency virus type 1 (HIV-1) intracytoplasmic routing to the nucleus*. J Biol Chem, 2015. **290**(8): p. 4631-46.
35. Li, R. and G.G. Gundersen, *Beyond polymer polarity: how the cytoskeleton builds a polarized cell*. Nat Rev Mol Cell Biol, 2008. **9**(11): p. 860-73.
36. Janke, C. and J.C. Bulinski, *Post-translational regulation of the microtubule cytoskeleton: mechanisms and functions*. Nat Rev Mol Cell Biol, 2011. **12**(12): p. 773-86.
37. McDonald, D., et al., *Visualization of the intracellular behavior of HIV in living cells*. J Cell Biol, 2002. **159**(3): p. 441-52.
38. Sodeik, B., *Mechanisms of viral transport in the cytoplasm*. Trends Microbiol, 2000. **8**(10): p. 465-72.
39. Smith, G.A. and L.W. Enquist, *Break ins and break outs: viral interactions with the cytoskeleton of Mammalian cells*. Annu Rev Cell Dev Biol, 2002. **18**: p. 135-61.
40. Bukrinskaya, A., et al., *Establishment of a functional human immunodeficiency virus type 1 (HIV-1) reverse transcription complex involves the cytoskeleton*. J Exp Med, 1998. **188**(11): p. 2113-25.
41. Mabit, H., et al., *Intact microtubules support adenovirus and herpes simplex virus infections*. J Virol, 2002. **76**(19): p. 9962-71.
42. Jayappa, K.D., et al., *Human immunodeficiency virus type 1 employs the cellular dynein light chain 1 protein for reverse transcription through interaction with its integrase protein*. J Virol, 2015. **89**(7): p. 3497-511.
43. Petit, C., et al., *Targeting of incoming retroviral Gag to the centrosome involves a direct interaction with the dynein light chain 8*. J Cell Sci, 2003. **116**(Pt 16): p. 3433-42.
44. Su, Y., et al., *Microtubule-dependent retrograde transport of bovine immunodeficiency virus*. Cell Microbiol, 2010. **12**(8): p. 1098-107.
45. de Soultrait, V.R., et al., *HIV-1 integrase interacts with yeast microtubule-associated proteins*. Biochim Biophys Acta, 2002. **1575**(1-3): p. 40-8.
46. Indran, S.V., M.E. Ballestas, and W.J. Britt, *Bicaudal D1-dependent trafficking of human cytomegalovirus tegument protein pp150 in virus-infected cells*. J Virol, 2010. **84**(7): p. 3162-77.
47. Arhel, N., et al., *Quantitative four-dimensional tracking of cytoplasmic and nuclear HIV-1 complexes*. Nat Methods, 2006. **3**(10): p. 817-24.
48. Tang, Y., et al., *Cellular motor protein KIF-4 associates with retroviral Gag*. J Virol, 1999. **73**(12): p. 10508-13.
49. Martinez, N.W., et al., *Kinesin KIF4 regulates intracellular trafficking and stability of the human immunodeficiency virus type 1 Gag polyprotein*. J Virol, 2008. **82**(20): p. 9937-50.
50. Azevedo, C., et al., *Inositol pyrophosphate mediated pyrophosphorylation of AP3B1 regulates HIV-1 Gag release*. Proc Natl Acad Sci U S A, 2009. **106**(50): p. 21161-6.

51. Gaudin, R., et al., *Critical role for the kinesin KIF3A in the HIV life cycle in primary human macrophages*. J Cell Biol, 2012. **199**(3): p. 467-79.
52. Sodeik, B., *Unchain my heart, baby let me go--the entry and intracellular transport of HIV*. J Cell Biol, 2002. **159**(3): p. 393-5.
53. Kuroda, S., et al., *Mammalian homologue of the Caenorhabditis elegans UNC-76 protein involved in axonal outgrowth is a protein kinase C zeta-interacting protein*. J Cell Biol, 1999. **144**(3): p. 403-11.
54. Gindhart, J.G., et al., *The kinesin-associated protein UNC-76 is required for axonal transport in the Drosophila nervous system*. Mol Biol Cell, 2003. **14**(8): p. 3356-65.
55. Okumura, F., et al., *Functional regulation of FEZ1 by the U-box-type ubiquitin ligase E4B contributes to neuritogenesis*. J Biol Chem, 2004. **279**(51): p. 53533-43.
56. Fujita, T., et al., *Axonal guidance protein FEZ1 associates with tubulin and kinesin motor protein to transport mitochondria in neurites of NGF-stimulated PC12 cells*. Biochem Biophys Res Commun, 2007. **361**(3): p. 605-10.
57. Ikuta, J., et al., *Fasciculation and elongation protein zeta-1 (FEZ1) participates in the polarization of hippocampal neuron by controlling the mitochondrial motility*. Biochem Biophys Res Commun, 2007. **353**(1): p. 127-32.
58. Bloom, L. and H.R. Horvitz, *The Caenorhabditis elegans gene unc-76 and its human homologs define a new gene family involved in axonal outgrowth and fasciculation*. Proc Natl Acad Sci U S A, 1997. **94**(7): p. 3414-9.
59. Verhey, K.J., et al., *Cargo of kinesin identified as JIP scaffolding proteins and associated signaling molecules*. J Cell Biol, 2001. **152**(5): p. 959-70.
60. Hirokawa, N. and R. Takemura, *Molecular motors and mechanisms of directional transport in neurons*. Nat Rev Neurosci, 2005. **6**(3): p. 201-14.
61. Blasius, T.L., et al., *Two binding partners cooperate to activate the molecular motor Kinesin-1*. J Cell Biol, 2007. **176**(1): p. 11-7.
62. Suzuki, T., et al., *Identification of FEZ1 as a protein that interacts with JC virus agnoprotein and microtubules: role of agnoprotein-induced dissociation of FEZ1 from microtubules in viral propagation*. J Biol Chem, 2005. **280**(26): p. 24948-56.
63. Malikov, V., et al., *HIV-1 capsids bind and exploit the kinesin-1 adaptor FEZ1 for inward movement to the nucleus*. Nat Commun, 2015. **6**: p. 6660.
64. Maturana, A.D., T. Fujita, and S. Kuroda, *Functions of fasciculation and elongation protein zeta-1 (FEZ1) in the brain*. ScientificWorldJournal, 2010. **10**: p. 1646-54.
65. Toda, H., et al., *UNC-51/ATG1 kinase regulates axonal transport by mediating motor-cargo assembly*. Genes Dev, 2008. **22**(23): p. 3292-307.
66. Chua, J.J., et al., *Phosphorylation-regulated axonal dependent transport of syntaxin 1 is mediated by a Kinesin-1 adapter*. Proc Natl Acad Sci U S A, 2012. **109**(15): p. 5862-7.
67. Malikov, V. and M.H. Naghavi, *Localized Phosphorylation of a Kinesin-1 Adaptor by a Capsid-Associated Kinase Regulates HIV-1 Motility and Uncoating*. Cell Rep, 2017. **20**(12): p. 2792-2799.
68. Lanza, D.C., et al., *Human FEZ1 has characteristics of a natively unfolded protein and dimerizes in solution*. Proteins, 2009. **74**(1): p. 104-21.
69. Alborghetti, M.R., et al., *Structural analysis of intermolecular interactions in the kinesin adaptor complex fasciculation and elongation protein zeta 1/ short coiled-coil protein (FEZ1/SCOCO)*. PLoS One, 2013. **8**(10): p. e76602.
70. Miyoshi, K., et al., *Disrupted-In-Schizophrenia 1, a candidate gene for schizophrenia, participates in neurite outgrowth*. Mol Psychiatry, 2003. **8**(7): p. 685-94.
71. Assmann, E.M., et al., *FEZ1 dimerization and interaction with transcription regulatory proteins involves its coiled-coil region*. J Biol Chem, 2006. **281**(15): p. 9869-81.
72. Alborghetti, M.R., A.S. Furlan, and J. Kobarg, *FEZ2 has acquired additional protein interaction partners relative to FEZ1: functional and evolutionary implications*. PLoS One, 2011. **6**(3): p. e17426.

73. Fujita, T., et al., *Identification of a tissue-non-specific homologue of axonal fasciculation and elongation protein zeta-1*. *Biochem Biophys Res Commun*, 2004. **313**(3): p. 738-44.
74. Huang, P.T., et al., *FEZ1 Is Recruited to a Conserved Cofactor Site on Capsid to Promote HIV-1 Trafficking*. *Cell Rep*, 2019. **28**(9): p. 2373-2385 e7.
75. Summers, B.J., et al., *Modular HIV-1 Capsid Assemblies Reveal Diverse Host-Capsid Recognition Mechanisms*. *Cell Host Microbe*, 2019. **26**(2): p. 203-216 e6.
76. Pornillos, O., et al., *Disulfide bond stabilization of the hexameric capsomer of human immunodeficiency virus*. *J Mol Biol*, 2010. **401**(5): p. 985-95.
77. Ganser-Pornillos, B.K., M. Yeager, and W.I. Sundquist, *The structural biology of HIV assembly*. *Curr Opin Struct Biol*, 2008. **18**(2): p. 203-17.
78. Bharat, T.A., et al., *Cryo-electron microscopy of tubular arrays of HIV-1 Gag resolves structures essential for immature virus assembly*. *Proc Natl Acad Sci U S A*, 2014. **111**(22): p. 8233-8.
79. Momany, C., et al., *Crystal structure of dimeric HIV-1 capsid protein*. *Nat Struct Biol*, 1996. **3**(9): p. 763-70.
80. Berthet-Colominas, C., et al., *Head-to-tail dimers and interdomain flexibility revealed by the crystal structure of HIV-1 capsid protein (p24) complexed with a monoclonal antibody Fab*. *EMBO J*, 1999. **18**(5): p. 1124-36.
81. Mattei, S., et al., *The structure and flexibility of conical HIV-1 capsids determined within intact virions*. *Science*, 2016. **354**(6318): p. 1434-1437.
82. Smaga, S.S., et al., *MxB Restricts HIV-1 by Targeting the Tri-hexamer Interface of the Viral Capsid*. *Structure*, 2019. **27**(8): p. 1234-1245 e5.
83. Perilla, J.R. and K. Schulten, *Physical properties of the HIV-1 capsid from all-atom molecular dynamics simulations*. *Nat Commun*, 2017. **8**: p. 15959.
84. Zhou, J., et al., *HIV-1 Resistance to the Capsid-Targeting Inhibitor PF74 Results in Altered Dependence on Host Factors Required for Virus Nuclear Entry*. *J Virol*, 2015. **89**(17): p. 9068-79.
85. Bhattacharya, A., et al., *Structural basis of HIV-1 capsid recognition by PF74 and CPSF6*. *Proc Natl Acad Sci U S A*, 2014. **111**(52): p. 18625-30.
86. Price, A.J., et al., *Host cofactors and pharmacologic ligands share an essential interface in HIV-1 capsid that is lost upon disassembly*. *PLoS Pathog*, 2014. **10**(10): p. e1004459.
87. Yoo, S., et al., *Molecular recognition in the HIV-1 capsid/cyclophilin A complex*. *J Mol Biol*, 1997. **269**(5): p. 780-95.
88. Biris, N., et al., *Structure of the rhesus monkey TRIM5alpha PRYSPRY domain, the HIV capsid recognition module*. *Proc Natl Acad Sci U S A*, 2012. **109**(33): p. 13278-83.
89. Freire, E., *Do enthalpy and entropy distinguish first in class from best in class?* *Drug Discov Today*, 2008. **13**(19-20): p. 869-74.
90. Velazquez-Campoy, A., Y. Kiso, and E. Freire, *The binding energetics of first- and second-generation HIV-1 protease inhibitors: implications for drug design*. *Arch Biochem Biophys*, 2001. **390**(2): p. 169-75.
91. Mortuza, G.B., et al., *High-resolution structure of a retroviral capsid hexameric amino-terminal domain*. *Nature*, 2004. **431**(7007): p. 481-5.
92. Velazquez-Campoy, A., M.J. Todd, and E. Freire, *HIV-1 protease inhibitors: enthalpic versus entropic optimization of the binding affinity*. *Biochemistry*, 2000. **39**(9): p. 2201-7.
93. Ohtaka, H. and E. Freire, *Adaptive inhibitors of the HIV-1 protease*. *Prog Biophys Mol Biol*, 2005. **88**(2): p. 193-208.
94. Jacques, D.A., et al., *HIV-1 uses dynamic capsid pores to import nucleotides and fuel encapsidated DNA synthesis*. *Nature*, 2016. **536**(7616): p. 349-53.
95. Goujon, C., et al., *Human MX2 is an interferon-induced post-entry inhibitor of HIV-1 infection*. *Nature*, 2013. **502**(7472): p. 559-62.
96. Kane, M., et al., *MX2 is an interferon-induced inhibitor of HIV-1 infection*. *Nature*, 2013. **502**(7472): p. 563-6.
97. Busnadiego, I., et al., *Host and viral determinants of Mx2 antiretroviral activity*. *J Virol*, 2014. **88**(14): p. 7738-52.

98. Matreyek, K.A., et al., *Host and viral determinants for MxB restriction of HIV-1 infection*. *Retrovirology*, 2014. **11**: p. 90.
99. Gamble, T.R., et al., *Crystal structure of human cyclophilin A bound to the amino-terminal domain of HIV-1 capsid*. *Cell*, 1996. **87**(7): p. 1285-94.
100. Dick, R.A., et al., *IP6 Regulation of HIV Capsid Assembly, Stability, and Uncoating*. *Viruses*, 2018. **10**(11).
101. Marquez, C.L., et al., *Kinetics of HIV-1 capsid uncoating revealed by single-molecule analysis*. *Elife*, 2018. **7**.
102. Gamble, T.R., et al., *Structure of the carboxyl-terminal dimerization domain of the HIV-1 capsid protein*. *Science*, 1997. **278**(5339): p. 849-53.
103. Kingston, R.L., et al., *Structure and self-association of the Rous sarcoma virus capsid protein*. *Structure*, 2000. **8**(6): p. 617-28.
104. Campos-Olivas, R., J.L. Newman, and M.F. Summers, *Solution structure and dynamics of the Rous sarcoma virus capsid protein and comparison with capsid proteins of other retroviruses*. *J Mol Biol*, 2000. **296**(2): p. 633-49.
105. Cornilescu, C.C., et al., *Structural analysis of the N-terminal domain of the human T-cell leukemia virus capsid protein*. *J Mol Biol*, 2001. **306**(4): p. 783-97.
106. Tang, C., Y. Ndassa, and M.F. Summers, *Structure of the N-terminal 283-residue fragment of the immature HIV-1 Gag polyprotein*. *Nat Struct Biol*, 2002. **9**(7): p. 537-43.
107. Rihn, S.J., et al., *Extreme genetic fragility of the HIV-1 capsid*. *PLoS Pathog*, 2013. **9**(6): p. e1003461.
108. von Schwedler, U.K., et al., *Functional surfaces of the human immunodeficiency virus type 1 capsid protein*. *J Virol*, 2003. **77**(9): p. 5439-50.
109. Goldstone, D.C., et al., *Structural studies of postentry restriction factors reveal antiparallel dimers that enable avid binding to the HIV-1 capsid lattice*. *Proc Natl Acad Sci U S A*, 2014. **111**(26): p. 9609-14.
110. Haller, O., *Dynamins are forever: MxB inhibits HIV-1*. *Cell Host Microbe*, 2013. **14**(4): p. 371-3.
111. Strickler, S.S., et al., *Protein stability and surface electrostatics: a charged relationship*. *Biochemistry*, 2006. **45**(9): p. 2761-6.
112. Heyrana, K.J., et al., *Contributions of Charged Residues in Structurally Dynamic Capsid Surface Loops to Rous Sarcoma Virus Assembly*. *J Virol*, 2016. **90**(12): p. 5700-14.
113. Freddolino, P.L., et al., *Molecular dynamics simulations of the complete satellite tobacco mosaic virus*. *Structure*, 2006. **14**(3): p. 437-49.
114. Kotecha, A., et al., *Structure-based energetics of protein interfaces guides foot-and-mouth disease virus vaccine design*. *Nat Struct Mol Biol*, 2015. **22**(10): p. 788-94.
115. Colgan, J., et al., *Binding of the human immunodeficiency virus type 1 Gag polyprotein to cyclophilin A is mediated by the central region of capsid and requires Gag dimerization*. *J Virol*, 1996. **70**(7): p. 4299-310.
116. Luban, J., et al., *Human immunodeficiency virus type 1 Gag protein binds to cyclophilins A and B*. *Cell*, 1993. **73**(6): p. 1067-78.
117. Sokolskaja, E., D.M. Sayah, and J. Luban, *Target cell cyclophilin A modulates human immunodeficiency virus type 1 infectivity*. *J Virol*, 2004. **78**(23): p. 12800-8.
118. Hatzioannou, T., et al., *Cyclophilin interactions with incoming human immunodeficiency virus type 1 capsids with opposing effects on infectivity in human cells*. *J Virol*, 2005. **79**(1): p. 176-83.
119. Franke, E.K., H.E. Yuan, and J. Luban, *Specific incorporation of cyclophilin A into HIV-1 virions*. *Nature*, 1994. **372**(6504): p. 359-62.
120. Li, L., et al., *Structural analysis and optimization of the covalent association between SpyCatcher and a peptide Tag*. *J Mol Biol*, 2014. **426**(2): p. 309-17.
121. Gray, E.R., et al., *Unravelling the Molecular Basis of High Affinity Nanobodies against HIV p24: In Vitro Functional, Structural, and in Silico Insights*. *ACS Infect Dis*, 2017. **3**(7): p. 479-491.
122. Li, Y.L., et al., *Primate TRIM5 proteins form hexagonal nets on HIV-1 capsids*. *Elife*, 2016. **5**.

123. Zhang, P., X. Meng, and G. Zhao, *Tubular crystals and helical arrays: structural determination of HIV-1 capsid assemblies using iterative helical real-space reconstruction*. *Methods Mol Biol*, 2013. **955**: p. 381-99.
124. Meng, X., G. Zhao, and P. Zhang, *Structure of HIV-1 capsid assemblies by cryo-electron microscopy and iterative helical real-space reconstruction*. *J Vis Exp*, 2011(54).
125. Li, X. and J. Sodroski, *The TRIM5alpha B-box 2 domain promotes cooperative binding to the retroviral capsid by mediating higher-order self-association*. *J Virol*, 2008. **82**(23): p. 11495-502.
126. Yang, H., et al., *Structural insight into HIV-1 capsid recognition by rhesus TRIM5alpha*. *Proc Natl Acad Sci U S A*, 2012. **109**(45): p. 18372-7.
127. Buffone, C., et al., *Contribution of MxB oligomerization to HIV-1 capsid binding and restriction*. *J Virol*, 2015. **89**(6): p. 3285-94.
128. Vauquelin, G. and S.J. Charlton, *Exploring avidity: understanding the potential gains in functional affinity and target residence time of bivalent and heterobivalent ligands*. *Br J Pharmacol*, 2013. **168**(8): p. 1771-85.
129. Rudnick, S.I. and G.P. Adams, *Affinity and avidity in antibody-based tumor targeting*. *Cancer Biother Radiopharm*, 2009. **24**(2): p. 155-61.
130. Mallery, D.L., et al., *IP6 is an HIV pocket factor that prevents capsid collapse and promotes DNA synthesis*. *Elife*, 2018. **7**.
131. Chayen, N.E., P.D. Shaw Stewart, and D.M. Blow, *Microbatch crystallization under oil — a new technique allowing many small-volume crystallization trials*. *Journal of Crystal Growth*, 1992. **122**(1): p. 176-180.
132. McCoy, A.J., et al., *Phaser crystallographic software*. *J Appl Crystallogr*, 2007. **40**(Pt 4): p. 658-674.
133. Vagin, A.A., et al., *REFMAC5 dictionary: organization of prior chemical knowledge and guidelines for its use*. *Acta Crystallogr D Biol Crystallogr*, 2004. **60**(Pt 12 Pt 1): p. 2184-95.
134. Emsley, P. and K. Cowtan, *Coot: model-building tools for molecular graphics*. *Acta Crystallogr D Biol Crystallogr*, 2004. **60**(Pt 12 Pt 1): p. 2126-32.
135. Schrodinger, LLC, *The PyMOL Molecular Graphics System, Version 1.8*. 2015.
136. Baker, N.A., et al., *Electrostatics of nanosystems: application to microtubules and the ribosome*. *Proc Natl Acad Sci U S A*, 2001. **98**(18): p. 10037-41.
137. Eswar, N., et al., *Comparative protein structure modeling using Modeller*. *Curr Protoc Bioinformatics*, 2006. **Chapter 5**: p. Unit-5 6.
138. Dolinsky, T.J., et al., *PDB2PQR: expanding and upgrading automated preparation of biomolecular structures for molecular simulations*. *Nucleic Acids Res*, 2007. **35**(Web Server issue): p. W522-5.
139. Leaver-Fay, A., et al., *ROSETTA3: an object-oriented software suite for the simulation and design of macromolecules*. *Methods Enzymol*, 2011. **487**: p. 545-74.
140. Jorgensen, W.L.a.J., C. , *Temperature dependence of TIP3P, SPC, and TIP4P water from NPT Monte Carlo simulations: Seeking temperatures of maximum density*. *J. Comput. Chem.*, 1998(19): p. 1179-1186.
141. Phillips JC, B.R., Wang W, Gumbart J, Tajkhorshid E, Villa E, Chipot C, Skeel RD, Kalé L, Schulten K., *Scalable molecular dynamics with NAMD*. *J Comput Chem.*, 2005. **26**: p. 1781-802.
142. Shaw, D.E., et al., *Anton 2: raising the bar for performance and programmability in a special-purpose molecular dynamics supercomputer*, in *Proceedings of the International Conference for High Performance Computing, Networking, Storage and Analysis*. 2014, IEEE Press: New Orleans, Louisiana. p. 41-53.
143. Huang, J., et al., *CHARMM36m: an improved force field for folded and intrinsically disordered proteins*. *Nat Methods*, 2017. **14**(1): p. 71-73.
144. Lippert, R.A., et al., *Accurate and efficient integration for molecular dynamics simulations at constant temperature and pressure*. *J Chem Phys*, 2013. **139**(16): p. 164106.
145. Shan, Y., et al., *Gaussian split Ewald: A fast Ewald mesh method for molecular simulation*. *J Chem Phys*, 2005. **122**(5): p. 54101.

146. Tinevez, J.Y., et al., *TrackMate: An open and extensible platform for single-particle tracking*. *Methods*, 2017. **115**: p. 80-90.
147. Nogales, E., S.G. Wolf, and K.H. Downing, *Structure of the alpha beta tubulin dimer by electron crystallography*. *Nature*, 1998. **391**(6663): p. 199-203.
148. Lowe, J., et al., *Refined structure of alpha beta-tubulin at 3.5 A resolution*. *J Mol Biol*, 2001. **313**(5): p. 1045-57.
149. Menendez, M., et al., *Control of the structural stability of the tubulin dimer by one high affinity bound magnesium ion at nucleotide N-site*. *J Biol Chem*, 1998. **273**(1): p. 167-76.
150. Nogales, E., et al., *High-resolution model of the microtubule*. *Cell*, 1999. **96**(1): p. 79-88.
151. Unger, E., K.J. Bohm, and W. Vater, *Structural diversity and dynamics of microtubules and polymorphic tubulin assemblies*. *Electron Microsc Rev*, 1990. **3**(2): p. 355-95.
152. Tilney, L.G., et al., *Microtubules: evidence for 13 protofilaments*. *J Cell Biol*, 1973. **59**(2 Pt 1): p. 267-75.
153. Pierson, G.B., P.R. Burton, and R.H. Himes, *Alterations in number of protofilaments in microtubules assembled in vitro*. *J Cell Biol*, 1978. **76**(1): p. 223-8.
154. Marx, A., et al., *Interaction of kinesin motors, microtubules, and MAPs*. *J Muscle Res Cell Motil*, 2006. **27**(2): p. 125-37.
155. Amos, L.A. and D. Schlieper, *Microtubules and maps*. *Adv Protein Chem*, 2005. **71**: p. 257-98.
156. Desai, A. and T.J. Mitchison, *Microtubule polymerization dynamics*. *Annu Rev Cell Dev Biol*, 1997. **13**: p. 83-117.
157. Kollman, J.M., et al., *Microtubule nucleation by gamma-tubulin complexes*. *Nat Rev Mol Cell Biol*, 2011. **12**(11): p. 709-21.
158. Wiese, C. and Y. Zheng, *A new function for the gamma-tubulin ring complex as a microtubule minus-end cap*. *Nat Cell Biol*, 2000. **2**(6): p. 358-64.
159. Jaspersen, S.L. and M. Winey, *The budding yeast spindle pole body: structure, duplication, and function*. *Annu Rev Cell Dev Biol*, 2004. **20**: p. 1-28.
160. Mitchison, T. and M. Kirschner, *Dynamic instability of microtubule growth*. *Nature*, 1984. **312**(5991): p. 237-42.
161. Howard, J. and A.A. Hyman, *Dynamics and mechanics of the microtubule plus end*. *Nature*, 2003. **422**(6933): p. 753-8.
162. Walker, R.A., et al., *Dynamic instability of individual microtubules analyzed by video light microscopy: rate constants and transition frequencies*. *J Cell Biol*, 1988. **107**(4): p. 1437-48.
163. Figure 16-6, *Molecular biology of the cell*, 4th edition
164. Bowne-Anderson, H., et al., *Microtubule dynamic instability: a new model with coupled GTP hydrolysis and multistep catastrophe*. *Bioessays*, 2013. **35**(5): p. 452-61.
165. Howard, J. and A.A. Hyman, *Microtubule polymerases and depolymerases*. *Curr Opin Cell Biol*, 2007. **19**(1): p. 31-5.
166. van der Vaart, B., A. Akhmanova, and A. Straube, *Regulation of microtubule dynamic instability*. *Biochem Soc Trans*, 2009. **37**(Pt 5): p. 1007-13.
167. Goodson, H.V. and E.M. Jonasson, *Microtubules and Microtubule-Associated Proteins*. *Cold Spring Harb Perspect Biol*, 2018. **10**(6).
168. Ramkumar, A., B.Y. Jong, and K.M. Ori-McKenney, *ReMAPping the microtubule landscape: How phosphorylation dictates the activities of microtubule-associated proteins*. *Dev Dyn*, 2018. **247**(1): p. 138-155.
169. Akhmanova, A. and M.O. Steinmetz, *Microtubule +TIPs at a glance*. *J Cell Sci*, 2010. **123**(Pt 20): p. 3415-9.
170. Gard, D.L. and M.W. Kirschner, *A microtubule-associated protein from Xenopus eggs that specifically promotes assembly at the plus-end*. *J Cell Biol*, 1987. **105**(5): p. 2203-15.
171. Gard, D.L. and M.W. Kirschner, *Microtubule assembly in cytoplasmic extracts of Xenopus oocytes and eggs*. *J Cell Biol*, 1987. **105**(5): p. 2191-201.
172. Al-Bassam, J. and F. Chang, *Regulation of microtubule dynamics by TOG-domain proteins XMAP215/Dis1 and CLASP*. *Trends Cell Biol*, 2011. **21**(10): p. 604-14.

173. Brouhard, G.J., et al., *XMAP215 is a processive microtubule polymerase*. Cell, 2008. **132**(1): p. 79-88.
174. Dehmelt, L. and S. Halpain, *The MAP2/Tau family of microtubule-associated proteins*. Genome Biol, 2005. **6**(1): p. 204.
175. Vallee, R.B. and G.G. Borisy, *The non-tubulin component of microtubule protein oligomers. Effect on self-association and hydrodynamic properties*. J Biol Chem, 1978. **253**(8): p. 2834-45.
176. Bosc, C., A. Andrieux, and D. Job, *STOP proteins*. Biochemistry, 2003. **42**(42): p. 12125-32.
177. Fourniol, F., et al., *Structural studies of the doublecortin family of MAPs*. Methods Cell Biol, 2013. **115**: p. 27-48.
178. Bayliss, R., et al., *Molecular mechanisms that underpin EML4-ALK driven cancers and their response to targeted drugs*. Cell Mol Life Sci, 2016. **73**(6): p. 1209-24.
179. Goodwin, S.S. and R.D. Vale, *Patronin regulates the microtubule network by protecting microtubule minus ends*. Cell, 2010. **143**(2): p. 263-74.
180. Jiang, K., et al., *Microtubule minus-end stabilization by polymerization-driven CAMSAP deposition*. Dev Cell, 2014. **28**(3): p. 295-309.
181. Kinoshita, K., et al., *Global and local control of microtubule destabilization promoted by a catastrophe kinesin MCAK/XKCM1*. J Muscle Res Cell Motil, 2006. **27**(2): p. 107-14.
182. Kuo, Y.W., et al., *Spastin is a dual-function enzyme that severs microtubules and promotes their regrowth to increase the number and mass of microtubules*. Proc Natl Acad Sci U S A, 2019. **116**(12): p. 5533-5541.
183. McNally, F.J. and R.D. Vale, *Identification of katanin, an ATPase that severs and disassembles stable microtubules*. Cell, 1993. **75**(3): p. 419-29.
184. Trotta, N., et al., *The hereditary spastic paraplegia gene, spastin, regulates microtubule stability to modulate synaptic structure and function*. Curr Biol, 2004. **14**(13): p. 1135-47.
185. Perez, F., et al., *CLIP-170 highlights growing microtubule ends in vivo*. Cell, 1999. **96**(4): p. 517-27.
186. Diamantopoulos, G.S., et al., *Dynamic localization of CLIP-170 to microtubule plus ends is coupled to microtubule assembly*. J Cell Biol, 1999. **144**(1): p. 99-112.
187. Brunner, D. and P. Nurse, *CLIP170-like tip1p spatially organizes microtubular dynamics in fission yeast*. Cell, 2000. **102**(5): p. 695-704.
188. Arnal, I., et al., *CLIP-170/tubulin-curved oligomers coassemble at microtubule ends and promote rescues*. Curr Biol, 2004. **14**(23): p. 2086-95.
189. Dixit, R., et al., *Microtubule plus-end tracking by CLIP-170 requires EB1*. Proc Natl Acad Sci U S A, 2009. **106**(2): p. 492-7.
190. Lansbergen, G. and A. Akhmanova, *Microtubule plus end: a hub of cellular activities*. Traffic, 2006. **7**(5): p. 499-507.
191. Morrison, E.E., et al., *EB1, a protein which interacts with the APC tumour suppressor, is associated with the microtubule cytoskeleton throughout the cell cycle*. Oncogene, 1998. **17**(26): p. 3471-7.
192. Rogers, S.L., et al., *Drosophila EB1 is important for proper assembly, dynamics, and positioning of the mitotic spindle*. J Cell Biol, 2002. **158**(5): p. 873-84.
193. Berrueta, L., et al., *The APC-associated protein EB1 associates with components of the dynactin complex and cytoplasmic dynein intermediate chain*. Curr Biol, 1999. **9**(8): p. 425-8.
194. Varma, D. and E.D. Salmon, *The KMN protein network--chief conductors of the kinetochore orchestra*. J Cell Sci, 2012. **125**(Pt 24): p. 5927-36.
195. Pollard, T.D. and E.D. Korn, *Electron microscopic identification of actin associated with isolated amoeba plasma membranes*. J Biol Chem, 1973. **248**(2): p. 448-50.
196. Gibbons, I.R. and A.J. Rowe, *Dynein: A Protein with Adenosine Triphosphatase Activity from Cilia*. Science, 1965. **149**(3682): p. 424-6.
197. Vale, R.D., T.S. Reese, and M.P. Sheetz, *Identification of a novel force-generating protein, kinesin, involved in microtubule-based motility*. Cell, 1985. **42**(1): p. 39-50.
198. Hirokawa, N., Y. Noda, and Y. Okada, *Kinesin and dynein superfamily proteins in organelle transport and cell division*. Curr Opin Cell Biol, 1998. **10**(1): p. 60-73.

199. Hirokawa, N., *Kinesin and dynein superfamily proteins and the mechanism of organelle transport*. Science, 1998. **279**(5350): p. 519-26.
200. Hirokawa, N., et al., *Kinesin superfamily motor proteins and intracellular transport*. Nat Rev Mol Cell Biol, 2009. **10**(10): p. 682-96.
201. Brady, S.T., *A novel brain ATPase with properties expected for the fast axonal transport motor*. Nature, 1985. **317**(6032): p. 73-5.
202. Marx, A., J. Muller, and E. Mandelkow, *The structure of microtubule motor proteins*. Adv Protein Chem, 2005. **71**: p. 299-344.
203. Vicente, J.J. and L. Wordeman, *Mitosis, microtubule dynamics and the evolution of kinesins*. Exp Cell Res, 2015. **334**(1): p. 61-9.
204. Lawrence, C.J., et al., *A standardized kinesin nomenclature*. J Cell Biol, 2004. **167**(1): p. 19-22.
205. Kim, A.J. and S.A. Endow, *A kinesin family tree*. J Cell Sci, 2000. **113 Pt 21**: p. 3681-2.
206. Dagenbach, E.M. and S.A. Endow, *A new kinesin tree*. J Cell Sci, 2004. **117**(Pt 1): p. 3-7.
207. Yang, J.T., R.A. Laymon, and L.S. Goldstein, *A three-domain structure of kinesin heavy chain revealed by DNA sequence and microtubule binding analyses*. Cell, 1989. **56**(5): p. 879-89.
208. Walker, J.E., et al., *Distantly related sequences in the alpha- and beta-subunits of ATP synthase, myosin, kinases and other ATP-requiring enzymes and a common nucleotide binding fold*. EMBO J, 1982. **1**(8): p. 945-51.
209. Kozielski, F., et al., *The crystal structure of dimeric kinesin and implications for microtubule-dependent motility*. Cell, 1997. **91**(7): p. 985-94.
210. Kozielski, F., et al., *Crystallization and preliminary X-ray analysis of the single-headed and double-headed motor protein kinesin*. J Struct Biol, 1997. **119**(1): p. 28-34.
211. Vale, R.D. and R.J. Fletterick, *The design plan of kinesin motors*. Annu Rev Cell Dev Biol, 1997. **13**: p. 745-77.
212. Ogawa, T., et al., *A common mechanism for microtubule destabilizers-M type kinesins stabilize curling of the protofilament using the class-specific neck and loops*. Cell, 2004. **116**(4): p. 591-602.
213. Wickstead, B., K. Gull, and T.A. Richards, *Patterns of kinesin evolution reveal a complex ancestral eukaryote with a multifunctional cytoskeleton*. BMC Evol Biol, 2010. **10**: p. 110.
214. Schief, W.R. and J. Howard, *Conformational changes during kinesin motility*. Curr Opin Cell Biol, 2001. **13**(1): p. 19-28.
215. Svoboda, K. and S.M. Block, *Force and velocity measured for single kinesin molecules*. Cell, 1994. **77**(5): p. 773-84.
216. Vale, R.D. and R.A. Milligan, *The way things move: looking under the hood of molecular motor proteins*. Science, 2000. **288**(5463): p. 88-95.
217. Yildiz, A., et al., *Kinesin walks hand-over-hand*. Science, 2004. **303**(5658): p. 676-8.
218. Howard, J., A.J. Hudspeth, and R.D. Vale, *Movement of microtubules by single kinesin molecules*. Nature, 1989. **342**(6246): p. 154-8.
219. Block, S.M., L.S. Goldstein, and B.J. Schnapp, *Bead movement by single kinesin molecules studied with optical tweezers*. Nature, 1990. **348**(6299): p. 348-52.
220. Hackney, D.D., *Highly processive microtubule-stimulated ATP hydrolysis by dimeric kinesin head domains*. Nature, 1995. **377**(6548): p. 448-50.
221. Svoboda, K., et al., *Direct observation of kinesin stepping by optical trapping interferometry*. Nature, 1993. **365**(6448): p. 721-7.
222. Coy, D.L., M. Wagenbach, and J. Howard, *Kinesin takes one 8-nm step for each ATP that it hydrolyzes*. J Biol Chem, 1999. **274**(6): p. 3667-71.
223. Schnitzer, M.J. and S.M. Block, *Kinesin hydrolyses one ATP per 8-nm step*. Nature, 1997. **388**(6640): p. 386-90.
224. Cui, W., et al., *Drosophila Nod protein binds preferentially to the plus ends of microtubules and promotes microtubule polymerization in vitro*. Mol Biol Cell, 2005. **16**(11): p. 5400-9.
225. Friel, C.T. and J. Howard, *The kinesin-13 MCAK has an unconventional ATPase cycle adapted for microtubule depolymerization*. EMBO J, 2011. **30**(19): p. 3928-39.

226. Hunter, A.W., et al., *The kinesin-related protein MCAK is a microtubule depolymerase that forms an ATP-hydrolyzing complex at microtubule ends*. Mol Cell, 2003. **11**(2): p. 445-57.
227. Hildebrandt, E.R. and M.A. Hoyt, *Mitotic motors in Saccharomyces cerevisiae*. Biochim Biophys Acta, 2000. **1496**(1): p. 99-116.
228. Lillie, S.H. and S.S. Brown, *Immunofluorescence localization of the unconventional myosin, Myo2p, and the putative kinesin-related protein, Smy1p, to the same regions of polarized growth in Saccharomyces cerevisiae*. J Cell Biol, 1994. **125**(4): p. 825-42.
229. Roof, D.M., P.B. Meluh, and M.D. Rose, *Kinesin-related proteins required for assembly of the mitotic spindle*. J Cell Biol, 1992. **118**(1): p. 95-108.
230. Lyle, K., P. Kumar, and T. Wittmann, *SnapShot: Microtubule regulators II*. Cell, 2009. **136**(3): p. 566, 566 e1.
231. Miki, H. and N. Hirokawa, *Kinesin Superfamily Classification*, in *Encyclopedia of Biophysics*, G.C.K. Roberts, Editor. 2013, Springer Berlin Heidelberg: Berlin, Heidelberg. p. 1191-1200.
232. Nakagawa, T., et al., *Identification and classification of 16 new kinesin superfamily (KIF) proteins in mouse genome*. Proc Natl Acad Sci U S A, 1997. **94**(18): p. 9654-9.
233. <https://www.uniprot.org/uniprot/P28743>
234. <https://www.yeastgenome.org/locus/S000006076>
235. <https://www.uniprot.org/uniprot/C7GJA7>
236. Ubersax, J.A., et al., *Targets of the cyclin-dependent kinase Cdk1*. Nature, 2003. **425**(6960): p. 859-64.
237. Drechsler, H., A.N. Tan, and D. Liakopoulos, *Yeast GSK-3 kinase regulates astral microtubule function through phosphorylation of the microtubule-stabilizing kinesin Kip2*. J Cell Sci, 2015. **128**(21): p. 3910-21.
238. Cottingham, F.R. and M.A. Hoyt, *Mitotic spindle positioning in Saccharomyces cerevisiae is accomplished by antagonistically acting microtubule motor proteins*. J Cell Biol, 1997. **138**(5): p. 1041-53.
239. Saunders, W., V. Lengyel, and M.A. Hoyt, *Mitotic spindle function in Saccharomyces cerevisiae requires a balance between different types of kinesin-related motors*. Mol Biol Cell, 1997. **8**(6): p. 1025-33.
240. Miller, R.K., et al., *The kinesin-related proteins, Kip2p and Kip3p, function differently in nuclear migration in yeast*. Mol Biol Cell, 1998. **9**(8): p. 2051-68.
241. Carvalho, P., et al., *Cell cycle control of kinesin-mediated transport of Bik1 (CLIP-170) regulates microtubule stability and dynein activation*. Dev Cell, 2004. **6**(6): p. 815-29.
242. Huyett, A., et al., *The Kar3p and Kip2p motors function antagonistically at the spindle poles to influence cytoplasmic microtubule numbers*. J Cell Sci, 1998. **111 (Pt 3)**: p. 295-301.
243. Maekawa, H., et al., *Yeast Cdk1 translocates to the plus end of cytoplasmic microtubules to regulate bud cortex interactions*. EMBO J, 2003. **22**(3): p. 438-49.
244. Bienz, M., *Spindles cotton on to junctions, APC and EB1*. Nat Cell Biol, 2001. **3**(3): p. E67-8.
245. Miller, R.K. and M.D. Rose, *Kar9p is a novel cortical protein required for cytoplasmic microtubule orientation in yeast*. J Cell Biol, 1998. **140**(2): p. 377-90.
246. Miller, R.K., S.C. Cheng, and M.D. Rose, *Bim1p/Yeb1p mediates the Kar9p-dependent cortical attachment of cytoplasmic microtubules*. Mol Biol Cell, 2000. **11**(9): p. 2949-59.
247. Roberts, A.J., B.S. Goodman, and S.L. Reck-Peterson, *Reconstitution of dynein transport to the microtubule plus end by kinesin*. Elife, 2014. **3**: p. e02641.
248. Caudron, F., et al., *A new role for kinesin-directed transport of Bik1p (CLIP-170) in Saccharomyces cerevisiae*. J Cell Sci, 2008. **121**(Pt 9): p. 1506-13.
249. Sheeman, B., et al., *Determinants of S. cerevisiae dynein localization and activation: implications for the mechanism of spindle positioning*. Curr Biol, 2003. **13**(5): p. 364-72.
250. Moore, J.K., M.D. Stuchell-Breteron, and J.A. Cooper, *Function of dynein in budding yeast: mitotic spindle positioning in a polarized cell*. Cell Motil Cytoskeleton, 2009. **66**(8): p. 546-55.
251. Hibbel, A., et al., *Kinesin Kip2 enhances microtubule growth in vitro through length-dependent feedback on polymerization and catastrophe*. Elife, 2015. **4**.

252. Liu, A.P. and D.A. Fletcher, *Biology under construction: in vitro reconstitution of cellular function*. Nat Rev Mol Cell Biol, 2009. **10**(9): p. 644-50.
253. Gell, C., et al., *Microtubule dynamics reconstituted in vitro and imaged by single-molecule fluorescence microscopy*. Methods Cell Biol, 2010. **95**: p. 221-45.
254. Zanic, M., et al., *Synergy between XMAP215 and EB1 increases microtubule growth rates to physiological levels*. Nat Cell Biol, 2013. **15**(6): p. 688-93.
255. Gardner, M.K., et al., *Rapid microtubule self-assembly kinetics*. Cell, 2011. **146**(4): p. 582-92.
256. Bieling, P., et al., *Reconstitution of a microtubule plus-end tracking system in vitro*. Nature, 2007. **450**(7172): p. 1100-5.
257. Podolski, M., M. Mahamdeh, and J. Howard, *Stu2, the budding yeast XMAP215/Dis1 homolog, promotes assembly of yeast microtubules by increasing growth rate and decreasing catastrophe frequency*. J Biol Chem, 2014. **289**(41): p. 28087-93.
258. Varga, V., et al., *Yeast kinesin-8 depolymerizes microtubules in a length-dependent manner*. Nat Cell Biol, 2006. **8**(9): p. 957-62.
259. Gell, C., et al., *Purification of tubulin from porcine brain*. Methods Mol Biol, 2011. **777**: p. 15-28.
260. Schnitzer, M.J., K. Visscher, and S.M. Block, *Force production by single kinesin motors*. Nat Cell Biol, 2000. **2**(10): p. 718-23.
261. Svoboda, K. and S.M. Block, *Biological applications of optical forces*. Annu Rev Biophys Biomol Struct, 1994. **23**: p. 247-85.
262. Shang, Z., et al., *High-resolution structures of kinesin on microtubules provide a basis for nucleotide-gated force-generation*. Elife, 2014. **3**: p. e04686.
263. Gigant, B., et al., *Structure of a kinesin-tubulin complex and implications for kinesin motility*. Nat Struct Mol Biol, 2013. **20**(8): p. 1001-7.
264. Ghaemmaghami, S., et al., *Global analysis of protein expression in yeast*. Nature, 2003. **425**(6959): p. 737-41.
265. Ayaz, P., et al., *A TOG:alphabeta-tubulin complex structure reveals conformation-based mechanisms for a microtubule polymerase*. Science, 2012. **337**(6096): p. 857-60.
266. Kural, C., et al., *Kinesin and dynein move a peroxisome in vivo: a tug-of-war or coordinated movement?* Science, 2005. **308**(5727): p. 1469-72.
267. Hyman, A., et al., *Preparation of modified tubulins*. Methods Enzymol, 1991. **196**: p. 478-85.
268. Bormuth, V., J. Howard, and E. Schaffer, *LED illumination for video-enhanced DIC imaging of single microtubules*. J Microsc, 2007. **226**(Pt 1): p. 1-5.
269. Kirschner, M.W., et al., *Microtubules from mammalian brain: some properties of their depolymerization products and a proposed mechanism of assembly and disassembly*. Proc Natl Acad Sci U S A, 1974. **71**(4): p. 1159-63.
270. Mandelkow, E.M., E. Mandelkow, and R.A. Milligan, *Microtubule dynamics and microtubule caps: a time-resolved cryo-electron microscopy study*. J Cell Biol, 1991. **114**(5): p. 977-91.
271. Chretien, D., S.D. Fuller, and E. Karsenti, *Structure of growing microtubule ends: two-dimensional sheets close into tubes at variable rates*. J Cell Biol, 1995. **129**(5): p. 1311-28.
272. Downing, K.H. and E. Nogales, *Tubulin structure: insights into microtubule properties and functions*. Curr Opin Struct Biol, 1998. **8**(6): p. 785-91.
273. Downing, K.H. and E. Nogales, *New insights into microtubule structure and function from the atomic model of tubulin*. Eur Biophys J, 1998. **27**(5): p. 431-6.
274. Downing, K.H. and E. Nogales, *Tubulin and microtubule structure*. Curr Opin Cell Biol, 1998. **10**(1): p. 16-22.
275. Gigant, B., et al., *The 4 A X-ray structure of a tubulin:stathmin-like domain complex*. Cell, 2000. **102**(6): p. 809-16.
276. Ravelli, R.B., et al., *Insight into tubulin regulation from a complex with colchicine and a stathmin-like domain*. Nature, 2004. **428**(6979): p. 198-202.
277. Wang, H.W. and E. Nogales, *Nucleotide-dependent bending flexibility of tubulin regulates microtubule assembly*. Nature, 2005. **435**(7044): p. 911-5.
278. Nawrotek, A., M. Knossow, and B. Gigant, *The determinants that govern microtubule assembly from the atomic structure of GTP-tubulin*. J Mol Biol, 2011. **412**(1): p. 35-42.

279. Pecqueur, L., et al., *A designed ankyrin repeat protein selected to bind to tubulin caps the microtubule plus end*. Proc Natl Acad Sci U S A, 2012. **109**(30): p. 12011-6.
280. Ozon, S., A. Maucuer, and A. Sobel, *The stathmin family -- molecular and biological characterization of novel mammalian proteins expressed in the nervous system*. Eur J Biochem, 1997. **248**(3): p. 794-806.
281. Wang, P.J. and T.C. Huffaker, *Stu2p: A microtubule-binding protein that is an essential component of the yeast spindle pole body*. J Cell Biol, 1997. **139**(5): p. 1271-80.
282. Campanacci, V., et al., *Selection and Characterization of Artificial Proteins Targeting the Tubulin alpha Subunit*. Structure, 2019. **27**(3): p. 497-506 e4.
283. Dubochet, J., et al., *Cryo-electron microscopy of vitrified specimens*. Q Rev Biophys, 1988. **21**(2): p. 129-228.
284. Wade, R.H. and D. Chretien, *Cryoelectron microscopy of microtubules*. J Struct Biol, 1993. **110**(1): p. 1-27.
285. Nogales, E., *Structural insights into microtubule function*. Annu Rev Biochem, 2000. **69**: p. 277-302.
286. Kuhlbrandt, W., *Biochemistry. The resolution revolution*. Science, 2014. **343**(6178): p. 1443-4.
287. Zhang, R. and E. Nogales, *A new protocol to accurately determine microtubule lattice seam location*. J Struct Biol, 2015. **192**(2): p. 245-54.
288. Manka, S.W. and C.A. Moores, *Microtubule structure by cryo-EM: snapshots of dynamic instability*. Essays Biochem, 2018. **62**(6): p. 737-751.
289. Mignot, I., et al., *Design and characterization of modular scaffolds for tubulin assembly*. J Biol Chem, 2012. **287**(37): p. 31085-94.
290. Gigant, B., et al., *Mechanism of Tau-promoted microtubule assembly as probed by NMR spectroscopy*. J Am Chem Soc, 2014. **136**(36): p. 12615-23.
291. Fauquant, C., et al., *Systematic identification of tubulin-interacting fragments of the microtubule-associated protein Tau leads to a highly efficient promoter of microtubule assembly*. J Biol Chem, 2011. **286**(38): p. 33358-68.
292. Hailat, N., et al., *N-myc gene amplification in neuroblastoma is associated with altered phosphorylation of a proliferation related polypeptide (Op18)*. Oncogene, 1990. **5**(11): p. 1615-8.
293. Pasmantier, R., et al., *P19, a hormonally regulated phosphoprotein of peptide hormone-producing cells: secretagogue-induced phosphorylation in AtT-20 mouse pituitary tumor cells and in rat and hamster insulinoma cells*. Endocrinology, 1986. **119**(3): p. 1229-38.
294. Steinmetz, M.O., *Structure and thermodynamics of the tubulin-stathmin interaction*. J Struct Biol, 2007. **158**(2): p. 137-47.
295. Gavet, O., et al., *The stathmin phosphoprotein family: intracellular localization and effects on the microtubule network*. J Cell Sci, 1998. **111 (Pt 22)**: p. 3333-46.
296. Gradin, H.M., et al., *Regulation of microtubule dynamics by extracellular signals: cAMP-dependent protein kinase switches off the activity of oncoprotein 18 in intact cells*. J Cell Biol, 1998. **140**(1): p. 131-41.
297. Barbier, P., et al., *Stathmin and interfacial microtubule inhibitors recognize a naturally curved conformation of tubulin dimers*. J Biol Chem, 2010. **285**(41): p. 31672-81.
298. Binz, H.K., et al., *Designing repeat proteins: well-expressed, soluble and stable proteins from combinatorial libraries of consensus ankyrin repeat proteins*. J Mol Biol, 2003. **332**(2): p. 489-503.
299. Sedgwick, S.G. and S.J. Smerdon, *The ankyrin repeat: a diversity of interactions on a common structural framework*. Trends Biochem Sci, 1999. **24**(8): p. 311-6.
300. Tamaskovic, R., et al., *Designed ankyrin repeat proteins (DARPs) from research to therapy*. Methods Enzymol, 2012. **503**: p. 101-34.
301. Binz, H.K., et al., *High-affinity binders selected from designed ankyrin repeat protein libraries*. Nat Biotechnol, 2004. **22**(5): p. 575-82.
302. Dreier, B. and A. Pluckthun, *Rapid selection of high-affinity binders using ribosome display*. Methods Mol Biol, 2012. **805**: p. 261-86.
303. Hanes, J. and A. Pluckthun, *In vitro selection and evolution of functional proteins by using ribosome display*. Proc Natl Acad Sci U S A, 1997. **94**(10): p. 4937-42.

304. Cao, L., et al., *The structure of apo-kinesin bound to tubulin links the nucleotide cycle to movement*. Nat Commun, 2014. **5**: p. 5364.
305. Hayashi, I. and M. Ikura, *Crystal structure of the amino-terminal microtubule-binding domain of end-binding protein 1 (EB1)*. J Biol Chem, 2003. **278**(38): p. 36430-4.
306. Slep, K.C. and R.D. Vale, *Structural basis of microtubule plus end tracking by XMAP215, CLIP-170, and EB1*. Mol Cell, 2007. **27**(6): p. 976-91.
307. Honnappa, S., et al., *An EB1-binding motif acts as a microtubule tip localization signal*. Cell, 2009. **138**(2): p. 366-76.
308. Su, L.K., et al., *APC binds to the novel protein EB1*. Cancer Res, 1995. **55**(14): p. 2972-7.
309. Schwartz, K., K. Richards, and D. Botstein, *BIM1 encodes a microtubule-binding protein in yeast*. Mol Biol Cell, 1997. **8**(12): p. 2677-91.
310. Beinhauer, J.D., et al., *Mal3, the fission yeast homologue of the human APC-interacting protein EB-1 is required for microtubule integrity and the maintenance of cell form*. J Cell Biol, 1997. **139**(3): p. 717-28.
311. Maurer, S.P., et al., *EB1 accelerates two conformational transitions important for microtubule maturation and dynamics*. Curr Biol, 2014. **24**(4): p. 372-84.
312. Akhmanova, A., et al., *The microtubule plus-end-tracking protein CLIP-170 associates with the spermatid manchette and is essential for spermatogenesis*. Genes Dev, 2005. **19**(20): p. 2501-15.
313. Akhmanova, A. and M.O. Steinmetz, *Tracking the ends: a dynamic protein network controls the fate of microtubule tips*. Nat Rev Mol Cell Biol, 2008. **9**(4): p. 309-22.
314. Maurer, S.P., et al., *EBs recognize a nucleotide-dependent structural cap at growing microtubule ends*. Cell, 2012. **149**(2): p. 371-82.
315. Zhang, R., et al., *Mechanistic Origin of Microtubule Dynamic Instability and Its Modulation by EB Proteins*. Cell, 2015. **162**(4): p. 849-59.
316. Zanic, M., et al., *EB1 recognizes the nucleotide state of tubulin in the microtubule lattice*. PLoS One, 2009. **4**(10): p. e7585.
317. Maurer, S.P., et al., *GTPgammaS microtubules mimic the growing microtubule end structure recognized by end-binding proteins (EBs)*. Proc Natl Acad Sci U S A, 2011. **108**(10): p. 3988-93.
318. Reid, T.A., et al., *Structural state recognition facilitates tip tracking of EB1 at growing microtubule ends*. Elife, 2019. **8**.
319. Zhang, R., B. LaFrance, and E. Nogales, *Separating the effects of nucleotide and EB binding on microtubule structure*. Proc Natl Acad Sci U S A, 2018. **115**(27): p. E6191-E6200.
320. Cleveland, D.W., S.Y. Hwo, and M.W. Kirschner, *Physical and chemical properties of purified tau factor and the role of tau in microtubule assembly*. J Mol Biol, 1977. **116**(2): p. 227-47.
321. Drubin, D.G. and M.W. Kirschner, *Tau protein function in living cells*. J Cell Biol, 1986. **103**(6 Pt 2): p. 2739-46.
322. Preuss, U., et al., *The 'jaws' model of tau-microtubule interaction examined in CHO cells*. J Cell Sci, 1997. **110 (Pt 6)**: p. 789-800.
323. Garcia, M.L. and D.W. Cleveland, *Going new places using an old MAP: tau, microtubules and human neurodegenerative disease*. Curr Opin Cell Biol, 2001. **13**(1): p. 41-8.
324. Al-Bassam, J., et al., *MAP2 and tau bind longitudinally along the outer ridges of microtubule protofilaments*. J Cell Biol, 2002. **157**(7): p. 1187-96.
325. Kellogg, E.H., et al., *Near-atomic model of microtubule-tau interactions*. Science, 2018. **360**(6394): p. 1242-1246.
326. World Alzheimer Repot 2016 & 2015, Alzheimer's Disease International
327. Kadavath, H., et al., *Folding of the Tau Protein on Microtubules*. Angew Chem Int Ed Engl, 2015. **54**(35): p. 10347-51.
328. Kosik, K.S., et al., *Developmentally regulated expression of specific tau sequences*. Neuron, 1989. **2**(4): p. 1389-97.
329. Grundke-Iqbal, I., et al., *Abnormal phosphorylation of the microtubule-associated protein tau (tau) in Alzheimer cytoskeletal pathology*. Proc Natl Acad Sci U S A, 1986. **83**(13): p. 4913-7.

330. Min, S.W., et al., *Acetylation of tau inhibits its degradation and contributes to tauopathy*. Neuron, 2010. **67**(6): p. 953-66.
331. Cohen, T.J., et al., *The acetylation of tau inhibits its function and promotes pathological tau aggregation*. Nat Commun, 2011. **2**: p. 252.
332. Nakamura, K., et al., *Proline isomer-specific antibodies reveal the early pathogenic tau conformation in Alzheimer's disease*. Cell, 2012. **149**(1): p. 232-44.
333. Mukrasch, M.D., et al., *Structural polymorphism of 441-residue tau at single residue resolution*. PLoS Biol, 2009. **7**(2): p. e34.
334. Santarella, R.A., et al., *Surface-decoration of microtubules by human tau*. J Mol Biol, 2004. **339**(3): p. 539-53.
335. Bibow, S., et al., *The dynamic structure of filamentous tau*. Angew Chem Int Ed Engl, 2011. **50**(48): p. 11520-4.
336. Honnappa, S., et al., *Thermodynamics of the Op18/stathmin-tubulin interaction*. J Biol Chem, 2003. **278**(40): p. 38926-34.
337. Rice, L.M., E.A. Montabana, and D.A. Agard, *The lattice as allosteric effector: structural studies of alphabeta- and gamma-tubulin clarify the role of GTP in microtubule assembly*. Proc Natl Acad Sci U S A, 2008. **105**(14): p. 5378-83.
338. Buey, R.M., J.F. Diaz, and J.M. Andreu, *The nucleotide switch of tubulin and microtubule assembly: a polymerization-driven structural change*. Biochemistry, 2006. **45**(19): p. 5933-8.
339. Melki, R., et al., *Cold depolymerization of microtubules to double rings: geometric stabilization of assemblies*. Biochemistry, 1989. **28**(23): p. 9143-52.
340. Campanacci, V., et al., *Insight into microtubule nucleation from tubulin-capping proteins*. Proc Natl Acad Sci U S A, 2019. **116**(20): p. 9859-9864.
341. Schweers, O., et al., *Structural studies of tau protein and Alzheimer paired helical filaments show no evidence for beta-structure*. J Biol Chem, 1994. **269**(39): p. 24290-7.
342. Li, X.H., J.A. Culver, and E. Rhoades, *Tau Binds to Multiple Tubulin Dimers with Helical Structure*. J Am Chem Soc, 2015. **137**(29): p. 9218-21.
343. Chayen N. E., S.S.P.D., Maeder D. L., Blow D. M., *An automated system for micro-batch protein crystallization and screening*. Journal of Applied Crystallography, 1990. **23**(4): p. 297-302.
344. Gaskin, F. and Y. Kress, *Zinc ion-induced assembly of tubulin*. J Biol Chem, 1977. **252**(19): p. 6918-24.